Astronomy Reports, Vol. 45, No. 6, 2001, pp. 415–416. Translated from Astronomicheskiĭ Zhurnal, Vol. 78, No. 6, 2001, pp. 483–484.

The 70th Birthday of Aleksandr Alekseevich Boyarchuk

Academician Aleksandr Alekseevich Boyarchuk—the Academic Secretary of the Division of General Physics and Astrophysics of the Russian Academy of Sciences, Directory of the Institute of Astronomy of the Russian Academy of Sciences, and main editor of *Astronomicheskiĭ Zhurnal*—will celebrate his 70th birthday on June 21, 2001.

A. A. Boyarchuk is an eminent astrophysicist specializing in the fields of stellar spectroscopy, the physics of stellar atmospheres, stellar envelopes and circumstellar material, space-based optical astronomy, and the construction of astronomical instruments and telescopes.

The beginning of his scientific activity and an appreciable fraction of his life were connected to the Crimean Astrophysical Observatory of the Academy of Sciences of the USSR. After graduating from the mathematical mechanics department of Leningrad State University with a specialty in astronomy in 1953, Boyarchuk became a graduate student at the Crimean Astrophysical Observatory and, after successfully defending his dissertation, began to work as a junior, then senior scientist at the Observatory. In 1969, he was appointed Assistant Director, retaining this position until 1987. In 1976, Boyarchuk was elected a corresponding member of the Academy of Sciences of the USSR. In 1987, he became director of the Astronomy Council of the Academy of Sciences (renamed the Institute of Astronomy three years later) and moved to Moscow. In this same year, Boyarchuk was elected as a full member of the Russian Academy of Sciences and became a member of the Presidium of the Russian Academy of Sciences two years later. In 1996, he became head of the Division of General Physics and Astronomy of the Russian Academy of Sciences—the largest division in the Academy system—while also continuing as head of the Institute of Astronomy.

The earliest of Boyarchuk's important scientific results were obtained during studies of Be stars. He determined the physical parameters in the envelopes of these stars and created a model for the Be-star phenomenon. Further, using a broad base of observational material on symbiotic stars, Boyarchuk carried out detailed investigations of these objects, which were quite mysterious at that time, and constructed a multi-component model that made it possible to understand their observed spectral and photometric properties. Based on these stars, and subsequently also various other types of non-steady-state stars, he proposed now widely accepted concepts concerning the observational manifestations of various effects in the evolution of stars in close binary systems.

Over the last several years, Boyarchuk and his coauthors have carried out extremely interesting detailed hydrodynamical computations of matter exchange in close binary systems; these have shown that widely used, simplified models with a "hot spot" on an accretion disk do not correspond to the real, complex, physical patterns of the flow of matter from one stellar component to another. The construction of two-dimensional and three-dimensional models based on these computations and analyses of the gas-dynamical flows in such systems have revealed a number of fundamentally new effects in the physics of mass transfer in cataclysmic binaries, symbiotic stars, and low-mass and massive x-ray binary systems.

The work of Boyarchuk on the chemical compositions of various types of stars—red giants, supergiants, new stars, Be stars, symbiotic stars and other close binaries, metallic stars, and also the unique object FG Sgr—is of fundamental importance. The discovery by Boyarchuk and his colleagues back in the 1970s of sodium overabundances in the atmospheres of super-

1063-7729/01/4506-0415$21.00 © 2001 MAIK "Nauka/Interperiodica"

giants first demonstrated that not only elements synthesized in the CNO cycle are carried to the surfaces of evolved stars. These and further detailed observational studies revealed interesting dependences of the sodium overabundances in the atmospheres of supergiants and giants on their luminosities. Analyses of recent observations of the atmospheres of a number of giants have demonstrated analogous anomalies in the abundances of aluminum and silicon.

At the end of the 1950s and beginning of the 1960s, Boyarchuk carried out a series of pioneering studies of phenomena associated with stellar rotation. He was the first to compile a catalog of stellar rotation rates, containing 2362 objects. Statistical analyses of the data in this catalog have enabled the identification of peculiarities in the rotation of early-type stars.

The role of Boyarchuk in the preparation and realization of the major space experiment "Astron" was very great. He was not only the scientific supervisor for the project but also directly participated in the development of the space ultraviolet telescope, the creation of the complex of scientific instruments, the assembly and tuning of the telescope at the Crimean Astrophysical Observatory, the composition and realization of the scientific program, and the development and execution of methods for the reduction of a large fraction of the observational material obtained. Important results were acquired in connection with measurements of the spectral energy distributions of the earliest-type stars, the discovery of white dwarfs in symbiotic systems, estimates of the gradients of the outflow velocities of hot stars, observations of the radiation of active galactic nuclei, and studies of active processes on red dwarfs. The observations of the evolution of the rate of outflow of material from Halley's comet during its approach toward and recession from the Sun are of special interest, as is the detection of a gradient in the overabundance of heavy elements in the expanding shell of Supernova 1987A. Boyarchuk received a State Prize for his role in the creation of the "Astron" space observatory.

Currently, Boyarchuk is the scientific supervisor of a new space project to build a large ultraviolet telescope designed to obtain high-resolution spectra, high-quality images, and polarimetric data—the "Spektrum UV" project. However, the interests of Boyarchuk in the area of space experiments are not limited to astrophysical investigations—a new type of space optical angular interferometer was recently developed under his supervision (the "Zodiak" project).

Boyarchuk expends much strength and energy on various organizational activities. He has been associated with the supervision of major scientific organizations for more than 30 years. In recent years, he has held positions of responsibility in the Presidium of the Russian Academy of Sciences, as the Academic Secretary of the Division and the Primary Assistant to the Chairman of the Council of the Russian Academy of Sciences on Space Issues, and has also had numerous other responsibilities as a member of various committees, councils, commissions, and editorial boards.

The widespread international recognition of the scientific activities of Boyarchuk is testified to by his election as President of the International Astronomical Union and also by his membership in many prestigious foreign and international academies and societies.

Boyarchuk is the author of more than 250 scientific articles and several monographs. His services have been acknowledged, in particular, by a "Sign of Honor," "Order of Honor," and the order "Service for the Motherland."

Boyarchuk has educated numerous students, many of whom have themselves gone on to become authoritative figures in astrophysics. He is able to attract the attention of colleagues with whom he is working to the solution of the most interesting scientific problems. His exceptional benevolence toward others and unpretentiousness in relations, the ability to make weighty and purposeful decisions and carry them out with firmness of will and adherence to principles, and intuition and exceptional wisdom in evaluating situations and problems act as a magnetic to those working around him. Aleksandr Alekseevich is a modest man with a strong sense of decency who is worthy of great authority and the sincere respect of his colleagues and friends.

The collectives of the editorial board and editors of *Astronomicheskiĭ Zhurnal*, the Institute of Astronomy of the Russian Academy of Sciences, and the International Academic Publishing Company "Nauka" congratulate Aleksandr Alekseevich on the occasion of this jubilee and wish him health, happiness, success in everything, and future scientific accomplishments as great as those already attained.

Astronomy Reports, Vol. 45, No. 6, 2001, pp. 417–427. Translated from Astronomicheskiĭ Zhurnal, Vol. 78, No. 6, 2001, pp. 485–497.

Interstellar Medium Surrounding the WO Star in the Galaxy IC 1613: New Optical and Radio Observations

T. A. Lozinskaya[1], A. V. Moiseev[2], V. L. Afanas'ev[2], E. Wilcots[3], and W. M. Goss[4]

[1]*Sternberg Astronomical Institute, Universitetskiĭ pr. 13, Moscow, 119899 Russia*

[2]*Special Astrophysical Observatory, Nizhniĭ Arkhyz, Zelenchukskiĭ raĭon, Karachaevo-Cherkessia, 357147 Russia*

[3]*Department of Astronomy, University of Wisconsin–Madison, 475 N. Charter St., Madison, WI 53706 USA*

[4]*National Radio Astronomy Observatory, P.O. Box O, 1003 Lopezville Road, Socorro, NM 87801 USA*

Received September 30, 2000

Abstract—Observations of the nebula S3 associated with the WO star in the galaxy IC 1613 and of an extended region surrounding S3 are reported. The star and bright core of the nebula were observed with a multipupil fiber spectrograph mounted on the 6-m telescope of the Special Astrophysical Observatory of the Russian Academy of Sciences. Images in the principle spectral lines and integrated spectra of the star and three compact clumps were obtained, and the radial-velocity field constructed. An extended region of the galaxy was observed with the Very Large Array at 21 cm. A giant ring or H I shell enclosing a large fraction of the stellar population in IC 1613 was discovered. The WO star and associated bipolar nebula, which we discovered earlier, lie at the inner edge of the H I ring. A local H I deficiency and two arclike H I ridges were also detected for the first time and probably represent the neutral component of the bipolar shell surrounding the WO star. The two arclike ridges may also have been produced by the collective stellar wind (and supernova explosions?) in OB association No. 9 from the list of Hodge. A scenario for the formation of the extended bipolar feature is discussed, based on the new data. © *2001 MAIK "Nauka/Interperiodica".*

1. INTRODUCTION

Only six WR stars of more than five hundred such objects in the Local Group of galaxies belong to the rare WO class, which represents a very brief final evolutionary stage of massive stars approaching the naked CO-core stage (see [1, 2] and references therein). WO stars are characterized by powerful stellar winds (with terminal velocities reaching ≈5000 km/s [1, 3–5]), and their effective temperatures can be as high as 10^5 K [4, 6–8]. One of these six stars was discovered by D'Odorico and Rosa [9] (see also [10, 11]) in the dwarf irregular galaxy IC 1613. The star was identified by the specific wide bands it produces in the spectrum of the core of the bright emission nebula S3 from the list of Sandage [12]—a giant $29'' \times 9''$ (93×30 pc) H II region. Throughout this paper, we adopt the distance 660 kpc for IC 1613, as derived by Saha *et al.* [13]. The central region of S3 shows a bright He II 4686 Å emission [9, 14, 15]. A detailed spectral analysis of the nebula and a discussion of its chemical composition are presented by Garnett *et al.* [15] and Kingsburgh and Barlow [16]. The nebula S3 was found to be a source of thermal radio emission [17]; the full size at half-maximum intensity of the radio source ($19'' \times 14''$) corresponds to a bright region of the optical nebula visible on deep Hα images taken by Hodge *et al.* [18] and Hunter *et al.* [19].

Our observations made with a scanning Fabry–Perot interferometer mounted on the 6-m telescope of the Special Astrophysical Observatory (SAO) and narrowband Hα and [O III] images taken with the 4-m telescope of the Kitt Peak National Observatory resulted in the discovery of a faint external bipolar feature (hereafter called the bipolar shell) extending far beyond the bright nebula S3 [20, 21]. The sizes of the two external components—the southeastern and northwestern shells—are $35'' \times 24''$ (or 112×77 pc) and $\simeq 60'' \times 70''$ (or $\simeq 190 \times 220$ pc), respectively. Radial-velocity measurements at the maximum and the Hα line halfwidths provide evidence for expansion of the bipolar shell, with the lower limits to the expansion velocities of the southeastern and northwestern shells being 50 km/s and at least 70 km/s, respectively.

Afanas'ev *et al.* [21] proposed a scenario for the formation of the unique bipolar feature by the stellar wind of the WO star, which is embedded in a dense layer at the boundary of a supercavity in the galaxy's H I distribution. We identified this supercavity by analyzing the H I column density distribution in IC 1613 published by Lake and Skillman [22]. At that time, we hypothesized the presence of a dense shell surrounding the supercavity and a physical association with the WO star but were not able to prove that this was the case.

In the current paper, we report the results of new observations of the nebula associated with the WO star in the galaxy IC 1613. We observed the bright core of the nebula S3 using the MPFS multipupil fiber spectrograph mounted on the SAO 6-m telescope (Section 2).

1063-7729/01/4506-0417$21.00

We obtained integrated spectra of individual compact clumps in the central bright region and reconstructed the radial-velocity field from our Hβ and [O III] 5007 Å measurements. We also obtained observations of a large sector of IC 1613 at 21 cm with the Very Large Array (VLA; Section 3). We derived a detailed image of the neutral-gas distribution, which revealed a giant dense ring or H I shell surrounding the supercavity, and showed that the WO star does indeed reside in this dense ring and is physically interacting with it. We also found a local H I deficiency and two extended features, testifying to the presence of a neutral gas component associated with the ionized bipolar shell. In Section 4, we discuss the results of the observations and analyze a possible scenario for the formation of the extended bipolar feature.

2. SPECTROSCOPIC OBSERVATIONS OF THE WO STAR AND NEBULA S3

2.1. Observations and Data Reduction

The spectroscopic observations were made on November 29 and 30, 1999, using the new MPFS panoramic multipupil fiber spectrograph mounted at the primary focus of the SAO 6-m telescope. A description of the spectrograph can be found at the webpage http://www.sao.ru/~gafan/devices/mpfs_main.htm.

Compared to the earlier version of the MPFS [23], the new spectrograph has a larger field of view, wider spectral range, and higher quantum efficiency. The spectrograph uses a 1024×1024 CCD as a detector and allows a set of spectra to be taken simultaneously from 240 spatial elements ("micropupils") forming a 16×15 array in the plane of the sky. The angular size of an image element can be varied from $0.5''$–$1.0''$. A spectrum of the sky background $4.5'$ from the center of the field of view is taken simultaneously. Table 1 gives a log of the MPFS observations.

These observations were reduced using IDL-based software developed by the SAO Laboratory for Spectroscopy and Photometry of Extragalactic Objects. The preliminary data reduction included offset frame subtraction, flat-field correction, cosmic-ray removal, extraction of individual spectra from the CCD images, and wavelength calibration using the spectrum of a He–Ne–Ar lamp. We then subtracted the night-sky spectrum from the linearized spectra and used a number of spectrophotometric standards observed at the same zenith angle as IC 1613 to convert the observed fluxes to an absolute energy scale. We used the same standards to derive the seeing estimates given in Table 1.

Analysis of the observations showed that the data obtained on November 29 and 30, 1999, yielded consistent values for the main parameters measured (line fluxes and velocities). Therefore, we will consider further only the November 30, 1999, data, since they had a higher angular resolution compared to the data of November 29, 1999.

Figure 1a shows an [O III] line image of the central region of the nebula S3 surrounding the WO star from the data of [21], together with the boundaries of the field of view of our new MPFS observations.

2.2. Analysis of the Field Spectroscopy Results

The WO star

We obtained the integrated spectrum of the WO star by co-adding 24 individual spectra, which exhibited the broad emission bands characteristic of Wolf–Rayet stars.

During the flux measurements, we fitted the emission lines using superpositions of two to six Gaussians; the resulting flux and equivalent-width estimates are summarized in Table 2. Note that the errors quoted in this table do not include uncertainty in the continuum level, which could contribute systematic errors to the equivalent widths. For comparison, this table also gives the fluxes and equivalent widths of the corresponding lines from [16].

We observed a narrower spectral interval than Kingsburgh and Barlow [16]; it is clear from Table 2 that the two sets of observations do not show significant discrepancies. The differences between the equivalent widths are due primarily to the different methods used to determine the continuum level (unlike Kingsburgh and Barlow [16], we did not take into account the nebular continuum component). Our flux estimates are higher than those of [16] for most of the lines. This is likely due to the fact that our panoramic detector collected all the light from the star, whereas a long slit whose width ($1''$) was comparable to or smaller than the image size was used in [16]. To test this hypothesis, we integrated the spectra of the star only over the lenses lying within a $1'' \times 5''$ rectangle aligned along PA = 55°, i.e., in the direction of the slit used in [16]. The resulting WO-star line fluxes, indeed, proved to be a factor of 1.5–2 lower, on average, than the fluxes listed in Table 2. Moreover, as we show below, the emission-line bright-

Table 1. Log of MPFS observations

Date	Size of micropupil	Field of view	Spectral interval, Å	δλ, Å	Exposure, s	Seeing
Nov. 29, 1999	$1''$	$16'' \times 15''$	4450–7050	8	7200	$2''.7$
Nov. 30, 1999	0.75	12×11.3	4450–7050	8	7200	1.8

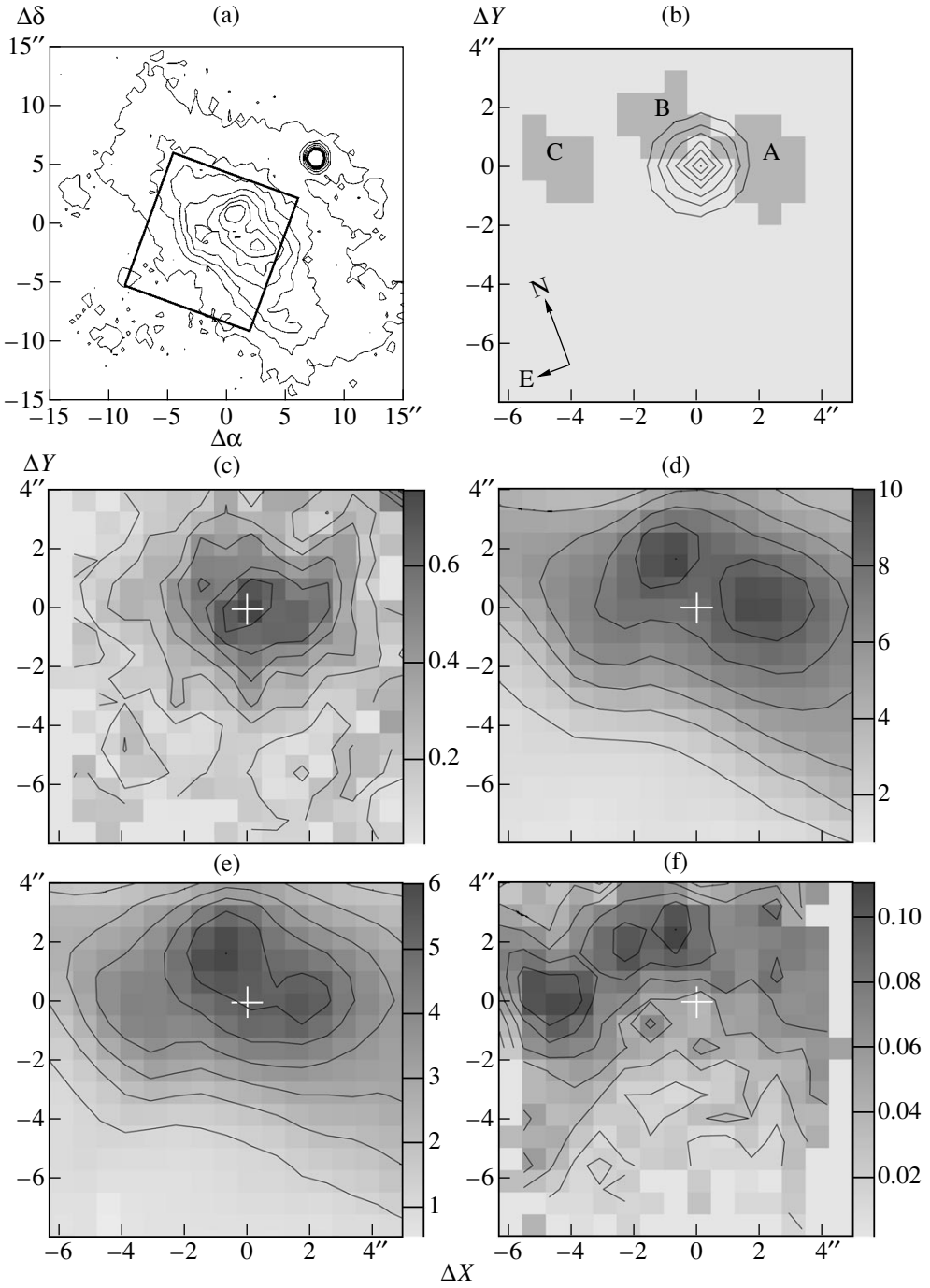

Fig. 1. (a) [O III] image of the nebula surrounding the WO star, adopted from [21]. The frame shows the MPFS field of view for the observations described in this paper. (b) MPFS observations. Isophotes show the brightness distribution in the C IV 5801 Å line emitted by the WO star. Also indicated are the positions of emission clumps. (c), (d), (e), and (f): Images and isophotes of the nebula in the He II 4686 Å, [O III] 5007 Å, Hα, and [S II] 6717 + 6731 Å emission lines, respectively. The cross indicates the position of the WO star. Surface brightness is in units of 10^{-15} erg cm^{-2} s^{-1} arcsec^{-2}.

ness peak in the nebula does not coincide with the position of the star. This could have led to an offset during the positioning of the narrow slit on the star in [16], resulting in further underestimation of the line fluxes.

We constructed images in the C IV + He II 4659 Å, O V 5590 Å, and C IV 5801 Å emission lines by integrating the spectra over the intervals 4600–4725, 5535–5653 and 5735–5850 Å, after subtraction of narrow nebular line components blended with the WO-star lines. The centroids of all the images agree to within ±0.05″ and also agree with the centroid of a continuum image made in the vicinity of 6100 Å. We estimate the

Table 2. Fluxes and equivalent widths of emission lines in the spectrum of the WO star

λ, Å	Line	F, erg cm^{-2} s^{-1}		EW, Å	
		this paper	[16]	this paper	[16]
4659	C IV + He II	2.56×10^{-14}	1.48×10^{-14}	360 ± 25	330 ± 20
5290	O VI	9.50×10^{-16}	1.26×10^{-15}	13 ± 2	55
5411	He II + C IV	1.28×10^{-15}	5.5×10^{-16}	17 ± 2	30
5470	C IV	3.46×10^{-16}	4.2×10^{-16}	4 ± 1	20
5590	O V	4.04×10^{-15}	2.46×10^{-15}	62 ± 11	120
5801	C IV	2.10×10^{-14}	1.41×10^{-14}	420 ± 97	690 ± 40

FWHM of these emission-line images of the WO star to be 1.85 ± 0.05″, 1.84 ± 0.09″, and 1.67 ± 0.03″, respectively, consistent with the seeing estimate of 1.″8 obtained for the standard star (Table 1). Note that, due to certain specific features of the spectrograph, the images constructed from the micropupil array are slightly elongated (1:1.15) along the *x*-axis (Fig. 1b). Therefore, all our FWHM estimates are based on measurements in the *y*-direction.

The continuum image of the WO star was somewhat more extended (FWHM = 2.2″ ± 0.15″) and exhibited a faint base. (This could indicate the presence of a compact cluster made up of several stars, but firm conclusions require further observations.)

Structure and Emission Spectrum of S3

We constructed an entire series of monochromatic images of the bright core of the nebula in the He II 4686 Å, [O III] 5007 Å, [S II] 6717 + 6731 Å, and Hα lines by obtaining Gaussian fits to the emission lines. The results are shown in Figs. 1c–1f. All the line profiles are fit well by single Gaussians and do not show any systematic deviations. Note, however, that the expected relative gas velocities (up to 100 km/s in the bright core [21]) are appreciably lower than the spectral resolution of our data (FWHM = 350–450 km/s).

It is evident from Fig. 1 that the morphology of the nebula is appreciably different in different lines. For example, the He II brightness peak is coincident with the position of the WO star; the He II brightness decreases with distance from the star, and the full size of the emission region is 10″ × 9″. The situation is quite different in the brighter [O III] and Hα lines and also in the [S II] lines: the corresponding images exhibit several bright clumps 2″–3″ from the star (Fig. 1). The [O III] and Hα images show two well-defined bright clumps north and northwest of the star (marked A and B, respectively, in Fig. 1b) and a more extended clump northeast of the star (clump C in Fig. 1b). This extended clump is especially prominent in the [S II] images, where clump A cannot be seen at all.

We discovered the clumpy structure of the S3 core in our earlier study [21], based on uncalibrated [O III] and Hα images of the region. However, having no emission spectra for the clumps, we mistook the WO star for a clump (clump *2* in [21]). (Clumps A and B from our new observations correspond to clumps *3* and *1*, respectively, from [21]; clump C, which can be confidently identified only in the [S II] lines, was not discovered earlier in the [O III] and Hα images.)

We obtained the integrated spectra of clumps A, B, and C; the positions of the image elements whose spectra were co-added in each clump are shown in Fig. 1b. Table 3 gives the relative line intensities for the three clumps, corrected for selective extinction. We assumed $c(\mathrm{H}\beta) = 0.1$ and E(B–V) = 0.069, in accordance with [16]. For comparison, Table 3 also presents the data of [16] for the integrated spectrum of the central region of S3.

2.3. Ionized Gas Velocities in the Core of S3

We used the resulting spectra to construct the radial-velocity field for the central part of the nebula S3. We determined the velocity fields from measurements made in the main spectral lines from Gaussian fits to the corresponding line profiles. Analysis of the night-sky spectrum showed that, after linearization of the spectra, there remained systematic velocity variations in the night-sky lines across the field of ±0.1–0.15 channels, i.e., about 15 km/s. We corrected our emission-line velocity fields for this systematic offset; Fig. 2 shows the results.

We used the resulting velocity fields to estimate the mean velocities in various lines for clumps A, B, and C and for the nebula region projected onto the WO star. In this last case, we used the same set of lenses used when co-adding the spectrum of the star (see Section 2.1). The results are summarized in Table 4, where the quoted errors correspond to the velocity dispersion within individual spatial elements.

The resulting mean clump velocities are consistent with the mean velocity of the nebula S3 as a whole derived from our Fabry–Perot interferometric measurements ($V_{\mathrm{hel}} = -216 \pm 1$ km/s) [21] (taking into account possible systematic absolute calibration errors of 15–20 km/s for the interferometric observations) and are in full agreement with the measurements of Tomita *et al.* [24], based on a single spectrogram of S3: $V_{\mathrm{hel}} = -235$

Table 3. Line intensities for clumps A, B, and C

λ, Å	Line	$I/I(H_\beta)$, %			
		A	B	C	[16]
4686	He II	31.1 ± 0.7	28.3 ± 0.8	12.2 ± 0.8	23.1
4711	[Ar IV]	7.1 ± 0.7	7.9 ± 0.8	3.1 ± 0.8	4.5
4740	[Ar IV]	6.3 ± 0.7	6.5 ± 0.7	5.8 ± 0.8	5.62
4861	Hβ	100.0	100.0	100.0	100.0
4959	[O III]	174 ± 5	168 ± 8	164.0 ± 2	188
5007	[O III]	519 ± 13	511 ± 20	489 ± 6	–
5876	He I	4.1 ± 0.3	4.6 ± 0.7	5.4 ± 0.8	7.1
6542	[N II]	1.4 ± 0.2	1.8 ± 0.3	2.3 ± 0.3	–
6563	Hα	273 ± 4.0	283 ± 10	273 ± 5	276
6583	[N II]	2.4 ± 0.2	2.8 ± 0.4	4.6 ± 0.3	6.4
6717	[S II]	8.9 ± 0.3	10.2 ± 0.2	15.2 ± 0.9	8.73
6731	[S II]	6.9 ± 0.3	7.6 ± 0.2	10.4 ± 0.8	5.78
		$(I)\,H\beta \times 10^{-14}$, erg cm^{-2} s^{-1}			
		1.5	1.2	7.7	

to –230 km/s. We show below (see Section 3) that the velocities of the densest H I clouds in the vicinity of S3 are ≈ –230 km/s or differ from this value by less than 10 km/s.

Two cone-shaped regions where the velocities are systematically different from the mean are immediately apparent in Fig. 2. Our [O III] line measurements enable identification of the region where the velocities differ from the mean value by 40–50 km/s. Both deviations from the mean velocity agree with the velocity variations in the central part of the bright nebula S3 presented in [21], based on interferometric Hα measurements. Note that the cone-shaped regions originate at the position of the star, a pattern that, generally speaking, might indicate an asymmetric stellar wind. However, firm conclusions require further observational evidence, since such velocity variations could also be a consequence of the inhomogeneous structure of the interstellar medium in the near environment of the star.

3. RADIO OBSERVATIONS IN THE 21-CM LINE

3.1. Observations and Data Reduction

We constructed a high angular resolution VLA H I map covering an extended region of the galaxy IC 1613, including the WO star and the associated bipolar shell (this was part of a larger project to investigate the neutral-gas structure and kinematics in IC 1613 [25]). The maps shown below were constructed from combined B-, C-, and D-array VLA observations with a velocity resolution of 2.57 km/s. The data were Hanning smoothed, subjected to the usual calibration procedure, and made into maps using the AIPS package.

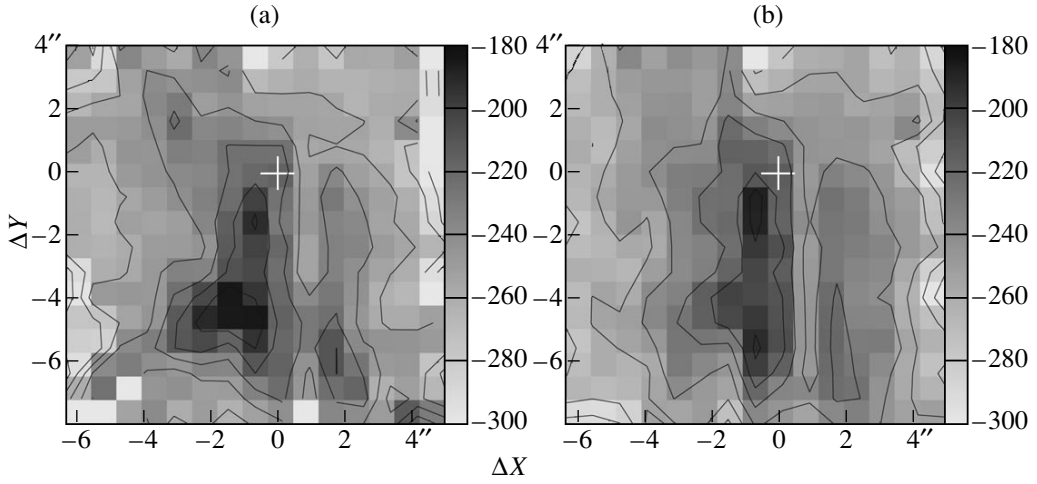

Fig. 2. Ionized gas velocity field in the (a) Hβ and (b) [O III] 5007 Å lines based on the MPFS observations. The cross indicates the position of the WO star. The velocity scale is in km/s.

Table 4. Mean velocities for clumps A, B, and C and toward the WO star

λ, Å	Line	V_{hel}, km/s			
		A	B	C	WO
4686	He II	−213 ± 14	−227 ± 22	−186 ± 30	−214 ± 21
4861	Hβ	−250 ± 10	−242 ± 13	−252 ± 7.	−231 ± 18
4959	[O III]	−247 ± 11	−241 ± 13	−257 ± 6.	−230 ± 18
5007	[O III]	−241 ± 8.	−238 ± 17	−253 ± 10	−225 ± 18
6563	Hα	−246 ± 6.	−248 ± 5.	−242 ± 4.	−251 ± 6.
6717	[S II]	−247 ± 23	−225 ± 13	−224 ± 11	−253 ± 26
Mean		−241 ± 6	−237 ± 4	−236 ± 11	−234 ± 6

The results are represented in the form of a data cube with angular resolution $7\farcs4 \times 7\farcs0$, which corresponds to a linear resolution of ~23 pc.

Figure 3 shows the H I distribution for the eastern sector of the galaxy constructed using these data. A well-defined giant cavity (supercavity) surrounding a large fraction of the stellar population of IC 1613 is immediately apparent. This giant, low surface brightness region of 21-cm emission is also visible on the map of Lake and Skillman [22]. Earlier [21], we suggested that this region was deficient in neutral gas because it had been swept out, implying that the supercavity should be surrounded by a dense, wind-blown shell. Figure 3 shows that such a shell or ring of neutral gas does, indeed, exist and that the WO star resides in a dense gas layer near its inner edge.

The angular size of the supercavity is about 5′, corresponding to a linear size of 1 kpc. The characteristic thickness of the shell is $\Delta R \simeq 1'$–$2'$, or 200–350 pc.

A sketch of the bipolar ionized shell surrounding the WO star and its relative position with respect to the H I supercavity are shown on an enlarged scale in Fig. 4, which presents the southeastern sector of the H I ring.

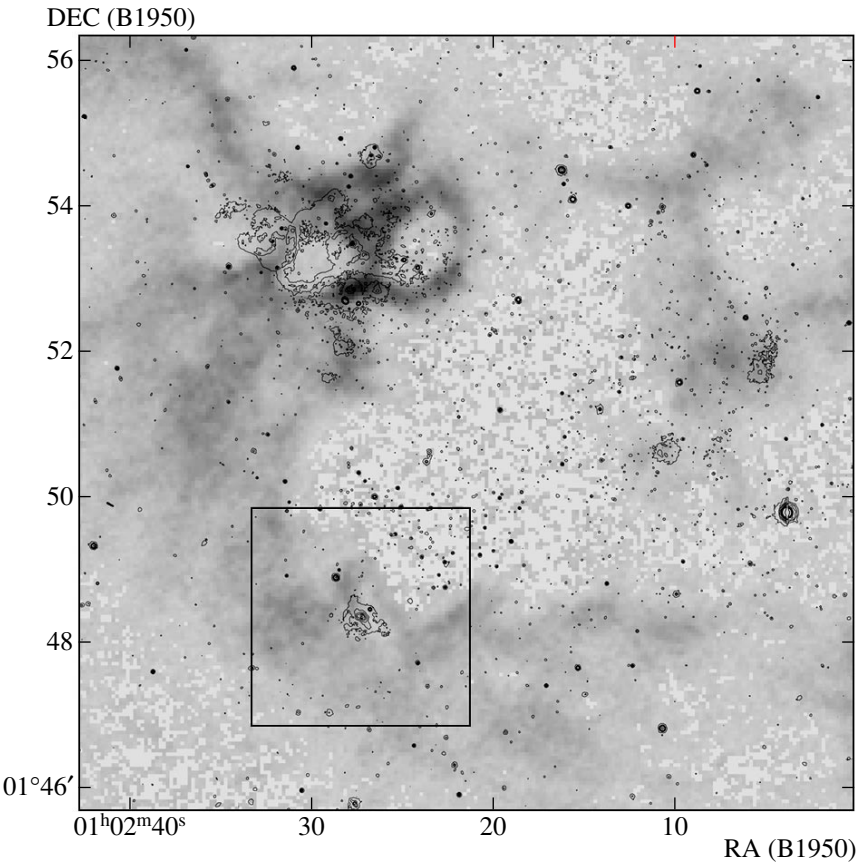

Fig. 3. Eastern sector of the galaxy IC 1613: brightness distribution in the 21-cm line from the VLA data (gray scale) and Hα isophotes (based on the observations made with the 4-m KPNO telescope). An enlarged-scale version of the framed region surrounding the nebula S3 and WO star is shown in Fig. 4.

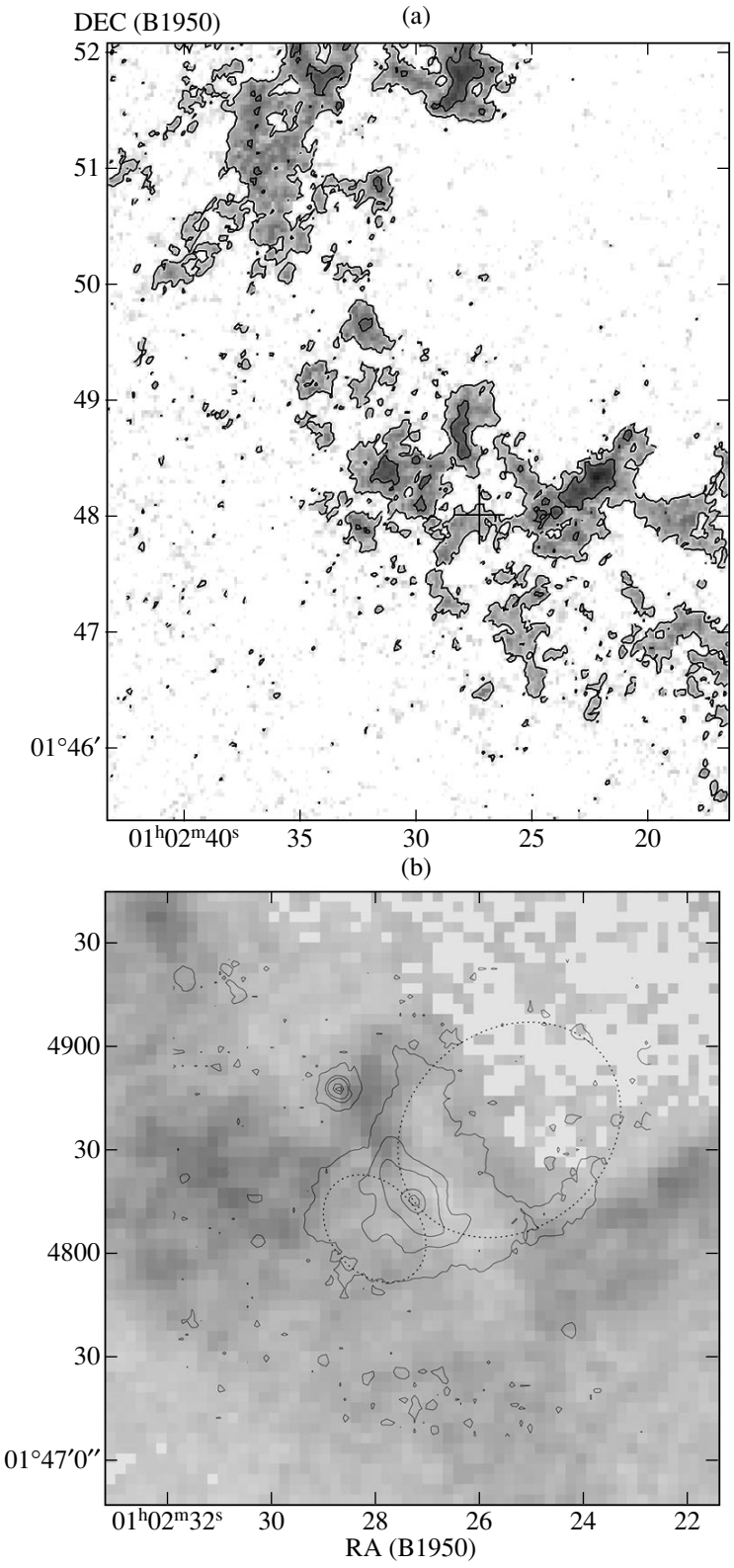

Fig. 4. (a) Southeastern sector of the dense H I ring (including the framed region in Fig. 3). The contours correspond to H I column densities of $N(\mathrm{H\ I}) = (2, 6, 18) \times 10^{20}$ cm^{-2}. The cross indicates the position of the WO star. (b) Sketch of the bipolar ionized shell associated with the WO star (isophotes adopted from [21]); the Hα isophotes correspond to brightness levels of 0.028, 0.2, 0.4, 1.0, and 2.0×10^{-15} erg cm^{-2} s^{-1} arcsec^{-2}. The H I distribution is superimposed as a gray-scale image.

Table 5. Parameters of H I clouds in the vicinity of the bipolar shell

Cloud	RA (B1950)	DEC (B1950)	N(H I), 10^{20} cm^{-2}	M, $10^4 M_\odot$
a	1 2 28	1 47 55	5	~4
b	1 2 31.5	1 48 20	8	~3
c	1 2 21–24	1 48 08	20	10
d	1 02 26	1 48 20	7	2
e	1 02 28	1 48 30–60	9	6

This figure shows that the elongated core of the ionized bipolar shell (previously known as S3) and its bright southeastern component are located in a dense region of the ring, whereas the extended, faint northwestern component is in the low-density medium inside the supercavity.

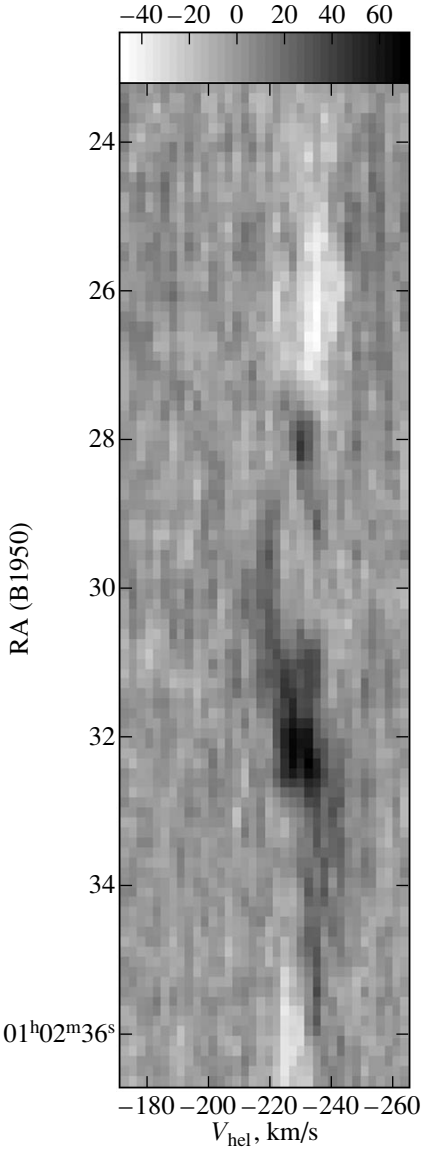

Fig. 5. H I radial-velocity variations in a right-ascension band from the VLA observations (see text). The fluxes are in mJy/beam.

Figure 4 clearly shows a local decrease in the 21-cm brightness, filled by the ionized gas of the core and southeastern component. We can also see two prominent, extended H I features just on the outside of the two sides of the northwestern component of the ionized shell, which reproduce the shape of the shell. This structure probably provides evidence for a local neutral shell surrounding the bipolar shell.

The parameters of the most prominent H I clouds forming the local neutral shell surrounding the ionized bipolar feature are summarized in Table 5, which presents the central coordinates, total mass, and maximum column density of each cloud.

3.2. Neutral Gas Velocities

In order to reveal the possible effect of the expansion of the local neutral shell, we constructed the radial-velocity distribution within a right-ascension band passing through the WO star (Fig. 5). The band is 200″ wide and therefore includes all clouds H I making up the local shell. This distribution clearly demonstrates velocity variations with distance from the star that are typical of an expanding shell (the so-called "velocity ellipse") at right ascensions from $01^h02^m28^s$ to $01^h02^m31^s$. This region corresponds to the part of the local H I shell that is east of the WO star; the characteristic radius of this "half-shell" is 100–140 pc. The velocity difference between the two sides of the neutral shell is ~20 km/s, suggesting an expansion velocity of ~10 km/s. The velocities of the densest "unaccelerated" H I clouds in a large region surrounding the WO star are $V_{hel} = -230 \pm 5$ km/s.

4. DISCUSSION

The results of spectroscopic observations of the WO star and the central region of the nebula S3 reported in this paper are in full agreement with earlier observations, within the errors limits, when the different slit locations are taken into account. The spectra of the compact clumps identified in this paper do not differ significantly from the those of the nebula S3 (see [15, 16] and references therein). The relative line intensities listed in Table 3 are suggestive of a typical H II region ionized by a star with a high effective temperature. The observed differences between the spectra of the three clumps could be due to different excitation conditions: distance from the exciting star and electron density. No shock signatures were found either in the emission spectra (the [N II] and [S II] lines are weak) or in the mean velocities of the bright clumps. The ionized gas velocities of the clumps in the central core of the nebula agree with velocity measurements of neutral gas clouds in the vicinity of the bipolar shell.

Electron Density and He Abundance in the Nebula Core

The relative intensities of the [S II] 6717/6731 Å doublet can be used to estimate the electron density in the three bright clumps identified in this paper. We determined the electron densities in clumps A, B, and C using formulas adopted from [26], assuming that the electron temperature of the nebula is T_e =17000 K (as determined in [16] from the [O III] 4959/4363 Å line intensities). The resulting values are listed in Table 6.

We derived the He abundance in the nebula from He I and He II line intensities of individual clumps using the diagnostic relations and recombination coefficients for hydrogen and helium from [27]. At T_e = 17000 K we determined the relative helium abundances $N(He^+)/N(H)$ and $N(He^{++})/N(H)$ and the total helium abundances $N(He)/N(H)$ (in number) of the clumps. The results are given in Table 6, which also lists data adopted from [16]. We can see that our abundances coincide with those of [16] and are in good agreement with the estimate of [10]: $N(He)/N(H) = 0.073 \pm 0.009$. (In both [10] and [16], the He abundances were obtained from the spectrum of the entire bright core of the nebula without subdividing it into individual clumps.)

Table 6. Electron density and He abundances of clumps A, B, and C

Parameter	A	B	C	[16]
n_e, cm^{-3}	170	80	≤30	100
$N(He^+)/N(H)$	0.051	0.057	0.067	0.057
$N(He^{++})/N(H)$	0.028	0.025	0.011	0.025
$N(He)/N(H)$	0.079	0.082	0.078	0.082

Velocity of the Stellar Wind of the WO star

One of the major parameters determining the structure and kinematics of the interstellar medium at large distances from WR stars is the stellar-wind velocity. Kingsburgh *et al.* [2] have shown (see also [16]) that the halfwidth of the C IV 5801 Å line at zero intensity is a good estimator of the terminal wind velocities of WR stars. The C IV line halfwidth at zero intensity measured from our spectra for the WO star yields a terminal wind velocity of V_w = 2910 km/s, which is virtually coincident with the value 2850 km/s obtained in [16], given that the accuracy of our measurements is determined by the width of the spectral channel (~130 km/s). We thus confirm the conclusion of Kingsburgh and Barlow [16] that the terminal wind velocity of the WO star in IC 1613 is the lowest among the six objects of this class currently known in the Local-Group galaxies.

Large-Scale Structure of the Interstellar Medium

In principle, the giant H I ring shown in Fig. 3 could be the projection onto the plane of the sky of a shell or torus. A torus could be the result of the wind-blown supercavity breaking out of the gaseous disk of the galaxy. In both cases, the neutral gas ring surrounding the supercavity displays a characteristic filamentary structure. The filamentary system making up the H I ring bifurcates at its southeastern end. A system of arclike filaments with characteristic lengths of 1′–1.5′, or 200–300 pc, is also apparent. This filamentary pattern undoubtedly testifies to the action of dynamically active processes that are responsible for the formation of the supercavity and the surrounding dense ring or shell. This large-scale structure apparently formed as the result of a burst of star formation in the region. However, determining the nature of this burst is a separate problem which lies beyond the scope of this paper. Of interest to us here is the very existence of such a dense shell or torus surrounding the supercavity, since we consider this large-scale mass distribution to be responsible for the unique bipolar structure of the extended ionized shell associated with the WO star.

Lozinskaya [20] suggested that the bipolar structure of the ionized shell surrounding the WO star might be the result of a strong stellar wind breaking out of the dense gas layer. Earlier [21], we associated this dense layer with a hypothetical wind-blown shell, which we suggested should surround the giant H I-deficient region in IC 1613 seen on the map of Lake and Skillman [22]. However, only in this paper have we finally been able to provide some evidence supporting this hypothesis. The following factors form our principal arguments.

(1) One piece of evidence is the relative orientation of the bipolar ionized shell with respect to the H I supercavity. It is clear from Fig. 4 that the bright core of the nebula is extended along the boundary of the dense H I ring; the smaller southeastern component of the ionized bipolar shell lies inside a dense neutral gas layer, and the extended northwestern component lies in the low-density medium inside the supercavity.

(2) Afanas'ev *et al.* [21] showed that the southeastern component is brighter than the northwestern component and also has a lower expansion velocity.

(3) The local cavity and extended H I features whose discovery is reported in this paper testify to the presence of a neutral shell surrounding the ionized bipolar shell, providing direct evidence for a physical association of the WO star and the ionized bipolar shell with the supercavity and dense H I ring (the only alternative being a chance projection).

The gas density in the clouds making up the local H I shell surrounding the bright central and southeastern components of the ionized nebula can be derived from our maximum column density and total mass estimates, assuming that the clouds have the same sizes in the line-of-sight and transverse directions. The clouds that make up the local neutral H I shell have irregular structures. Clouds a, c, and e in Table 5, which make up the

expanding part of the H I half-shell, have lengths in the plane of the sky ranging from 40 to 120 pc. For a column density of (5–9) × 10^{20} cm^{-2}, this yields a characteristic density of $n_{\rm H\,I} \simeq 1.5$–7.5 cm^{-3}.

For comparison, we present estimates of the average density of ionized gas in this nebula: Davidson and Kinman [10] found $n_e = 8.5$ cm^{-3} based on the Hβ emission of the central 6″ of the nebula S3; Kenicutt [28] reports $n_e \simeq 1$ cm^{-3} based on a study of the integrated Hα emission of the bright nebula; and Goss and Lozinskaya [17] found $n_e = 3.5$ cm^{-3} from their analysis of its thermal radio emission.

If the H I clouds surrounding the bright central and southeastern components of the bipolar ionized shell are, indeed, parts of a shell of neutral gas blown out by the stellar wind, the radius and expansion velocity of the expanding section east of the WO star should be 100–140 pc and about 10 km/s, respectively (see Section 3). In the standard model [29, 30], we find the kinematic age of the wind-blown neutral shell to be t = (6–8) × 10^6 yr. (Note that this estimate depends neither on the stellar wind power nor on the density of the surrounding gas.) This age substantially exceeds the duration of the final WO stage and corresponds to the main-sequence lifetime of a massive star ($M \geq (30$–$40 M_\odot)$). We thus conclude that the local neutral shell surrounding the bright southeastern and central components of the ionized nebula could have been produced by the stellar wind of the WR progenitor when it was still a main-sequence star. Note that, earlier [21], we concluded that the ionized bipolar shell was blown out by the successive action of the stellar wind from the central star, first at the WR and then at the WO stage.

Our estimates indicate that the terminal velocity of the stellar wind of the WO star reaches 3000 km/s (see Section 2); a mass-loss rate of 2.9 × $10^{-5} M_\odot$/yr was derived in [16] based on the relation between the He II line luminosities and the mass-loss rates for two WO stars. Accordingly, the power of the stellar wind of the WO star in IC 1613 is $L_w \simeq 10^{38}$ erg/s. In all likelihood, the wind power was a factor of two to three lower during the earlier WR stage (WR stars typically have terminal velocities of 2000 km/s), but the duration of the WR stage ($\simeq 5 \times 10^5$ yr) is at least an order of magnitude longer than that of the WO stage. The power of the stellar wind of the main-sequence progenitor could have been two orders of magnitude lower than at the final Wolf–Rayet stage, however, the main-sequence lifetime was at least an order of magnitude longer than the Wolf–Rayet stage.

The formation of the wind-blown shell is determined by the standard relation $R = 28\,(L_{36}/n_0)^{1/5} t_6^{3/5}$, where L_{36} is the power of the stellar wind in units of 10^{36} erg/s, n_0 is the density of the surrounding gas, R is the radius in pc, and t_6 is the time in units of 10^6 yr [29, 30]. We can easily see that, although the mechanical energy inputs from the massive star during the WR and WO stages are comparable, the stellar wind produced during the main-sequence stage is capable of creating a larger shell than the powerful but short-lived stellar wind at the final stage. Therefore, this latter wind serves as an additional source of mechanical energy in an already formed, slowly expanding shell.

Our results for the two extended arclike H I clouds surrounding the northwestern component of the ionized shell are much less conclusive. On the one hand, these formations could be the result of the stellar wind of the WO star and its progenitor breaking into the tenuous gas inside the supercavity. Our measurements, indeed, indicate that the H I surface density inside the supercavity is at least an order of magnitude lower than in the clouds listed in Table 5. The thickness of the emitting gas layer can be taken to be twice that of the supershell in the plane of the sky, i.e., about 3′–4′ (600–700 pc), according to Fig. 3. Accordingly, we find the mean gas density in the supercavity to be $\simeq$0.04–0.05 cm^{-3}. If the observed ring-shaped H I distribution is the projection of a thick torus rather than a shell, the size of the emission region should be even larger, so that the above estimate should be considered an upper limit to the gas density inside the supercavity. The same standard relation yields a radius of $R \simeq 180$ pc for a shell blown out in the tenuous medium of the estimated density over the time $t = 7 \times 10^6$ yr found above. This agrees with the observed size of the northwestern part of the local shell outlined by two extended arc-like H I clouds in Fig. 4.

On the other hand, the formation of such an arc-like structure outlined by these extended H I clouds could be the result of the collective stellar winds (and possible supernova explosions) from association No. 9 of the list of Hodge [31], which is adjacent to and inside the supercavity. (This association is the largest in size and the richest in the galaxy.) In this case, the stellar wind and ionizing radiation of the WO star act inside this already formed arc-like feature.

We plan a detailed analysis of the kinematics of the ionized and neutral gas components in this region and a comparison with the stellar population. This study should lead to unambiguous conclusions about the nature of the arclike formation and the possible genetic relation between the WO star and the association.

5. CONCLUSIONS

We have observed the central part of the nebula S3 surrounding the WO star (field spectroscopy with the 6-m telescope) and an extended surrounding region several kpc in size (21-cm VLA observations). We have mapped the brightness of the central nebula in the main spectral lines and constructed the radial-velocity distribution based on Hβ and [O III] 5007 Å line measurements.

We identified three compact clumps and determined their integrated spectra, mean velocities, and electron

densities. Our spectroscopic data for both the WO star and the central region of S3 are in agreement with previous observations (see [15, 16] and references therein). The relative line intensities in the spectrum of the nebula are indicative of pure recombination emission from a highly excited H II region.

We analyzed the structure and kinematics of the neutral gas in an extended region around IC 1613 that includes the WO star and the associated ionized bipolar shell. A giant, dense shell or toroidal formation of neutral gas about 1.5 kpc in size surrounds the H I supercavity. This giant structure was very likely produced by bursts of star formation in this region.

We also discovered for the first time a local deficiency in the brightness of the 21-cm line and two extended H I features, providing evidence that the extended ionized bipolar shell associated with the WO star [20, 21] is, in turn, surrounded by a local shell of neutral gas. The mass and expansion velocity of this shell indicate that it was blown out by the stellar wind of the WO progenitor when it was still a main-sequence star.

Our new observations support a scenario in which the extended bipolar structure was produced by the stellar wind of the WO star residing in the dense "wall" of the supercavity. The arclike structure of the extended H I clouds just outside the faint northwestern component of the ionized shell might have been shaped by the collective stellar wind (and supernova explosions?) of Hodge's [32] association No. 9. In this case, the wind and ionizing radiation of the WO star act inside this previously formed arclike structure.

ACKNOWLEDGMENTS

This work was supported by the Russian Foundation for Basic Research (project no. 98-02-16032) and the Astronomy State Science and Technology Program (project no. 1.3.1.2). The National Radio Astronomy Observatory is a facility of the National Science Foundation operated under cooperative agreement with Associated Universities, Inc. We are grateful to E. Blanton for sharing the Hα line image of IC 1613 taken at Kitt Peak National Observatory, E.E. Gerasimenko for supporting the observations at the 6-m telescope of the Special Astrophysical Observatory of the Russian Academy of Sciences, and the Program Committee of the 6-m telescope for providing the observing time for this project.

REFERENCES

1. M. J. Barlow and D. C. Hummer, in *Wolf–Rayet Stars: Observations, Physics, and Evolution (IAU Symposium 99)*, Ed. by C. W. H. Loore and A. J. Willis (D. Reidel, Dordrecht, 1982), p. 387.
2. R. L. Kingsburgh, M. J. Barlow, and P. J. Storey, Astron. Astrophys. **295**, 75 (1995).
3. A. V. Torres, P. S. Conti, and P. Massey, Astrophys. J. **300**, 379 (1986).
4. M. A. Dopita, P. J. McGregor, T. A. Lozinskaya, and S. J. Rawlings, Astrophys. J. **351**, 563 (1990).
5. V. F. Polcaro, R. Viotti, C. Rossi, and L. Norci, Astron. Astrophys. **265**, 563 (1992).
6. A. Maeder and G. Meynet, Astron. Astrophys. **210**, 155 (1989).
7. J. Melnik and M. Heydari-Malayeri, in *WR Stars and Interrelations with Other Massive Stars in Galaxies (IAU Symposium 143)*, Ed. by K. A. van der Hucht and B. Hidayat (Kluwer, Dordrecht, 1991), p. 409.
8. V. F. Polcaro, F. Giovanelli, R. K. Manchanda, *et al.*, Astron. Astrophys. **252**, 590 (1991).
9. S. D'Odorico and M. Rosa, Astron. Astrophys. **105**, 410 (1982).
10. K. Davidson and T. D. Kinman, Publ. Astron. Soc. Pac. **94**, 634 (1982).
11. T. E. Armandroff and P. Massey, Astrophys. J. **291**, 685 (1985).
12. A. R. Sandage, Astrophys. J. **166**, 13 (1971).
13. A. Saha, W. L. Freedman, J. G. Hoessel, and A. E. Mossman, Astron. J. **104**, 1072 (1992).
14. H. E. Smith, Astrophys. J. **199**, 591 (1975).
15. D. R. Garnett, R. C. Kennicutt, Y.-H. Chu, and E. D. Skillman, Astrophys. J. **373**, 458 (1991).
16. R. L. Kinsburgh and M. J. Barlow, Astron. Astrophys. **295**, 171 (1995).
17. W. M. Goss and T. A. Lozinskaya, Astrophys. J. **439**, 637 (1995).
18. P. Hodge, M. G. Lee, and M. Gurwell, Publ. Astron. Soc. Pac. **102**, 1245 (1990).
19. D. A. Hunter, W. N. Hawley, and J. S. Gallagher, Astron. J. **106**, 1797 (1993).
20. T. A. Lozinskaya, Astrophys. Space Sci. **252**, 199 (1997).
21. V. L. Afanas'ev, T. A. Lozinskaya, A. V. Moiseev, and E. Blanton, Pis'ma Astron. Zh. **26**, 199 (2000) [Astron. Lett. **26**, 153 (2000)].
22. G. Lake and E. D. Skillman, Astron. J. **98**, 1274 (1989).
23. V. L. Afanas'ev, V. V. Vlasyuk, S. N. Dodonov, and O. K. Sil'chenko, Preprint SAO, 1990, no. 54.
24. A. Tomita, K. Ohta, and M. Saito, Publ. Astron. Soc. Jpn. **45**, 693 (1993).
25. Wilcots *et al.* (2000) (in press).
26. M. M. De Robertis, R. J. Dufour, and R. W. Hunt, J. R. Astron. Soc. Can. **81** (6), 195 (1987).
27. A. F. Kholtygin, Astron. Astrophys. Trans. **12** (2–3), 85 (1997).
28. R. C. Kennicutt, Astrophys. J. **287**, 116 (1984).
29. J. Castor, R. McCray, and R. Weaver, Astrophys. J. Lett. **200**, L107 (1975).
30. R. Weaver, R. McCray, J. Castor, *et al.*, Astrophys. J. **218**, 377 (1977).
31. P. W. Hodge, Astrophys. J., Suppl. Ser. **37**, 145 (1978).

Translated by A. Dambis

Astronomy Reports, Vol. 45, No. 6, 2001, pp. 428–433. Translated from Astronomicheskiĭ Zhurnal, Vol. 78, No. 6, 2001, pp. 498–504.

Physical Conditions in Faint Gigahertz-Peaked Spectrum Radio Sources

S. A. Tyul'bashev

Pushchino Radio Astronomy Observatory, Astro Space Center of the Lebedev Institute of Physics, Russian Academy of Sciences, Pushchino, Moscow oblast, 142290 Russia

Received March 13, 2000

Abstract—Weak, compact radio sources (~100 mJy peak flux, $L \sim 1$–10 pc) with their spectral peaks at about a gigahertz are studied, based on the complete sample of 46 radio sources of Snellen, drawn from high-sensitivity surveys, including the low-frequency Westerbork catalog. The physical parameters have been estimated for 14 sources: the magnetic field ($H_\perp$), the number density of relativistic particles (n_e), the energy of the magnetic field ($E_{H_\perp}$), and the energy of relativistic particles (E_e). Ten sources have $E_{H_\perp} \ll E_e$, three have approximate equipartition of the energies ($E_{H_\perp} \sim E_e$), and only one has $E_{H_\perp} \gg E_e$. The mean magnetic fields in quasars (10^{-3} G) and galaxies (10^{-2} G) have been estimated. The magnetic field appears to be related to the sizes of compact features as $H \sim 1/\sqrt{L}$.

1. INTRODUCTION

Compact radio sources with gigahertz-peaked spectra (GPS sources) were distinguished as a separate class in 1982 [1]. They attracted attention due to their unusually high compactness. VLBI observations showed that the bulk of the radio emission comes from regions with linear sizes not exceeding 1 kpc and frequently smaller than 10 pc [2]. In spite of their small sizes, GPS sources have high radio luminosities, $\sim 10^{45}$ erg/s. Optical identifications indicate that these sources are mostly quasars and radio galaxies. The properties of GPS sources are similar to those of compact steep-spectrum (CSS) sources, which have spectral peaks at ~100–300 MHz and linear dimensions not exceeding the sizes of their parent galaxies (10–30 kpc). The main hypotheses about the nature of GPS sources have been reviewed in, e.g., [3–6] and are briefly summarized below.

(1) GPS sources are young, compact objects that will evolve into classical FRI/FRII double sources [7–10].

(2) They are not young, but a very dense interstellar environment prevents them from expanding to "normal" sizes [11–15].

(3) They are old objects that, for some reason, have entered a new phase of their life. This is suggested by the fact that ~20% of GPS sources have emission from halos [5, 16, 17].

(4) They are objects formed by interacting galaxies [8, 9, 11, 17, 18].

Each of these hypotheses is supported by a number of arguments. In this work, we consider the physical conditions in GPS sources and compare them to those in CSS sources.

It is often thought that GPS sources are related to CSS sources [10, 19–21]. It is sometimes supposed that GPS sources are young versions of CSS sources. We have obtained interplanetary-scintillation observations of a sample of 57 CSS sources at 102 MHz. For most of the sample sources, we detected a low-frequency cutoff in the spectrum of the compact (scintillating) component. We have found correlations linking the magnetic-field strength and number density of relativistic particles to the source size and also a correlation between the mean magnetic field and the source type (the magnetic field is weaker in quasars than in galaxies) [22–24]. It is of interest to investigate the possible extension of these dependences to GPS sources.

The basis of the study is the complete sample of faint GPS sources published in the thesis of Snellen [4]. The peak flux densities of typical GPS sources are usually several Jy [1]; therefore, sources with peak fluxes of about 0.1 Jy are fairly faint. This sample includes the faintest GPS sources currently known. It was compiled on the basis of the Westerbork survey at 327 MHz [25] and Green Bank 1.4- and 5-GHz surveys [26, 27]. Additional observations of all GPS candidates were obtained using the VLA and MERLIN. The final sample contains 47 sources. Images in the optical and infrared and multifrequency VLBI observations are available for all sources; optical spectroscopy has been carried out for some of the sources. Various possible interpretations concerning the origin of the sources have been proposed. These results were partially published in [28–30].

1063-7729/01/4506-0428$21.00

2. TECHNIQUE FOR DETERMINING THE PHYSICAL CONDITIONS IN THE NUCLEI OF GPS SOURCES

A low-frequency cutoff in the spectrum of a radio source carries information about the physical conditions in the region that is responsible for the cutoff. Especially abundant physical information can be extracted in the case of a cutoff due to synchrotron self-absorption. Artyukh [31] developed a technique based on the formula of Slysh [32] to estimate the magnetic-field strength $H_\perp$ and relativistic-plasma density n_e without assuming equipartition between the energies of the magnetic field and relativistic plasma, as is usually done when obtaining such estimates. It follows from the formula of Slysh that

$$H_\perp \sim \nu^5 \theta^4 S^{-2} (1+z)^{-1}.$$

Using the angular size θ of the source, the flux near the cutoff in the spectrum S, the frequency ν at which this flux is measured, and redshift z, we can infer the magnetic-field strength $H_\perp$ in the source. Applying this magnetic field strength in the optically thin part of the spectrum, we can estimate the relativistic plasma density. The accuracy of the method is one–two orders of magnitude [31]. The main errors are associated with an inaccuracy in the source angular sizes and possible inhomogeneity of the sources.

This technique was developed in application to low-frequency spectral cutoffs (cutoff frequencies of about 100 MHz); however, it can be used without restriction for synchrotron cutoffs at any frequency. It is only necessary to demonstrate that a cutoff is indeed due to synchrotron self-absorption. This technique was thoroughly tested for low-frequency cutoffs on a large sample of CSS sources [22–24].

There are three fundamental points related to the application of this technique to the sample studied.

(1) The method tacitly assumes that the angular size of a compact feature observed at high frequencies does not change with frequency. If the size of the compact source depends on the observing frequency, the estimates will be erroneous. For the GPS sources we are studying, VLBI observations were carried out at 5 GHz and for most sources also at ~15 GHz. However, their spectra typically peak at ~1.5 GHz. Hence, we must be certain that the compact source seen at 1.5 GHz has the same angular size as at 5 GHz. Studies of a sample of CSS sources [22–24] have shown that, first, features studied using VLBI may disappear at lower frequencies (due to a spectral cutoff); however, their shapes and sizes depend little on the observing frequency. Second, most GPS sources have no halo, so that the integrated spectrum reflects the spectrum of the compact emission. Some GPS sources have a modest halo (containing ~5–10% of the total flux density); however, the overwhelming majority of GPS sources have no halo [5, 16, 17]. A faint halo can distort the spectrum of the compact feature, but it cannot considerably shift the spectral peak. The total halo flux density is low and, in the formula used to estimate the physical conditions, $H_\perp \sim S^{-2}$; thus, a 20% error in the estimated flux density can reduce $H_\perp$ by a factor of 1.5. Compared to the overall accuracy of the technique of one–two orders of magnitude, this is not significant. Thus, we can use the integrated spectrum of a GPS source when the spectrum of the compact component and the integrated spectrum coincide at a high frequency (5 GHz).

We must also consider the probable appearance of new features at frequencies below 5 GHz. These can shift the spectral cutoff toward lower frequencies and can also flatten the spectrum. However, the narrowness of the spectral peaks for the sample GPS sources is not consistent with this [4]. As a whole, even if additional features have appeared at low frequencies, they are either too faint and have no observable effect on the spectrum or themselves have spectral cutoffs.

(2) The method uses the spectral index α ($S \sim \nu^{-\alpha}$) in the optically thin region of the spectrum, but compact sources are often variable and, hence, it is not correct to construct the integrated spectrum using flux densities measured at different epochs. Since 5-GHz Green Bank, Westerbork, MERLIN, and VLBI observations obtained at different epochs are available, proximity of the flux densities for a given source would be good evidence for the absence of appreciable variability on timescales of about ten years. Additional indirect evidence is the "smoothness" of the spectrum presented in [4].

(3) Generally speaking, the magnetic field should be estimated at frequencies where the optical depth is close to unity. In this case, the observed emission is contributed by the entire source. If the optical depth (τ) $\gg 1$ is much greater than unity, we see emission only from a surface layer of gas [31]. Since $\tau \sim 1$ near the spectral peak, we use flux densities measured in this region. As a rule, the measurements of the studies of CSS sources [22–24] covered the region of the spectral peak and were then used to estimate the physical parameters. The spectra for the sample studied are rather sparse, and there are cases when the closest point in the cutoff region is quite far in frequency from the spectral peak. The widest separation is for the GPS source 0538+7131: the peak frequency is 4.2 GHz, whereas the closest point with measurements in the cutoff region is at 1.4 GHz. Since $H_\perp \sim \nu^5$, the difference in the magnetic-field estimates for this source will be a factor of $(4.2/1.4)^5 = 243$ (two orders of magnitude). To compare the results obtained for our GPS sample with those for the sample of CSS sources, we have estimated the physical parameters using the same method as in [22–24]. In addition, we estimated the physical parameters using the same method, but using the peak frequency and flux density. We comment on these estimates in Section 4.

Table 1. Estimated physical conditions in GPS sources

Source	z, type	$\Omega \times 10^{-6}$	L, pc	α	$H_\perp$, G	$E_{H_\perp}$, erg/cm^2	$E_{H_\perp}$, erg	n_e, cm^{-3}	E_e, erg/cm^3	E_e, erg
0544 + 5847	2.86 Q	0.4″	3	1.16	2.3×10^{-5}	2.2×10^{-11}	1.7×10^{46}	1.8×10^{3}	1.5	1.2×10^{57}
0758 + 5929	1.977 Q	0.14	2	0.4	3.4×10^{-4}	4.6×10^{-9}	1.1×10^{48}	1.1×10^{2}	8.3×10^{-2}	2.1×10^{55}
0826 + 7045	2.003 Q	0.12	2	0.2	2.8×10^{-3}	3.1×10^{-7}	6.3×10^{49}	2.5	1.3×10^{-3}	2.7×10^{53}
0830 + 5813	0.093Q	0.42	1	0.51	6.6×10^{-2}	1.7×10^{-4}	5.2×10^{51}	1.2×10^{-1}	4.7×10^{-6}	1.4×10^{50}
1538 + 5920	3.878 Q	0.21	2	0.77	6.0×10^{-3}	1.4×10^{-6}	3.4×10^{50}	5.1	4.0×10^{-4}	9.4×10^{52}
1622 + 6630	0.201Q	0.12	1	0.46	7.2×10^{-4}	2.1×10^{-8}	5.9×10^{47}	2.8×10^{2}	1.2×10^{-1}	3.5×10^{54}
1642 + 6701	2.167 Q	0.72	5	1.01	1.8×10^{-4}	1.2×10^{-9}	3.8×10^{48}	3.8×10^{1}	1.3×10^{-2}	4.1×10^{55}
1746 + 6921	1.886 Q	<0.36	<3	0.41	$<3.9 \times 10^{-3}$	$<6.2 \times 10^{-7}$	$<7.6 \times 10^{50}$	>1.8	$>4.0 \times 10^{-4}$	$>4.3 \times 10^{53}$
1819 + 6707	0.220Q	20.16	14	0.54	7.8×10^{-2}	2.4×10^{-4}	1.8×10^{55}	6.3×10^{-4}	2.2×10^{-8}	1.6×10^{51}
1841 + 6715	0.470Q	0.4	3	0.63	6.5×10^{-3}	1.7×10^{-6}	1.0×10^{51}	2.5	2.5×10^{-4}	1.6×10^{53}
1958 + 6158	1.824 Q	0.32	3	0.23	9.7×10^{-3}	3.8×10^{-6}	3.6×10^{51}	3.2×10^{-1}	7.9×10^{-5}	7.4×10^{52}
0538 + 7131	2	0.12	2	1.4	1.8×10^{-3}	1.3×10^{-7}	2.7×10^{49}	6.3×10^{2}	5.3×10^{-2}	1.1×10^{55}
1525 + 6801	2	0.72	5	1.08	6.6×10^{-3}	1.7×10^{-6}	5.2×10^{51}	3.9	2.0×10^{-4}	6.0×10^{53}
1600 + 7131	2	1.0	6	1.67	2.3×10^{-3}	2.0×10^{-7}	9.8×10^{50}	7.6×10^{1}	5.3×10^{-3}	2.6×10^{55}

3. PHYSICAL CONDITIONS IN THE NUCLEI OF GPS SOURCES

In the final sample, we have kept sources that had "smooth" measured spectra and similar flux densities from VLBI and single-dish observations at 5 GHz. This latter requirement guarantees a negligible contribution from any halo. Sources having nearly flat spectra in the optically thin region of the spectrum were excluded, since small changes of the spectral index can result in a wide scatter in the estimates of the physical conditions. We added to the sample three sources with very "smooth," sharply-peaked spectra (0538 + 7131, 1525 + 6801, and 1600 + 7131).

It is suggested in [13, 17, 33, 34] that synchrotron self-absorption provides the most likely explanation for the spectral cutoffs. We have estimated the physical parameters of 14 GPS sources assuming that the radio emission is due to synchrotron radiation from an electron–positron plasma and that the low-frequency spectral cutoffs are due to synchrotron self-absorption. We adopted $H_0 = 75$ km s^{-1} Mpc^{-1} and $q_0 = 1/2$. The results are listed in Table 1, which presents the source (1) name; (2) redshift z and type (Q: quasar, G: galaxy); (3) angular size ($\Omega = \theta_1 \times \theta_2$, where θ_1 and θ_2 are the VLBI sizes from [4]); (4) estimated mean linear size L; (5) spectral index α in the optically thin region; and (6)–(11) estimated physical parameters in the nuclei (magnetic-field strength, magnetic-field energy density, total magnetic-field energy within the volume L^3, density of relativistic particles, total energy of relativistic particles within the volume L^3). The data for columns 1, 2, 3, and 5 were taken from [4]. The redshifts of the sources 0538+7131, 1525+6801, 1600+7131 are unknown, and we have adopted $z = 2$ (typical of quasars). Note that the redshift is contained in the formula for the physical parameters in the factor $(1 + z)^{-1}$; thus, uncertainty in z has little effect on the final result. We can see from the table that all estimates correspond to the linear scales $L \sim 1$–10 pc.

When finding the total energy of relativistic particles, we took as the integration limits the energies at which the emission of relativistic electrons in our estimated magnetic field peaks at 10 MHz and 100 GHz. In our previous studies of the physical conditions in CSS sources [22–24], we defined the integration limits in the same way.

In [13, 17, 33, 34], it was indirectly shown that synchrotron self-absorption is the most probable mechanism for the spectral cutoff in GPS sources. Nevertheless, we also present estimates assuming that, despite the synchrotron nature of the emission, the spectral cutoffs are due to thermal plasma that is located in the region where the synchrotron emission is generated. In this case, the emission coefficient is determined by the synchrotron mechanism, and the absorption coefficient, by the thermal plasma. In our view, it is appropriate to give estimates of the density of thermal electrons in the objects studied, since a very high density of thermal electrons can be expected in GPS sources [3, 12]. The results are listed in Table 2, which presents the (1) source name, (2) source linear dimensions, (3) peak frequency, and (4) estimated density of thermal electrons. Columns 1 and 3 were taken from the thesis of Snellen [4]. We can see from the table that the estimated values of n_e are at least an order of magnitude higher than the density of thermal electrons in our Galaxy on the same scales [35]. Here, we have assumed a uniform filling of the volume by the thermal electrons. If the volume is

filled by dense clouds, such as those corresponding to the optical narrow-line region (NLR), then, depending on the filling factor, the thermal-electron densities listed in Table 2 should be increased accordingly. For example, if the clouds fill 10% of the volume, all the estimates in Table 2 should be increased by an order of magnitude.

In [36], a source model explaining the spectral cutoff as the effect of thermal absorption is constructed. In particular, a special model was introduced to explain the relationship between the size of the compact source and the peak frequency. According to this model, the thermal electrons in GPS galaxies are distributed as $n_e = n_0(r/R_0)^{-2}$, where $n_0 = 10$ cm^{-3} at a distance $R_0 = 10$ kpc. It is easy to verify that $n_e \sim 10^7$ cm^{-3} on a scale of 1 pc; i.e., three to four orders of magnitude higher than our estimates. Apparently, thermal absorption can account for the spectra of sources in which the absorbing regions are considerably larger than those in the sample studied and, at the same time, in which the densities of thermal electrons are rather high. However, thermal absorption remains improbable as the main mechanism leading to the spectral cutoffs in all compact radio sources.

4. DISCUSSION

The typical angular resolution of the VLBI observations was better than 1 mas; nevertheless, there were virtually no completely resolved sources. The published source angular sizes are several-fold smaller than the angular resolution of the VLBI observations [4]. At the same time, as noted above, the technique used is very sensitive to the angular size of the source: $H \sim \theta^4$. Hence, if the actual angular size is smaller than the originally published value, the magnetic field is overestimated and the relativistic-particle density underestimated. On the other hand, VSOP observations of 3C 147 have shown that the angular size of this source may be considerably larger than indicated by early VLBI observations [37]. If the angular size is underestimated, the magnetic field should be increased and the number density of relativistic particles decreased. Our estimates demonstrate that, if the source angular sizes differ from their true values by no more than a factor of two, the main results remain essentially unchanged.

Of the 14 sources studied, ten have $E_H \ll E_e$, three have $E_H \sim E_e$, and only one has $E_H \gg E_e$. In studies of a sample of CSS, the case where the magnetic-field energy far exceeds the relativistic-particle energy was fairly common. In estimates derived from the peak frequency and flux density, the most typical case is energy equipartition, $E_H \sim E_e$ (nine sources). This wide discrepancy between the physical conditions estimated based on the first point in the spectrum beyond the cutoff and on the spectral peak is due to the strong frequency dependence of the $H_\perp$ estimates ($H_\perp \sim \nu^5$). Apparently, the true physical conditions are intermediate between the estimates obtained using the two methods. This results in additional distortion of the dependences derived; we take this into account in our subsequent conclusions.

Table 2. Estimated density of nonrelativistic electrons at $T = 10^4$ K

Source	L, pc	ν_p, GHz	n_e, cm^{-3}
0544 + 5847	3	1.4	1000
0758 + 5929	2	2.0	1800
0826 + 7045	2	3.5	3100
0830 + 5813	1	1.6	2000
1538 + 5920	2	3.5	3100
1622 + 6630	1	4.0	5100
1642 + 6701	5	1.3	750
1746 + 6921	<3	2.2	>1600
1819 + 6707	14	0.8	250
1841 + 6715	3	2.1	1500
1958 + 6158	3	3.0	2200
0538 + 7131	2	4.2	4200
1525 + 6801	5	1.8	1000
1600 + 7131	6	1.7	900

It is also interesting to compare the mean magnetic fields in quasars and galaxies. We have found that the mean magnetic field in quasars (~10^{-3} G) is weaker than that in galaxies (~10^{-2} G). The typical sizes of compact features in both quasars and galaxies are several parsecs. Of course, the statistical significance of this result is low (the sample contains only four radio galaxies). However, these results are consistent with those on the physical conditions in CSS sources obtained in [24], where the mean fields in quasars and galaxies were 10^{-4} and 10^{-3} G, respectively, with feature sizes of a few hundred parsecs. For the physical conditions estimated from the peak frequency and flux density, the typical field is somewhat stronger, but the dependence is the same. Earlier, in [23, 24], we found a correlation between the sizes of the compact self-absorbing features in CSS sources and the magnetic field: the smaller the self-absorbing feature, the weaker the magnetic field and the higher the number density of relativistic particles. According to the results for GPS sources, the mean fields in features with sizes of several parsecs are stronger than those in features in CSS sources. Thus, there is an obvious inconsistency between these two sets of estimates obtained using the same method.

Figures 1 and 2 are reproduced from [24]. Uncertain estimates of the magnetic field are labeled "?." We can see that the early result was basically due to several points with anomalously low magnetic fields $H \sim 10^{-7}$–10^{-10} G.

There are a number of possible explanations for this result, which contradicts our previous work.

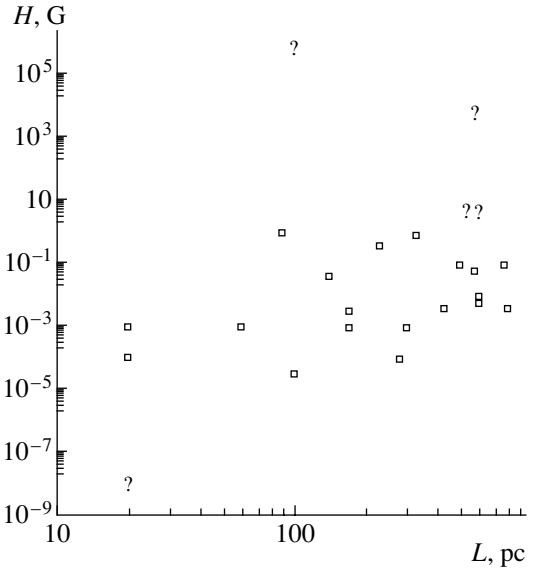

Fig. 1. Magnetic-field strength H as a function of linear size of the source L for galaxies [24]. The "?" denotes uncertain estimates.

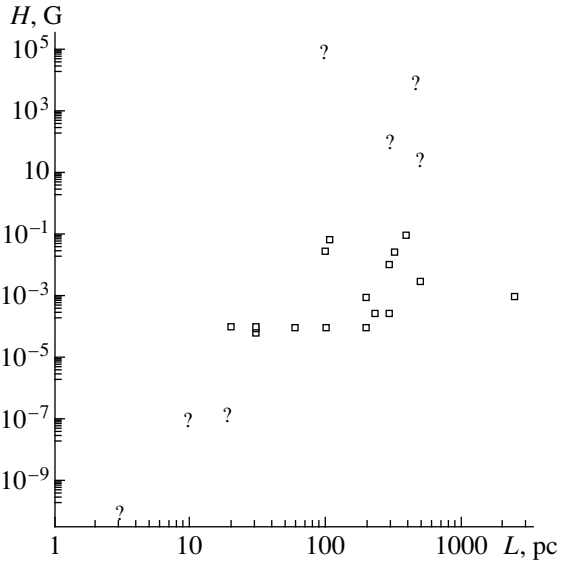

Fig. 2. Same as Fig. 1 for quasars [24].

(1) Let us suppose there is superluminal expansion in the sources with anomalously low magnetic fields. Then, due to Doppler brightening, the observed flux exceeds the actual value. Since $H \sim S^{-2}$, this results in underestimation of the magnetic field (this explanation was proposed by Artyukh [38]).

(2) Let us suppose that the angular sizes of sources with weak magnetic fields have been strongly underestimated (as is possible, according to [37]). A tenfold underestimation of the angular size will lead to underestimation of the magnetic field by four orders of magnitude.

(3) We also may suppose that the CSS and GPS sources are not related from the viewpoint of their evolution. In this case, there should not be any relation between the physical conditions in these two classes of sources. However, the evolutionary relationship between these classes seems beyond question, so that we consider this explanation to be improbable.

(4) It is also possible that we, indeed, observe a thermal cutoff in sources with anomalously low magnetic fields, rather than a synchrotron cutoff. At the same time, the cutoffs in the spectra of the remaining sources are due to synchrotron self-absorption.

Thus, there are a number of explanations that could invalidate the dependence published earlier. However, investigating these possible explanations is far beyond the scope of this work. As was already noted in [23, 24], the increase of the magnetic field with the size of the compact feature seemed to us unexpected and not obvious from a physical standpoint. We believed it to be more natural that the density of the relativistic particles and magnetic-field strength should be higher the smaller the compact, self-absorbing feature.

If GPS sources and CSS sources are the same type of object at different stages of evolution, we can see a statistical correlation linking the magnetic fields in compact feature to their size. This dependence is as follows: as the sizes of the compact, self-absorbing features decrease by two orders of magnitude (from hundreds of parsec in CSS sources to several parsecs in GPS sources), the fields increase by an order of magnitude: $H \sim 1\sqrt{L}$ ($H \sim L^{-1}$ for estimates derived from the spectral peak). Thus, instead of a dependence relating the size of the compact feature with the peak frequency, we have obtained a dependence linking this size with the field strength in the feature. This correlation seems to us more physically grounded.

5. CONCLUSIONS

Our study of a sample of "weak" GPS sources has yielded the following results:

(a) on small scales, of the order of several parsecs, the magnetic-field energy is, as a rule, considerably lower than the relativistic-particle energy;

(b) the average magnetic field in quasars (10^{-3} G) is an order of magnitude weaker than that in galaxies (10^{-2} G);

(c) the magnetic-field strength may be related to the size of the self-absorbing compact feature as $H \sim L^{-0.5(-1)}$.

ACKNOWLEDGMENTS

The author is grateful to I.A.G. Snellen for providing data on some of the sources studied, V.S. Artyukh for discussion of the technique for inferring the physical conditions from the spectral cutoff, V.I. Shishov for interesting comments on the work, and G.É. Tyul'basheva for help with the preparation of the paper.

REFERENCES

1. Gopal-Krishna, A. R. Patnaik, and H. Steppe, Astron. Astrophys. **123**, 107 (1983).
2. R. L. Mutel and R. B. Phillips, in *The Impact of VLBI on Astrophysics and Geophysics (IAU Symposium 129)*, Ed. by M. J. Reid and J. M. Moran (Kluwer, Dordrecht, 1988), p. 73.
3. C. Stanghellini, C. P. O'Dea, S. A. Baum, and E. Laurikainen, Astrophys. J., Suppl. Ser. **88**, 1 (1993).
4. I. A. G. Snellen, Ph.D. Thesis (Netherlands, 1997).
5. C. Stanghellini, C. P. O'Dea, S. A. Baum, *et al.*, Astron. Astrophys. **325**, 943 (1997).
6. J. C. Carvalho, Astron. Astrophys. **329**, 845 (1998).
7. R. B. Phillips and R. L. Mutel, Astrophys. J. **236**, 89 (1980).
8. R. B. Phillips and R. L. Mutel, Astron. Astrophys. **106**, 21 (1982).
9. J. C. Carvalho, Mon. Not. R. Astron. Soc. **215**, 463 (1985).
10. C. Fanti, R. Fanti, D. Dallacasa, *et al.*, Astron. Astrophys. **302**, 317 (1995).
11. C. P. O'Dea, S. A. Baum, and G. B. Morris, Astron. Astrophys., Suppl. Ser. **82**, 261 (1990).
12. C. P. O'Dea, S. A. Baum, C. Stanghellini, *et al.*, Astron. Astrophys., Suppl. Ser. **84**, 549 (1990).
13. C. P. O'Dea, S. A. Baum, and C. Stanghellini, Astrophys. J. **380**, 66 (1991).
14. W. van Breugel, G. Miley, and T. Heckman, Astron. J. **89**, 5 (1984).
15. J. C. Carvalho, Astron. Astrophys. **292**, 392 (1994).
16. C. Stanghellini, S. A. Baum, C. P. O'Dea, and G. B. Morris, Astron. Astrophys. **233**, 379 (1990).
17. S. A. Baum, C. P. O'Dea, D. W. Murphy, and A. G. de Bruyn, Astron. Astrophys. **232**, 19 (1990).
18. C. P. O'Dea, C. Stanghellini, S. A. Baum, and S. Charlot, Astrophys. J. **470**, 806 (1996).
19. C. P. O'Dea and S. A. Baum, Astron. J. **113**, 148 (1997).
20. A. C. S. Readhead, G. B. Taylor, W. Xu, and T. J. Pearson, Astrophys. J. **460**, 612 (1996).
21. A. C. S. Readhead, G. B. Taylor, T. J. Pearson, and P. N. Wilkinson, Astrophys. J. **460**, 634 (1996).
22. V. S. Artyukh, S. A. Tyul'bashev, and P. A. Chernikov, Astron. Zh. **76**, 3 (1999) [Astron. Rep. **43**, 1 (1999)].
23. S. A. Tyul'bashev and P. A. Chernikov, Astron. Zh. **77**, 331 (2000) [Astron. Rep. **44**, 286 (2000)].
24. S. A. Tyul'bashev and P. A. Chernikov, in Astron. Astrophys. 2001 (in press).
25. R. B. Rengelink, Y. Tang, A. G. de Bruyn, *et al.*, Astron. Astrophys. **124**, 259 (1997).
26. P. C. Gregory and J. J. Condon, Astrophys. J., Suppl. Ser. **75**, 1011 (1991).
27. P. C. Gregory, W. K. Scott, K. Douglas, and J. J. Condon, Astrophys. J., Suppl. Ser. **103**, 427 (1996).
28. I. A. G. Snellen, R. T. Schilizzi, A. G. de Bruyn, *et al.*, Astron. Astrophys., Suppl. Ser. **131**, 435 (1998).
29. I. A. G. Snellen, R. T. Schilizzi, M. N. Bremer, *et al.*, Mon. Not. R. Astron. Soc. **301**, 985 (1998).
30. I. A. G. Snellen, R. T. Schilizzi, M. N. Bremer, *et al.*, Mon. Not. R. Astron. Soc. **307**, 149 (1999).
31. V. S. Artyukh, Tr. Fiz. Inst. Akad. Nauk SSSR **189**, 223 (1988).
32. V. I. Slish, Nature **199**, 682 (1963).
33. M. W. Hodges, R. L. Mutel, and R. B. Phillips, Astron. J. **89**, 1327 (1984).
34. R. L. Mutel, M. W. Hodges, and R. B. Phillips, Astrophys. J. **290**, 86 (1985).
35. D. Downes and A. Maxwell, Astrophys. J. **146**, 653 (1966).
36. G. V. Bicknell, M. A. Dopita, and C. P. O'Dea, Astrophys. J. **485**, 112 (1997).
37. V. I. Slysh, private communication.
38. V. S. Artyukh, private communication.
39. P. N. Wilkinson, A. C. S. Readhead, B. Anderson, and G. N. Purcell, Astrophys. J. **232**, 365 (1979).

Translated by G. Rudnitskiĭ

Astronomy Reports, Vol. 45, No. 6, 2001, pp. 434–441. Translated from Astronomicheskiĭ Zhurnal, Vol. 78, No. 6, 2001, pp. 505–513.

Mathematical Modeling of the Structure of an Accretion Disk in a Stellar Binary System

M. V. Abakumov[2], S. I. Mukhin[2], Yu. P. Popov[1], and V. M. Chechetkin[1]

[1]*Keldysh Institute of Applied Mathematics, Moscow, Russia*

[2]*Moscow State University, Vorob'evy gory, Moscow, Russia*

Received September 22, 2000

Abstract—Numerical simulations of gas-dynamical processes taking place in the accretion disk of a stellar binary system are presented. The initial state of the disk is an equilibrium gaseous configuration. Mechanisms for the development of spiral waves and associated variations in the angular momentum of the gas are considered. The influence of the ratio of the binary-component masses and the initial disk configuration are investigated. It is concluded that the existence of a steady-state disk is impossible without a flow of gas from the donor star. © *2001 MAIK "Nauka/Interperiodica".*

1. INTRODUCTION

Investigation of gas-dynamical flows in accretion disks in stellar binary systems are currently a topical problem in astrophysics. Accretion disks are associated with objects such as black holes, neutron stars, white dwarfs, etc. Thus, information about the properties of these objects can be obtained by studying the processes occurring in accretion disks. One of the main factors in the evolution of accretion disks is the loss of angular momentum due to various physical effects. It is precisely angular-momentum loss that determines the character of the disk radiation, which is especially important for observations.

Accretion disks are an important element of binary stars, which in turn make up an appreciable fraction of all known stellar systems. Theoretical studies of the formation, evolution, and structure of accretion disks often employ mathematical modeling based on various physical models and computational algorithms. For example, [1–3] are concerned with the formation of disk structure as the result of tidal interactions of spiral shocks, which, in the opinion of those authors, are an important mechanism for angular-momentum loss. The formation of an accretion disk and its structure in a binary as a consequence of a flow of matter from the donor star filling its Roche lobe are considered in [4–6]. In these computations, carried out in two- and three-dimensional approximations, the computational domain contains both components of the binary. Therefore, there are a comparatively small number of computational cells for the difference grid in the vicinity of the accretor, where the disk forms, making it difficult to resolve features in the spatial structure of the disk flow in detail.

Here, we present the results of computations carried out in a two-dimensional approximation in which, analogous to [3], the accretion disk is treated as an independent element of the system. In this case, precision modeling of spatial structures in the disk is possible, with the formation and evolution of these structures occurring under the action of the gravitational forces of both components and the rotation of the binary system as a whole. Special attention is paid to the initial state of the disk, which is specified to be in equilibrium in the absence of the secondary component. In this way, the gas-dynamical flow developing in the disk results exclusively due to the interaction with the secondary.

The ratio of the component masses and the form of the boundary conditions are the parameters of the problem which are varied in the computations. To provide the best reliability in the results and, in particular, monitor the numerical viscosity, we carried out the computations using two different numerical methods: a modification of the scheme of Roe [7] and the method of large particles [8].

The results are intended to answer the question of whether a steady-state gaseous disk can exist in a binary system under the conditions indicated and provide information about the disk's spatial structure, mechanisms for angular-momentum loss by the disk material, etc.

2. MATHEMATICAL MODEL

We consider a system consisting of two stars with masses M and m rotating about the center of mass of the system with constant angular velocity ω. We will take the star with mass M to be the primary and the star with mass m to be the secondary (donor) (Fig. 1).

In accordance with Kepler's third law, the distance A between the components is related to the angular velocity of rotation of the system by the expression

$$\omega^2 A^3 = G(M + m), \quad (1)$$

1063-7729/01/4506-0434$21.00

where G is the gravitational constant. The distance L between the primary and the center of mass of the system has the form

$$L = Am/(M+m). \quad (2)$$

We introduce a noninertial polar coordinate system (r, φ) rotating with angular velocity ω, with its origin coincident with the center of the primary and the $\varphi = 0$ axis passing through the secondary (Fig. 1). We will take the region $\Omega = (r_1 \le r \le r_2)\ (0 \le \varphi \le 2\pi)$—a ring with its center at the coordinate origin—to represent the steady-state (in the absence of the secondary) gaseous configuration of the accretion disk, in which the gas rotates about the primary. We do not take into account the self-gravitation of the gas, since we assume that the mass of gas in the disk is much less than the mass of the primary. The gas is taken to be compressible and ideal, with its behavior described by the system of two-dimensional gas-dynamical equations in Euler variables [9]

$$\begin{aligned}
&\frac{\partial(r\rho)}{\partial t} + \frac{\partial(r\rho u)}{\partial r} + \frac{1}{r}\frac{\partial(r\rho v)}{\partial \varphi} = 0,\\
&\frac{\partial(r\rho u)}{\partial t} + \frac{\partial(r\rho u^2 + rp)}{\partial r} + \frac{1}{r}\frac{\partial(r\rho uv)}{\partial \varphi}\\
&\quad = p + \rho v^2 + r\rho \mathbf{F}_r,\\
&\frac{\partial(r\rho v)}{\partial t} + \frac{\partial(r\rho uv)}{\partial r} + \frac{1}{r}\frac{\partial(r\rho v^2 + rp)}{\partial \varphi}\\
&\quad = -\rho uv + r\rho \mathbf{F}_\varphi,\\
&\frac{\partial(r\rho e)}{\partial t} + \frac{\partial(r\rho uh)}{\partial r} + \frac{1}{r}\frac{\partial(r\rho vh)}{\partial \varphi} = r\rho(\mathbf{F}, \mathbf{v}),\\
&e = \varepsilon + u^2/2 + v^2/2, \quad h = e + p/\rho
\end{aligned} \quad (3)$$

with the equation of state

$$p = (\gamma - 1)\rho\varepsilon. \quad (4)$$

Here, r is the radius; φ, the polar angle; t, time, ρ, the gas density; p, the pressure; ε, the specific internal energy; e, the total specific energy; γ, the adiabatic index; h, the total specific enthalpy; $\mathbf{v} = (u, v)^T$, the gas velocity; u, its radial component; v, its azimuthal component; $\mathbf{F}$, the total specific internal force acting on a gas particle; and $\mathbf{F}_r$ and $\mathbf{F}_\varphi$, its radial and azimuthal components (in dimensionless variables), respectively:

$$\begin{aligned}
\mathbf{F}_r &= -\frac{1}{r^2} + \frac{m}{d^2}\cos(\alpha + \varphi) - \omega^2 s\cos(\eta + \varphi) + 2\omega v,\\
\mathbf{F}_\varphi &= -\frac{m}{d^2}\sin(\alpha + \varphi) + \omega^2 s\sin(\eta + \varphi) - 2\omega u,
\end{aligned} \quad (5)$$

where

$$\begin{aligned}
&d = \sqrt{r^2 + A^2 - 2Ar\cos\varphi},\\
&\sin\alpha = r\sin\varphi/d, \quad \cos\alpha = (A - r\cos\varphi)/d,\\
&s = \sqrt{r^2 + L^2 - 2rL\cos\varphi},\\
&\sin\eta = r\sin\varphi/s, \quad \cos\eta = (L - r\cos\varphi)/s.
\end{aligned}$$

These expressions take into account the gravitational forces of the primary and secondary components, the centrifugal force, and the Coriolis force. Note that the expressions for the forces in the chosen coordinate system do not depend on the solution—i.e., on time—with the exclusion of the last term (containing the velocity), associated with the Coriolis force.

We specified a steady-state gaseous configuration as the initial data in the computations. This enabled us to exclude the influence of gas-dynamical processes associated with a non-equilibrium initial state of the disk. In [10], we investigated in detail the possible equilibrium, cylindrically symmetrical configurations for gas rotating near a gravitating center whose pressure and density are related by the polytropic equation

$$p = k\rho^\gamma, \quad k, \gamma = \text{const}.$$

In particular, we considered the class of equilibrium gas configurations with boundaries of the form

$$Z(r) = \pm\alpha r\exp(-\beta(r - r_0)^2), \quad \alpha, \beta, r_0 > 0, \quad (6)$$

and presented formulas for the equilibrium distribution functions of the velocity $v_\varphi(r, z)$ and density $\rho(r, z)$ of the gas. Using analytical and numerical studies, we showed that the given gaseous configuration could be considered to be in equilibrium and could be used as initial data when modeling processes in an accretion disk in both three-dimensional and two-dimensional approximations.

The computations described below were carried out using dimensional variables based on the following scaling factors:

$$M = 1\times10^{33}\ \text{g}, \quad R = 7\times10^{8}\ \text{cm},$$
$$G = 6.67\times10^{-8}\ \text{cm}^3\ \text{g}^{-1}\ \text{s}^{-2}.$$

We took the distance between the binary components to be $A = 4$, and the mass of the secondary in the

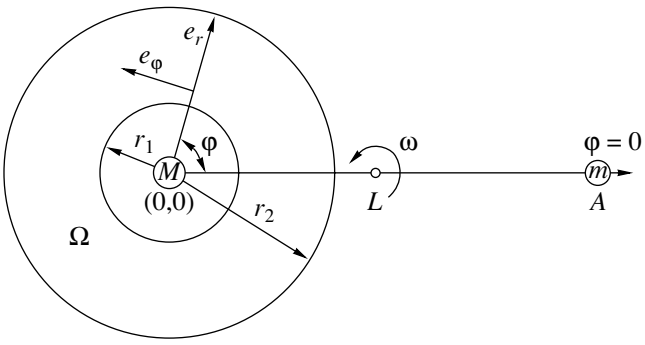

Fig. 1. Diagram of a stellar binary system with the mass of the primary component M, the mass of the secondary component m, and the angular velocity of rotation ω.

main run of the computations was $m = 1$. A complete orbit of the binary system takes place over $T_s \approx 35$. We take the gas to be ideal with equation of state (4) and adiabatic index $\gamma = 5/3$.

The parameters in (6) specifying the initial equilibrium configuration of the disk were taken to be $\alpha = 0.2$, $\beta = 9$, and $r_0 = 0.8$. In this case, most of the gas is concentrated in the ring $0.5 < r < 1.1$, the density distribution has a clear maximum, the total mass of the disk is $M_{\text{gas}} \approx 0.1$, and a complete orbit of a gas particle in the equilibrium configuration takes place over times $T_1 \approx 0.6$ and $T_2 \approx 10$ at the inner and outer edge of the disk, respectively.

Depending on the computation run, the parameters of the computation domain were chosen to be $r_1 = 0.2$, $r_2 = 1.4$; $r_1 = 0.2$, $r_2 = 2.1$; and $r_1 = 0.1$, $r_2 = 3$. The dimensions of the difference grid were 80×80, 120×100, and 160×120, respectively. At the edges of the computation domain, we specified either "free" boundary conditions

$$\frac{\partial \rho}{\partial r} = 0, \quad \frac{\partial u}{\partial r} = 0, \quad \frac{\partial v}{\partial r} = 0, \quad \frac{\partial e}{\partial r} = 0, \qquad (7)$$

or the condition that the gas not flow through the boundary

$$u = 0. \qquad (8)$$

In addition, we varied the component mass ratio and the initial configuration of the disk in the computations.

3. RESULTS OF NUMERICAL COMPUTATIONS

The aim of our mathematical modeling was investigating the flow of gas in an accretion disk near the primary under the influence of the gravitation of the secondary and rotation of the binary system. We present the results of computations performed with various parameters for the system and various boundary and initial conditions. To increase the trustworthiness of the results, we carried out computations using two different numerical methods: a modification of the scheme of Roe [7] and the method of large particles [8]. The results of these two computations were essentially identical, testifying to the insignificant influence of the approximation viscosity.

The results of all our computations display the general characteristic stage of the development of an accretion disk. Let us examine the results using a typical computation run with the mass ratio equal to unity and the free boundary conditions (7) as an example.

We carried out the solution in several steps. As indicated above, the initial disk configuration is equilibrium. We obtained a preliminary solution of the system of equations (3) and (4) in the absence of a secondary ($m = 0$). These computations showed that, in this case, the initial state of the gas remains virtually unchanged, which not only confirms that it is stationary but also testifies to its stability.

The main computation was then carried out including the secondary component of the binary, which was located at an appreciable distance from the primary ($10^3 A$) at the initial time. Then, in order to avoid abrupt relaxation processes, we gradually moved the secondary linearly to a distance A from the primary over a time $T_A = 4.5$. The angular velocity of rotation of the system, the position of its center of mass, and the total specific external force varied in accordance with relations (1), (2), and (5), respectively. At this stage, also, the initial state of the gas in the disk varied only weakly. The reason for this is that, in this formulation, variations of the gas velocity and, as a consequence, variations of the remaining parameters describing its state are determined by the action of the external force field **F** and also by the force of the gas-kinetic pressure; therefore, these variations have an inertial character and are manifest with some delay.

The pattern of the force field is such that, in this stage of the computation, the gas gradually acquires a positive radial velocity component, leading to the formation of a shock propagating at the periphery of the computation domain. Note that the radial and angular components of the "perturbing" total force are nonuniform in the polar angle. As a result, the shock front acquires an elliptical shape.

In its passage through the shock front, the gas essentially loses its radial velocity component. This leads to the formation of a central core, inside of which a spiral formation develops. The shock propagates to the outer boundary of the domain and, because of our use of the boundary conditions (7), freely leaves it.

In this way, there is a disruption of the initial equilibrium gas configuration and a new state develops, an important element of which is the spiral structure (Fig. 2). Figure 2 presents contours of the density and the velocity field in the ringlike computation domain at time $t = 18.0$. This configuration does not change qualitatively over a time of the order of $T_s \approx 35$ and is quasi-steady-state in the sense that the gas velocity's radial component is much less than its azimuthal component.

To study the two-armed disk structure that had formed, we also computed the trajectories of gas particles in the disk. These computations showed that, as a rule, passage of a particle through the spiral-wave front leads to changes in its angular momentum.

Figure 2 presents the trajectory of a gas particle (thick solid curve) located at the point ($r_a = 0.75$, $\varphi = 0$) at time $t = 14$ and passing through nearly one and a half orbits around the primary by the time $t = 21$. In this time interval $14 \le t \le 21$, the structure of the flow in the disk remains virtually unchanged. Therefore, we superpose the particle trajectory on the density contours at the intermediate time $t = 18$. Figure 3 depicts the time variations of the sine of the particle's polar angle $\sin\varphi$, its

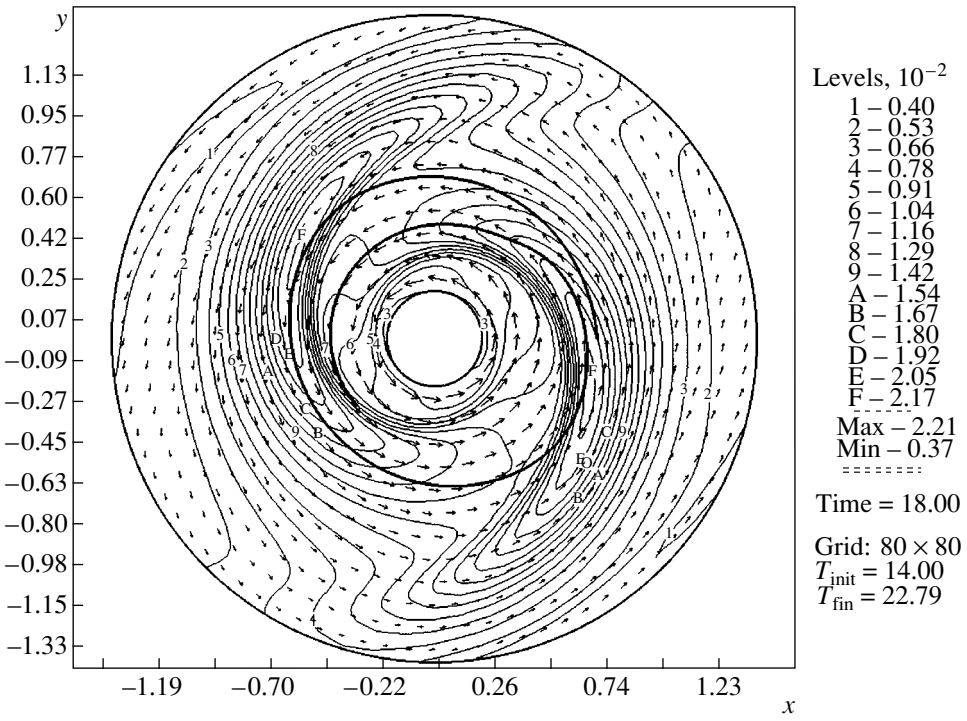

Fig. 2. Density contours (solid) and the velocity field (vectors) at time $t = 18$. The thick curve shows the trajectory of a gas particle with the initial position (at $t = 14$) at the point ($r_a = 0.75$, $\varphi = 0$).

radius R, and its angular momentum $J = rv_\varphi$. A comparison of these plots clearly demonstrates that a particle's angular momentum decreases when it passes through the spiral-wave front. The computations show that the degree to which the angular momentum decreases depends appreciably on the angle at which the particle intersects the front, the intensity of the wave, and the shape of the front.

It is important to note that the angular momentum can also change appreciably when the particle moves behind the spiral-wave fronts. For example, Fig. 4 presents the trajectory of a particle located at the same initial time at the position (r_b, $\varphi = 0$), where $r_b > r_a = 0.75$. The angular momentum of this particle sharply decreases when its passes through the region of the negative pressure gradient behind the wave front. We can see in Fig. 5 that, in the course of its motion, this particle (whose initial position is still further from the center) can acquire an additional angular momentum, causing it to be shifted toward the outer edge of the disk and eventually leave the computation domain. This occurs in spite of the fact that the trajectory of this particle shifts toward the center relative to its initial position during a certain time interval. It follows from the previous results that the accretion of matter depends not only on the presence of a spiral wave but also on the overall superposition of forces, including the pressure gradient.

During the quasi-steady-state phase, we see only slight qualitative variations in the disk structure. These include a decrease in the wave intensity and "winding up" of the gas in the fronts in the direction of rotation of the particles. The density and pressure maxima of the gas gradually shift toward the center of the region, as a consequence of the loss of angular momentum by some fraction of the gas.

These stages of the formation of a spiral flow are characteristic to some degree of all the computations

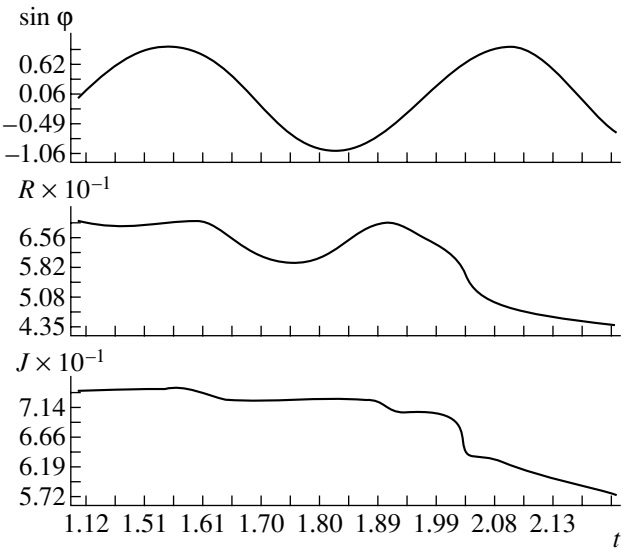

Fig. 3. Time variation of the sine of a particle's polar angle $\sin\varphi$ (the rotation phase), its radius R, and its angular momentum $J = rv_\varphi$.

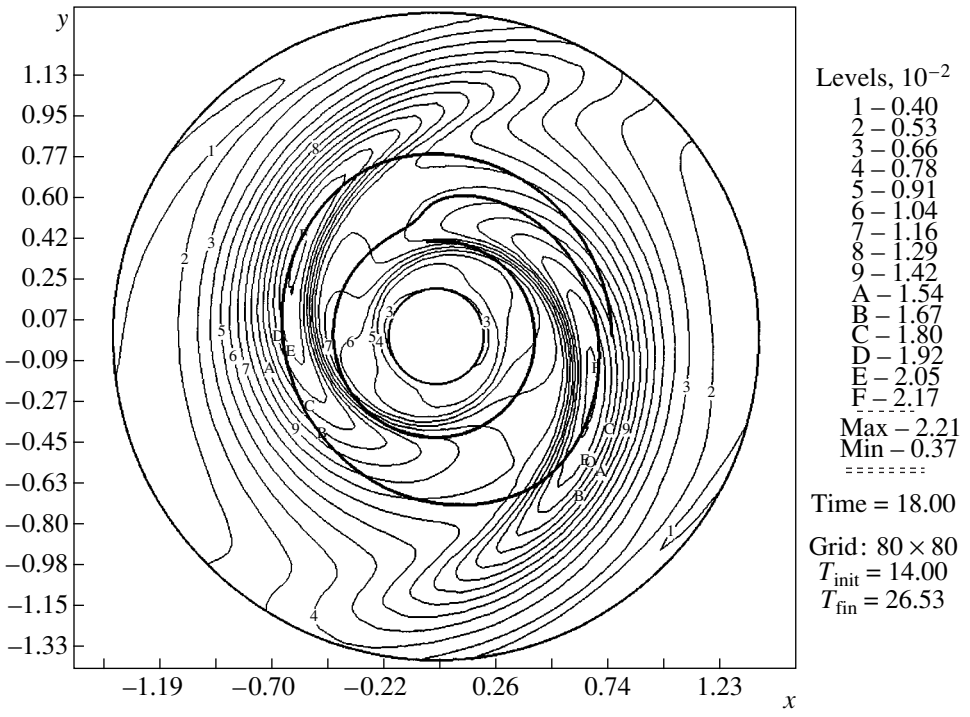

Fig. 4. Same as Fig. 2 for the initial position of the test particle ($r_b > r_a$, φ = 0).

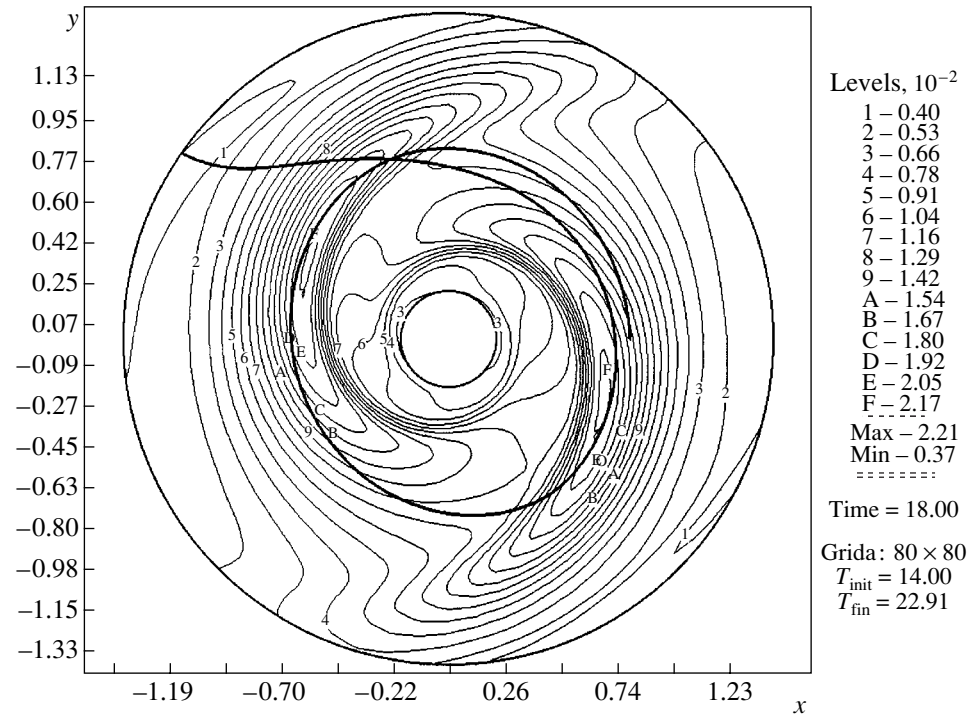

Fig. 5. Same as Fig. 2 for the initial position of the test particle ($r_c > r_b$, φ = 0).

we considered. We now turn to a description of the properties of several computation runs corresponding to various values of the main dimensionless parameters of the problem.

First and foremost, we consider the influence of the component mass ratio on processes in the disk. With this aim, we carried out computations with different ratios of the primary and secondary masses. As the

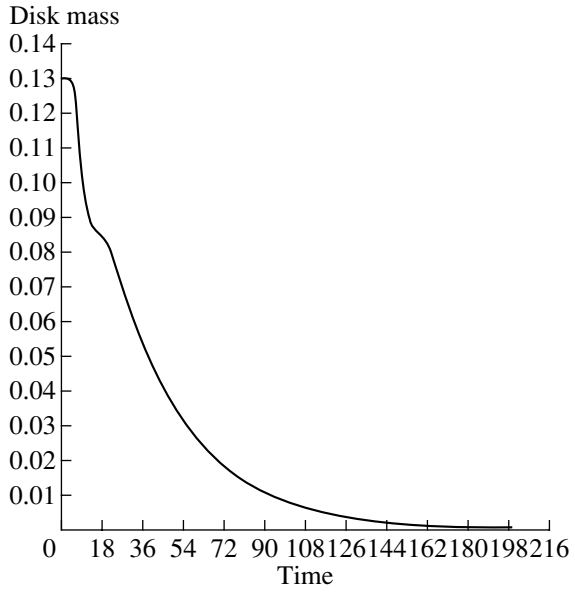

Fig. 6. Time dependence of the mass of the accretion-disk material.

mass of the secondary is increased, we observed an increase in the intensity of the spiral waves and also variation of the shape of the wave fronts. The results for the case of decreased secondary mass, for example $m = 0.1$ (with a constant distance between the components $A = 4$), proved interesting. The two-armed spiral structure is established appreciably later than in the runs described above—after a time interval of the order of $2T_s$. In addition, the intensity of the spiral waves that are formed is considerably less.

To estimate the influence of the form of the initial equilibrium configuration, we carried out computations in which the mass of the secondary was, as before, $m = 1$, but the parameters in boundary Eq. (6) were specified to be $\alpha = 0.19$, $\beta = 1$, and $r_0 = 0.2$. In this case, the mass of the initial configuration is, as before, $M_{gas} \approx 0.1$, but the pressure and density monotonically decrease from the inner to the outer boundary of the domain. In this run also, a radial shock wave formed, though it has a smaller intensity than in the main run. The spiral waves form at later times, their intensities are small, and the shape of the wave fronts differs from those described above. We obtained similar results when we chose for the initial configuration a two-dimensional equilibrium configuration (in the absence of the secondary) with a Keplerian velocity distribution in the radius.

One of the main questions that should be addressed by our computations is whether there can be a steady-state accretion disk in a stellar binary system. The results described above lead us to conclude that, in the adopted formulation of the problem, strictly speaking, there is no steady-state disk. After some time interval whose duration depends on the parameters adopted, we observe a quasi-steady state characterized by the presence of spiral formations. Further, the distributions of the density, pressure, and so forth, decrease in magnitude while maintaining their overall profiles. The main

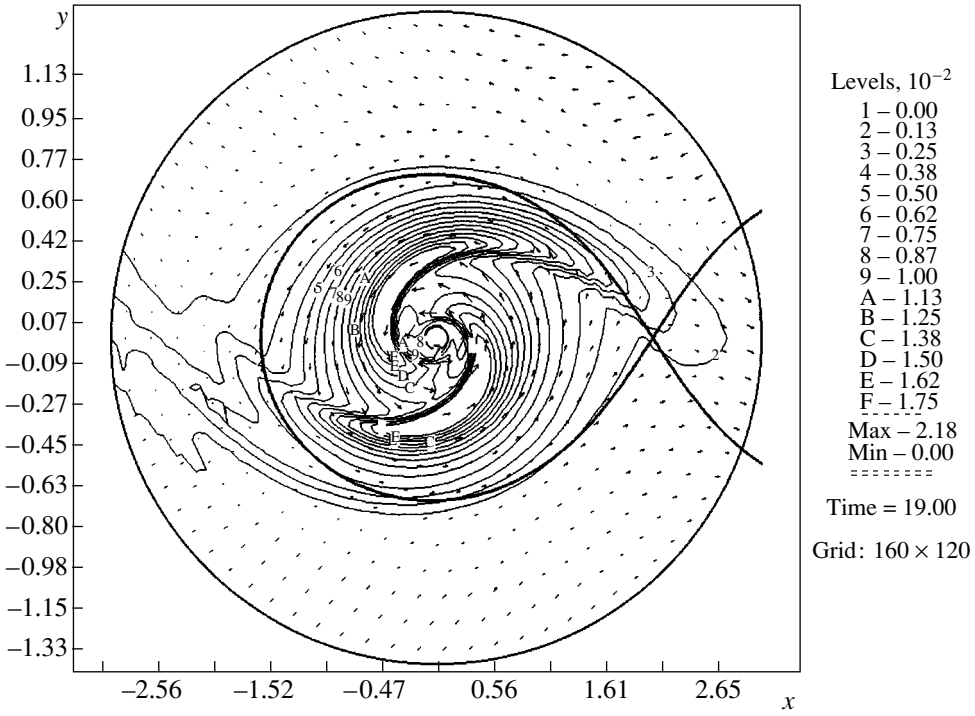

Fig. 7. (Solid) density contours and (vectors) the velocity field at time $t = 19$ for a computation domain containing the Roche lobe of the primary (thick curve) and the Lagrange point L_1.

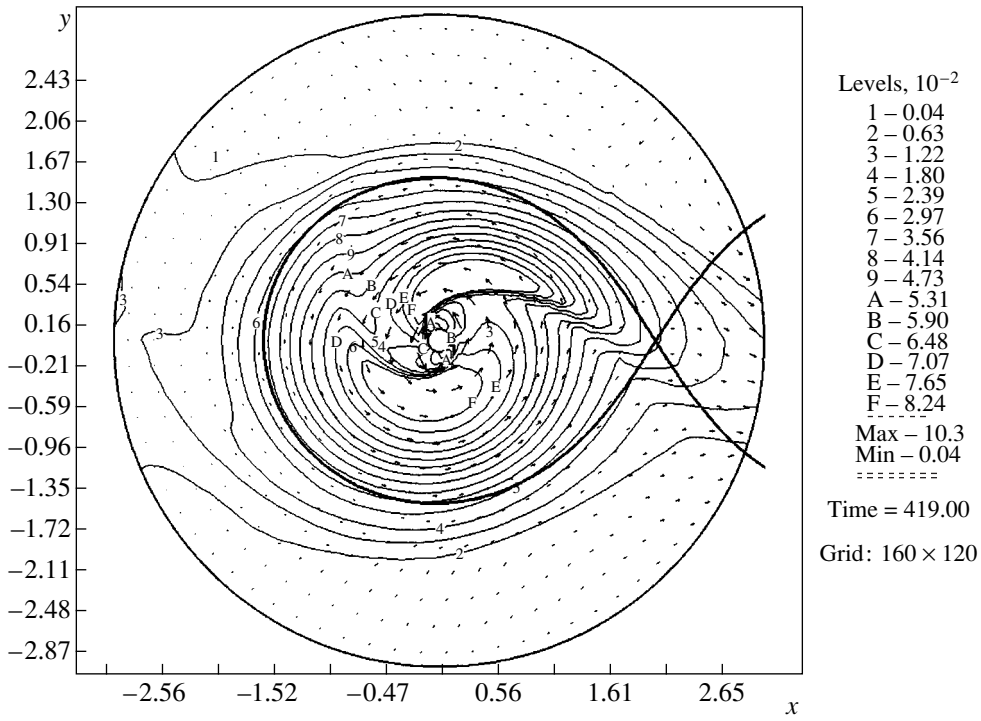

Fig. 8. Same as Fig. 7 for time $t = 419$.

reason for this is the flow of mass out through the boundaries of the domain (primarily the outer boundary), due to the boundary conditions (7) imposed. This is demonstrated by Fig. 6, which presents the time dependence of the mass in the ring computation domain.

We repeated this computation run on an appreciably larger computational domain ($r_1 = 0.1$, $r_2 = 3$) that contained the Roche lobe of the primary and the Lagrange point L_1. Here, as in the run described above, a two-armed spiral disk structure is established (Fig. 7). This structure remains qualitatively the same over a longer time of the order of $12T_s$. However, as before, this structure is not steady-state, since we observe a flow of disk material both toward the inner boundary of the computation domain (toward the primary) and toward the outer boundary, primarily through the vicinity of the inner Lagrange point. The intensity of the spiral waves varies with time, together with the shape of the wave fronts (Fig. 8). The structure of the spiral-wave structure on the far side relative to the secondary is especially evident.

It is clear that a steady state of the spiral structure that forms is impossible in the presence of an uncompensated flow of matter from the primary. In our formulation of the problem, we can formally avoid the outflow of mass by replacing the boundary conditions (7) with the nonflow boundary conditions (8). In this case, it is indeed possible to obtain a steady-state spiral disk structure in an expanded region containing the Roche lobe of the primary with the parameters $r_1 = 0.2$ and $r_2 = 2.1$ (Fig. 9). The computations showed that this structure is steady-state and does not vary over an extended time of the order of $20T_s$.

Another important question is the nature of the spiral waves that arise. Traditionally, it is usually thought that they represent standing shock waves with a spiral discontinuity front [3]. We were not able to confirm this hypothesis through our numerous computations. First and foremost, in the specified gaseous configuration (shown to be possible by our computations), the steady-state nature of the shock waves comes into contradiction with the requirement that the entropy be constant in a closed system, since particles in a steady-state flow that intersect a surface discontinuity many times will gradually increase the entropy. On the other hand, a careful study shows that, in the quasi-steady-state regimes of disk evolution described above, the velocity components of the particles do not experience discontinuities when they intersect the supposed shock fronts and the Mach number is appreciably higher than unity in virtually the entire region (with the exception of peripheral areas, where the density is vanishingly small).

A special analytical and numerical study of steady-state gas flows in a gravitational field in a one-dimensional approximation was devoted to questions concerning the nature of steady-state spiral waves [11]. It was demonstrated that, in the presence of external forces, there exist two classes of continuous steady-state solutions, corresponding to compression and rarefaction waves.

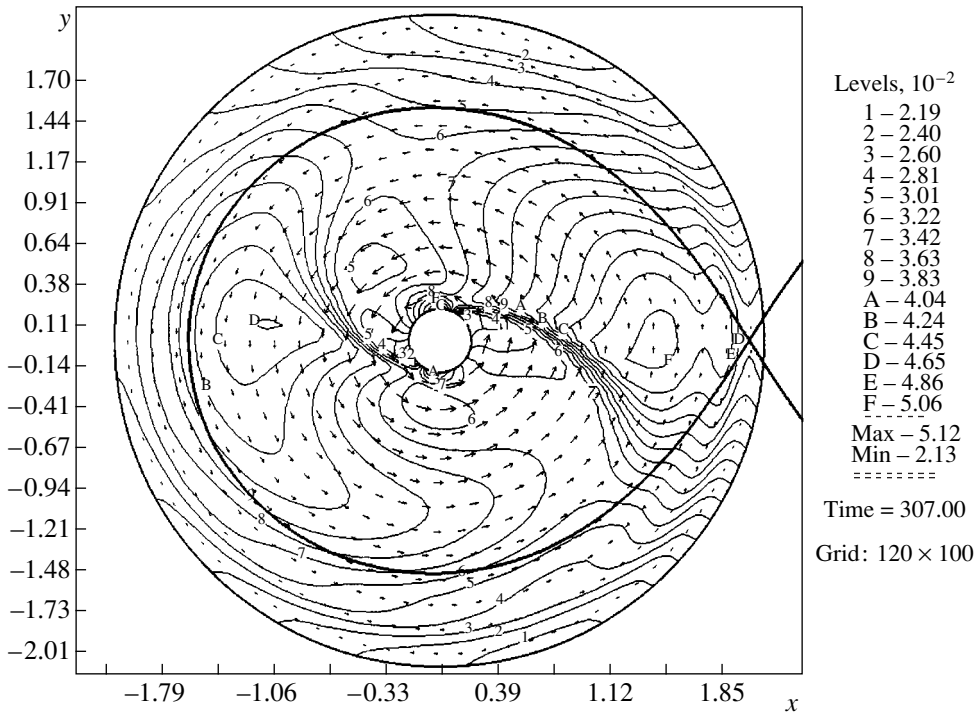

Fig. 9. Same as Fig. 7 for other boundary conditions (see text) and time $t = 307$.

4. CONCLUSIONS

Analysis of the results of our computations has shown that the gas-dynamical processes in the accretion disk of a stellar binary system are determined by a complex force field—the gravitational interactions of both stellar components, the centrifugal force, and the Coriolis force—as well as by the gas-dynamical pressure gradient. The gravitational and centrifugal forces are time independent. Under the action of these forces, a flow containing two spiral formations with enhanced density and pressure forms in the disk.

In our formulation of the problem with free boundary conditions, there is no steady-state disk. The reason is the flow of gas through the boundaries of the computation domain, primarily the outer boundary. Realization of a steady-state disk requires a flow of mass from the donor star, as is taken into account in a full treatment of the problem [5, 6, 12]. Our computations, estimates, and analytical study indicate that the spiral structures that form in the disk are not shock waves, as is usually assumed [11].

ACKNOWLEDGMENTS

This work was supported by the Russian Foundation for Basic Research (project no. 00-01-00392).

REFERENCES

1. K. Sawada, N. Sekino, and E. Shima, KEK Progress Rep. **89**, 197 (1990).
2. D. Molteni, G. Belvedere, and G. Lanzfame, Mon. Not. R. Astron. Soc. **249**, 748 (1991).
3. T. Matsuda, N. Sekino, E. Shima, *et al.*, Astron. Astrophys. **235**, 211 (1990).
4. D. V. Bisikalo, A. A. Boyarchuk, O. A. Kuznetsov, *et al.*, Astron. Zh. **72**, 190 (1995) [Astron. Rep. **39**, 167 (1995)].
5. D. V. Bisikalo, A. A. Boyarchuk, O. A. Kuznetsov, and V. M. Chechetkin, Astron. Zh. **74**, 880 (1997) [Astron. Rep. **41**, 786 (1997)].
6. D. V. Bisikalo, A. A. Boyarchuk, O. A. Kuznetsov, and V. M. Chechetkin, Astron. Zh. **74**, 889 (1997) [Astron. Rep. **41**, 794 (1997)].
7. P. L. Roe, Annu. Rev. Fluid Mech. **18**, 337 (1986).
8. O. M. Belotserkovskiĭ and Yu. M. Davydov, *Method of Large Particles in Gas Dynamics* [in Russian] (Nauka, Moscow, 1982).
9. L. D. Landau and E. M. Lifshitz, *Course in Theoretical Physics. Vol. 4: Fluid Mechanics* (Nauka, Moscow, 1986; Pergamon, New York, 1987).
10. M. V. Abakumov, S. I. Mukhin, Yu. P. Popov, and V. M. Chechetkin, Astron. Zh. **73**, 407 (1996) [Astron. Rep. **40**, 366 (1996)].
11. M. V. Abakumov, S. I. Mukhin, and Yu. P. Popov, Mat. Model. **12**, 110 (2000).
12. D. V. Bisikalo, A. A. Boyarchuk, O. A. Kuznetsov, and V. M. Chechetkin, Astron. Zh. **76**, 905 (1999) [Astron. Rep. **43**, 797 (1999)].

Translated by D. Gabuzda

Astronomy Reports, Vol. 45, No. 6, 2001, pp. 442–451. Translated from Astronomicheskiĭ Zhurnal, Vol. 78, No. 6, 2001, pp. 514–524.

Diagnostics for Accretion Disks Around UX Ori Stars Based on Balmer, Paschen, and Brackett Lines

L. V. Tambovtseva[1], V.P. Grinin[1, 2], B. Rodgers[3], and O.V. Kozlova[2]

[1]*Pulkovo Observatory, Russian Academy of Sciences, Pulkovskoe sh. 65, St. Petersburg, 196140 Russia*

[2]*Crimean Astrophysical Observatory, National Academy of Sciences of Ukraine, p/o Nauchnyĭ, Crimea, 334413 Ukraine*

[3]*University of Washington, Box 351580, Seattle, Washington 98195-1580 USA*

Received September 14, 2000

Abstract—We have modeled the H_α, H_β, and H_γ (Balmer series), P_{14} (Paschen series), and Br_γ (Brackett series) hydrogen lines formed in the inner regions of the accretion disk around the Herbig Ae star UX Ori. Our calculations are based on spectra obtained with the Nordic Optical Telescope (NOT) and the IRTF. We computed a grid of non-LTE models for a radiating area in the accretion disk and determined the basic parameters of the lines using the method of Sobolev. Analyzing the theoretical and observed line profiles, equivalent widths, and luminosities, we have estimated the accretion rate and electron-temperature distribution in the inner parts of the accretion disk. The accretion rate of UX Ori is about $\dot{M}_a = (3\text{–}10) \times 10^{-9} M_\odot$/yr, and the temperature distribution is consistent with the power law $T(r) = T(r_*)(r/r_*)^{-1/n}$, where the electron temperature near the stellar surface $T(r_*)$ is 15000–20000 K and the power-law index $n \approx 2\text{–}3$ is about two to three. The resulting value for $\dot{M}_a$ eliminates problems connected with the application of magnetospheric accretion models to Herbig Ae/Be stars. Another important conclusion is that, at the estimated accretion rate, the energy release is substantially (about two orders of magnitude) lower than the stellar luminosity. Therefore, the optical radiation of UX Ori accretion disks cannot appreciably contribute to the observed variability of these stars, which must be determined mainly by variability in the circumstellar extinction. © *2001 MAIK "Nauka/Interperiodica".*

1. INTRODUCTION

The Herbig Ae star UX Ori [1] is the prototype for a class of young stars with nonperiodic Algol-type brightness minima, which have been actively studied for years. They are mainly distinguished by violent, unpredictable photometric activity, with amplitudes reaching $2\text{–}3^m$ [2–4]. The brightness minima are accompanied by an increase of the linear polarization of the star by up to 5–8% [4–6], indicating the presence of eclipses due to circumstellar dust envelopes. During the eclipses, the direct (unpolarized) radiation of the star decreases so that the relative contribution of the radiation scattered by the circumstellar dust increases. This explains not only the increase of the linear polarization but also the "turnaround" of the color tracks in color–magnitude diagrams [7]. The high degree of polarization suggests that the circumstellar gas and dust envelopes are very flattened (we will call them disks below, for the sake of brevity) and are viewed edge-on or at a small angle to the line of sight. This is apparently the main reason for the violent photopolarimetric activity of these stars.

Another important feature of UX Ori stars that also appears to be due to the "optimal" orientation of their circumstellar disks is the presence of spectroscopic signs of gas accretion, seen both in metallic and Balmer lines [8–12]. There is ample evidence that the accretion resembles the infall of circumstellar matter onto β Pic [8, 9, 13], which is due to the evaporation of cometlike bodies in the vicinity of the star [14]. On the other hand, the H_α emission in the spectra of UX Ori stars and the fact that this line (as well as the He I 5876 Å line) often displays an accretion profile indicate that the bulk of the accreted matter comes into the vicinity of the star from the circumstellar gas–dust disk [13, 15]. This is also indicated by the recent analysis [16] of the approximate chemical composition (hydrogen to metal ratio) of the matter accreted onto UX Ori.

Thus, thanks to their "optimal" orientation, we view UX Ori stars directly through circumstellar disks—a circumstance we make use of in our emission-line modeling. Here, we consider the innermost region of the accretion disk, where a considerable fraction of the hydrogen line emission is formed. Non-LTE modeling for these lines enables us to determine the accretion rate of the circumstellar gas and the temperature distribution in the accretion disk, which in turn can be used to estimate the rate of release of accretion energy. This last quantity is of considerable interest in the context of the hypothesis that the accretion disk makes an appreciable contribution to

1063-7729/01/4506-0442$21.00 © 2001 MAIK "Nauka/Interperiodica"

the optical radiation of UX Ori stars (see, for example, [17]).

2. FORMULATION OF THE PROBLEM

For young, low-mass T Tauri stars, the magnetospheric-accretion model provides a reasonable description of the interaction between the accretion disk and the star (see the review [18] and references therein). In this model, a cool, geometrically thin accretion disk is the source of accreted matter. At some distance r_c from the star (the corotation radius), the disk material collides with the magnetosphere. As a result, the type of gas motion is dramatically altered: the quasi-Keplerian rotation of the disk switches to solid-body rotation and free fall of the accreted gas onto the star. It is this innermost region (in the case of T Tauri stars, its characteristic size is about 5–10 stellar radii [19]) that is thought to be responsible for the formation of most of the line emission in these stars. The hottest regions, where lines of atoms and ions with high ionization and excitation potentials originate, are located in the immediate vicinity of the stellar surface [20].

For young stars of intermediate mass, the magnetospheric-accretion model remains without comparable quantitative justification [18]. In particular, there is no direct evidence for large-scale magnetic fields on the surfaces of these stars [21], though some indirect indications are available (see, for example, [22]). Nevertheless, it seems reasonable to try to adapt the magnetospheric-accretion model to stars of this type, since a statistical analysis of the observed H_α profiles [23] indicates that the large-scale structure of the velocity fields in the circumstellar gaseous envelopes of these stars corresponds roughly to those expected in the model.

In our previous study [15], we considered a simplified model for the accretion disk of an UX Ori star, in which the radial and azimuthal velocity components vary according to the law v, $u \sim r^{-1/2}$. This model can describe in general terms the observed Balmer-line intensities and profiles for comparatively low accretion rates (of the order of 10^{-8} to $10^{-9} M_\odot$/yr). The He I 5876 Å line is formed in the immediate vicinity of the star, where the bulk of the accretion energy is released; in this region, the rotational velocity of the accretion disk decreases, approaching that of the star itself. This type of variation for the rotational velocity of the gas indicates the presence of a corotation zone in the accretion disk, the angular velocity of which is determined by the rotation of the star itself.

Based on these results, we consider here in more detail the formation of the emission spectrum of a UX Ori star taking the corotation zone into account. Together with the Balmer lines, we also analyze lines of the Paschen (P_{14}) and Brackett (Br_γ) series. Most of the gas radiating in these two lines is optically thin (especially P_{14}), which makes the results of our diagnostics less dependent on the optical conditions in the radiating region, and, consequently, more reliable.

Although the geometrical thickness of the disk in current accretion models increases with distance from the star [24], we consider a simplified model of an accretion disk with constant geometrical thickness $2h$. This approach is justified, since we consider the part of the disk in the immediate vicinity of the star, where the requirements of the standard Shakura–Syunayev disk accretion model [25] are violated due to the rapid increase of the gas temperature and the influence of the magnetic field. Using supplementary information about metallic absorption lines originating in the circumstellar gaseous disks of UX Ori stars, we estimated $h \approx (0.5–1)\, r_*$ in [15].

3. OBSERVATIONAL DATA

NOT spectra. Balmer and Paschen lines. We used spectral observations obtained in 1994–1996 with the Nordic Optical Telescope (NOT), La Palma, with resolution $R = 25000$ for a sample of UX Ori stars. The same stars were simultaneously monitored photometrically at the Crimean Astrophysical Observatory. A detailed description of the instrumentation and spectra will be published by Grinin *et al.* [12]. We used the first three Balmer lines H_α, H_β, and H_γ and the P_{14} (λ 8600Å) line in UX Ori on dates when the star was in its regular bright state for our modeling.

IRTF spectra. Balmer and Brackett lines. We used another hydrogen line, Br_γ (λ 21656 Å), from the spectrum of UX Ori to diagnose the accretion disk. The observations were made by Rodgers *et al.* [26] in February 1999 with the NASA Infrared Telescope Facility (IRTF) (Mauna Kea) and the high-resolution CSHELL IR spectrograph ($R = 36000$). In order to determine the luminosity of the emission component of the line, the spectrum of a normal star of the same spectral type was obtained, normalized to the V stellar magnitude of UX Ori, and subtracted from the spectrum of UX Ori. Some optical spectra were simultaneously observed at Apache Point Observatory with the Dual Imaging Spectrograph ($R = 2500$). The same procedure was applied to estimate the H_α luminosity of UX Ori, with the only difference being that a synthetic spectrum for the appropriate Kurucz model was used instead of the spectrum of a reference star. Photometric measurements made before and after the spectral observations indicated that UX Ori was also in its bright state ($V \approx 9.8$) at this time. This set of observations is described in more detail in [26].

Table 1 presents the spectral data along with the line luminosities and equivalent widths estimated from these observations.

4. KINEMATICAL MODEL FOR THE RADIATING REGION

Taking the above into account, we have assumed that the disk material rotates with a Keplerian velocity distribution right up to the corotation radius r_c. The

Table 1. Luminosities and equivalent widths of H_α, P_{14}, and Br_γ lines as inferred from observations of UX Ori

Line	Date	Reference	Line luminosity, 10^{31} erg/s^{-1}	EW, Å
H_α	Feb. 4, 1999	[26]	4	–
Br_γ	Feb. 6, 1999	[26]	0.34	–
H_α	Nov. 19, 1994	[12]	3.7	8.4
H_α	Dec. 2, 1995	[12]	4.4	10.8
H_α	Dec. 4, 1995	[12]	6.2	14
H_α	Nov. 25, 1996	[12]	3.5	8
P_{14}	Nov. 19, 1994	[12]	0.31	0.78
P_{14}	Dec. 2, 1995	[12]	0.21	0.53
P_{14}	Dec. 4, 1995	[12]	0.28	0.7
P_{14}	Nov. 25, 1996	[12]	0.31	0.77

kinematic conditions in the corotation zone are determined by the equation of motion in which the gravitation of the star and the centrifugal force dominate. The value of r_c can be roughly estimated from the condition that the magnetic and kinetic energy be equal in an elementary volume: $\rho u^2/2 = H^2/8\pi$, where H is the magnetic field strength, ρ the gas density, and u the rotational velocity. Assuming a dipolar magnetic field ($H \sim r^{-3}$) and Keplerian rotation and estimating the gas density using the continuity equation and accretion rate $\dot{M}_a$, we can easily derive an expression relating the corotation radius to the magnetic-field strength at the stellar surface H_* and also to the mass of the star M_* and its radius r_*: $r_c/r_* = r_*^{1/2} H_*^{1/2} (h\nu/G\dot{M}_a M_*)^{1/4}$. Here, ν is the radial component of the gas velocity in the disk (assumed below to be 50 km/s). Adopting in this relation $H_* = 500$ G[1] $\dot{M}_a = 10^{-8} M_\odot$/yr, $M_* = 3M_\odot$, $h = r_*$, and $r_* = 3r_\odot$, we obtain $r_c \approx 1.5 r_*$. Note that this estimate depends only weakly (to the one-quarter power) on the poorly known disk thickness $2h$ and velocity ν. It follows from this estimate that the corotation zone is close to the star. In our calculations, we adopt $r_c = 2r_*$.

According to the data of [27], the rotational velocity of UX Ori is 140 km/s. Taking this into account, the velocity of solid-body rotation at $r = r_c$ is 300 km/s, while the Keplerian rotational velocity is about 310 km/s. Therefore, either the transition from the accretion disk to the corotation zone occurs without a discontinuity in the tangential velocity component or this discontinuity is small. Thus, in contrast to T Tauri stars, for which the corotation radius is five to ten stellar radii, the accretion disks of Herbig Ae/Be stars approach much closer to the stars due to their faster rotation [28]. Therefore, in calculations of Herbig Ae/Be emission spectrum, we must take into account not only the radiation of gas in the corotation region, but (unlike the T Tauri case) also radiation originating in the accretion disk itself.

Based on this, we adopt the following model for the radiating region: the accretion disk is dominated by Keplerian rotation in combination with a small radial velocity component. For the sake of simplicity, we assume the latter to vary according to the same law as the Keplerian velocity ($\nu \sim r^{-1/2}$) and to reach 50 km/s at $r = r_c$. At r_c, the Keplerian and corotation rotational velocities are matched, and, in the corotation zone, the rotation is solid-body right to the surface of the star:

$$u(r) = \begin{cases} u(r_*)(r/r_*) & \text{at} \quad r \le r_c \\ u_k (r/r_*)^{-1/2} & \text{at} \quad r > r_c. \end{cases} \tag{1}$$

The same procedure is applied to determine the radial velocity, which, in the corotation zone, is specified by the gravitation of the star and the centrifugal force:

$$\nu(r)\frac{d\nu}{dr} = -\frac{GM_*}{r^2} + \frac{u^2(r)}{r}. \tag{2}$$

Hence, taking (1) into account, we obtain after simple manipulation the relation for the velocity of the infalling gas in the corotation zone

$$\nu(r) = \begin{cases} \sqrt{\nu(r_c)^2 + \nu_{\rm esc}^2 (r_*/r - r_*/r_c) - \frac{1}{2} u(r_*)^2 [(r_c/r_*)^2 - (r/r_*)^2]} & \text{at} \quad r \le r_c \\ \nu(r_c)(r/r_*)^{-1/2} & \text{at} \quad r > r_c. \end{cases} \tag{3}$$

Here, $\nu(r_c)$ is the radial component of the gas velocity at $r = r_c$, $u(r_*)$ is the rotational velocity of the gas near the stellar surface (assumed to be equal to the rotational velocity of the star), $\nu_{\rm esc}$ is the escape velocity near the surface of the star, and $u_k = 440$ km/s is the Keplerian rotational velocity of the gas near the stellar surface. Despite the fact that $u(r_*)$ and $\nu(r_c)$ are input parameters, we encounter no difficulties in choosing them, since spectral observations provide information about the components of the gas velocity in the vicinity of the star. The rotational velocity of the star is also known from the known orientation of the rotational axis of the

[1] Given the large rotation velocity of Herbig Ae/Be stars, the adopted magnetic field strength is beyond the detection limit for a classical Zeeman analysis and, consequently, does not contradict the negative results of the observations [21].

Table 2. Model parameters

Model	$T(r_*)$, K	n	h/r_*	Model	$T(r_*)$, K	n	h/r_*
1	10000	2	0.5	7	10000	2	1
2	15000	2	0.5	8	15000	2	1
3	20000	2	0.5	9	20000	2	1
4	10000	3	0.5	10	10000	3	1
5	15000	3	0.5	11	15000	3	1
6	20000	3	0.5	12	20000	3	1

star $\sin i \approx 1$. For $u(r_*) = 140$ km/s and $v(r_c) = 50$ km/s, the velocity law has the form presented in Fig. 1.

5. CALCULATION TECHNIQUE

The most challenging problem is the calculation of thermal balance in the radiating region, since there is no universal cooling function in the considered temperature range in an opaque plasma [29]. In addition, the gas heating function in the region under consideration is not entirely clear. Therefore, we adopted a power-law distribution for the temperature T in the envelope: $T(r) = T(r_*)(r/r_*)^{-1/n}$, where n is a parameter specifying the temperature profile of the accretion disk. In the study [15], we failed to set stringent limits on the temperature distribution in the accretion disk. Nonetheless, by fitting line profiles and verifying the results with the observed Balmer decrement (the intensity ratio $I_{H_\alpha} : I_{H_\beta} : I_{H_\gamma}$), we concluded that the best consistency between the calculated and observed Balmer line profiles was provided by models with $T(r_*) \approx 15000$ K and $n = 2$–3.

As in [15], our line-profile calculations were based on the exact expression for the emerging radiation intensity, while the level populations and source functions were determined in a Sobolev approximation [30] for media with a velocity gradient. Note that, as was shown in [31], the kinematic model considered belongs to the class of models with nonlocal radiative coupling. In such models, the equation for the source function contains an additional integral term that corresponds to radiation of the surfaces of comoving points [32, 33]. However, in our case, the disk is flat ($2h \ll R_d$, where R_d is the outer disk radius), so that the contribution of this term is negligible [30].

We took the energy distribution for UX Ori from Kurucz models [34] for $T_{\rm eff} = 9500$ K and $\log g = 4$. Analysis of shell components in the spectra of UX Ori stars show that the parameter h can reach values comparable to the stellar radius. Therefore, we carried out our calculations for the two values $h = 0.5r_*$ and $h = 1r_*$. The disk density was determined from the continuity equation for the case of a two-dimensional, axially symmetrical flow. We took into account the broadening of photosphere profiles due to the rotation of the star in the line-profile calculations.

Table 2 presents the parameters of the models considered. Having fixed the kinematics of the flow (Fig. 1), the outer radius of the disk $R_d = 10r_*$, and its thickness, we calculated the ionization state and level populations for a ten-level model of the hydrogen atom using the code described in [35]. Further, we determined the intensities, profiles, equivalent widths, and luminosities of all the lines considered for a set of $\dot{M}_a$ values in the interval from $10^{-7}M_\odot$/yr to $10^{-9}M_\odot$/yr. In the case of the P_{14} line, we took into account the fact that the Menzel parameter for the upper level of this transition is equal to unity with high accuracy in the considered density range. Figures 2–7 present the results of our calculations.

6. RESULTS

Figure 2 presents the theoretical luminosities in the H_α and Br_γ lines for models with temperature profiles corresponding to $n = 3$ and $T(r_*) = 10000$, 15000, and

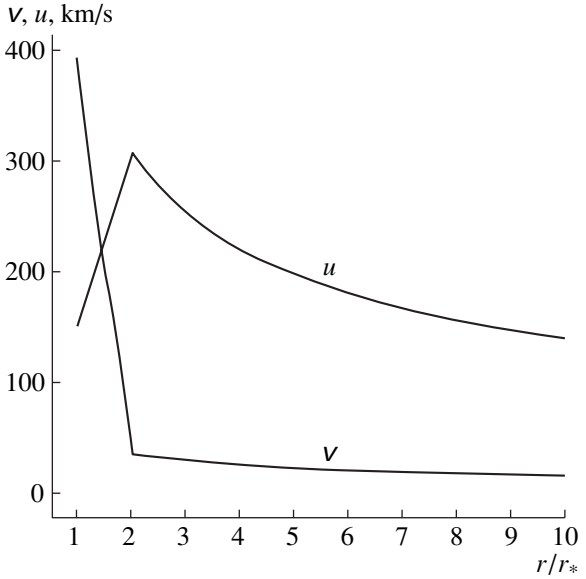

Fig. 1. Radial v and tangential u velocity components of the accretion flow as a function of distance from the star.

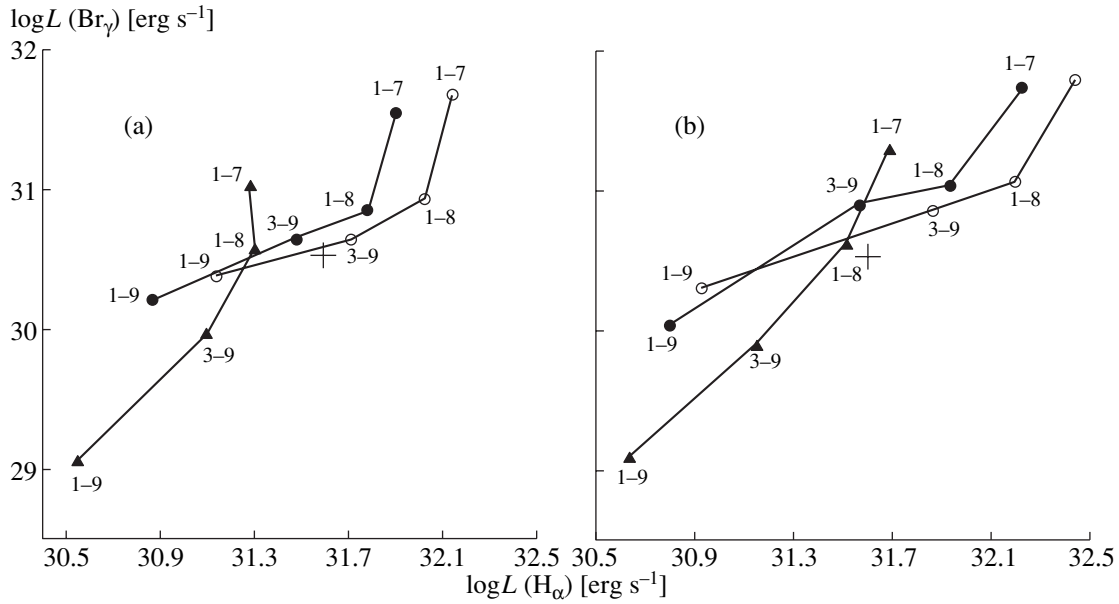

Fig. 2. Logarithms of the luminosity in the H_α and Br_γ lines as a function of the accretion rate for (a) thin (h = 0.5) and (b) thick (h = 1) disks for models with the temperature power-law index n = 3. The accretion rate is marked in solar masses per year (for example, 1–9 corresponds to $1 \times 10^{-9} M_\odot$). The hollow circles correspond to $T(r_*)$ = 20000 K, filled circles to 15000 K, and triangles to 10000 K. The crosses "┼" indicate the observed UX Ori line luminosities from [26].

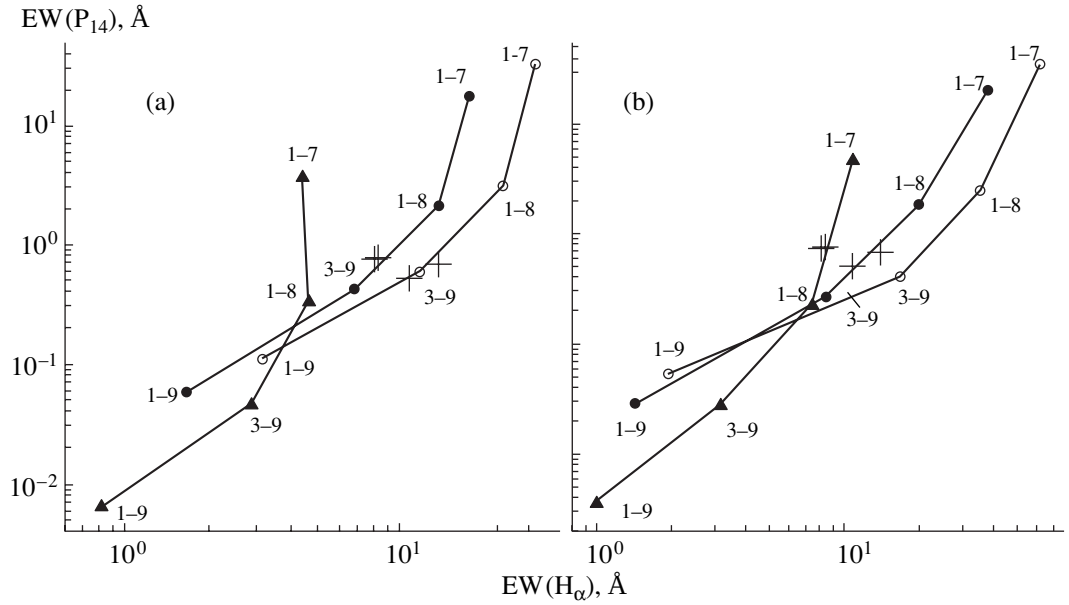

Fig. 3. Calculated equivalent widths for the H_α and P_{14} lines for n = 3 and (a) h = 0.5 and (b) h = 1. The crosses indicate the corresponding values for UX Ori observed with NOT [12]. Notation for the models is the same as in Fig. 2.

20000 K for h = 0.5 (Fig. 2a) and h = 1 (Fig. 2b). The crosses indicate the IRTF data of UX Ori. The numbers in the figures indicate the accretion rates for which we carried out the calculations: $\dot{M}_a = 1 \times 10^{-9}$, 3×10^{-9}, 1×10^{-8} and $1 \times 10^{-7} M_\odot$/yr. Figure 3 presents the H_α and P_{14} equivalent widths for the same $\dot{M}_a$. The crosses indicate the NOT data for these equivalent widths. Note that our theoretical luminosity estimates assume isotropic propagation of the radiation, which is, generally speaking, not the case in reality. Only the luminosity of Br_γ

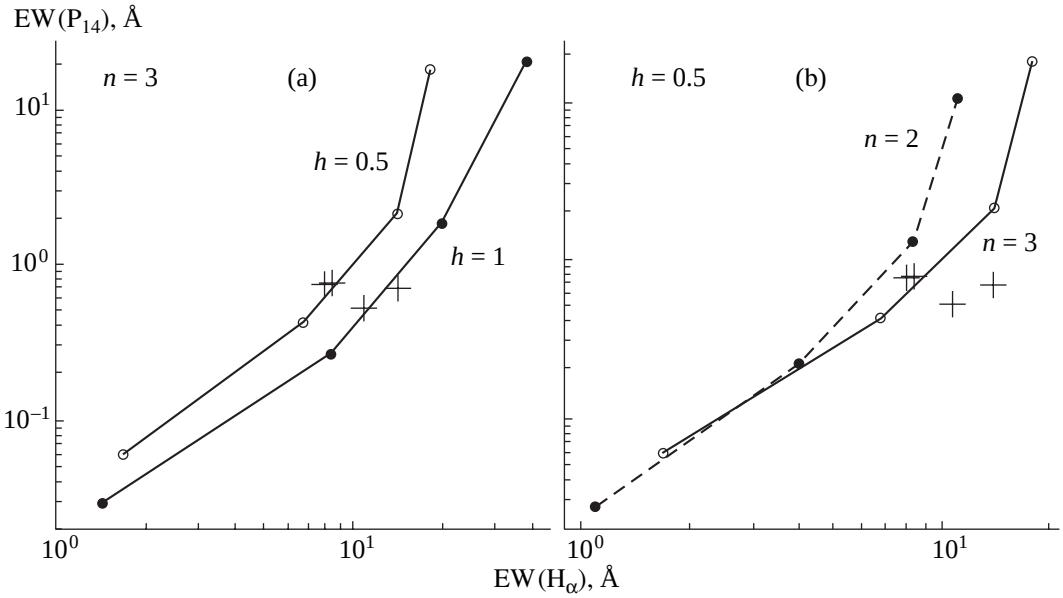

Fig. 4. The influence of model parameters on the results: the P_{14} and H_α equivalent widths for different (a) geometrical thicknesses of the disk and (b) temperature gradients. In case (a), models 5 and 11 are compared, while models 2 and 5 are compared in case (b). The crosses indicate the corresponding values for UX Ori observed with NOT [12].

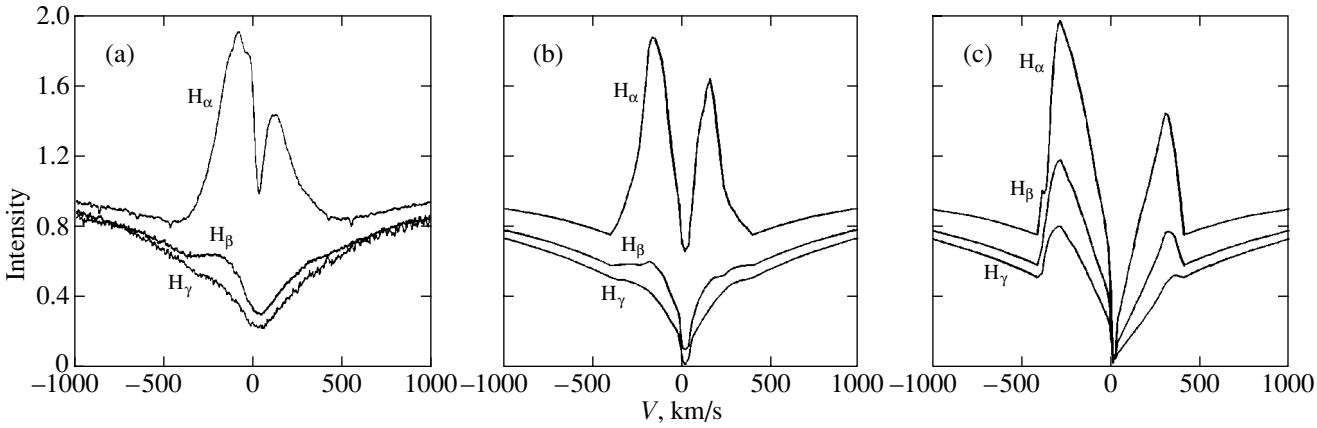

Fig. 5. H_α, H_β, and H_γ profiles of UX Ori (a) observed, averaged over four dates in 1995 and calculated in models (b) 12 and (c) 10. The accretion rates in the model calculations are (Model 12) $2.3 \times 10^{-9} M_\odot$/yr and (Model 10) $10^{-7} M_\odot$/yr.

can be considered, due to certain peculiarities in the measurement technique and normalization for this line [26].

Our calculations indicate that increasing the geometrical thickness of the disk h shifts the curves in $EW(H_\alpha) - EW(P_{14})$ diagrams to the right (Fig. 4a). This is due to the fact that variations of h affect the equivalent width of the P_{14} line (which is at frequencies where the radiating region is optically thin) less then that of the H_α line. Increasing the temperature gradient (decreasing n) shifts the curves to the left only for high and moderate accretion rates ($>10^{-8} M_\odot$/yr; Fig. 4b). When $\dot{M}_a < 10^{-8} M_\odot$/yr, these curves become closer or simply coincide. Note that variation of these two parameters within the considered limits does not fundamentally affect the results.

Considering the results for all the lines (Figs. 2–5), we conclude that the accretion rate is in the interval $(2–10) \times 10^{-9} M_\odot$/yr, and the temperature distribution is described adequately by models with the initial temperatures $T(r_*) = (15\,000–20\,000)$ K and the power-law index $n \approx 2–3$. The figures indicate that the observations correspond somewhat better to curves with a flatter temperature gradient ($n = 3$). Our analysis also takes into account the theoretical Balmer decrements. Profile fitting for the first three Balmer lines provides an independent criterion for our estimates of the accretion rate and disk temperature. An example is presented in Fig. 5, which displays the Balmer profiles that were observed (Fig. 5a) and those calculated using two models: 12 (Fig. 5b) and 10 (Fig. 5c). In both cases, the H_α

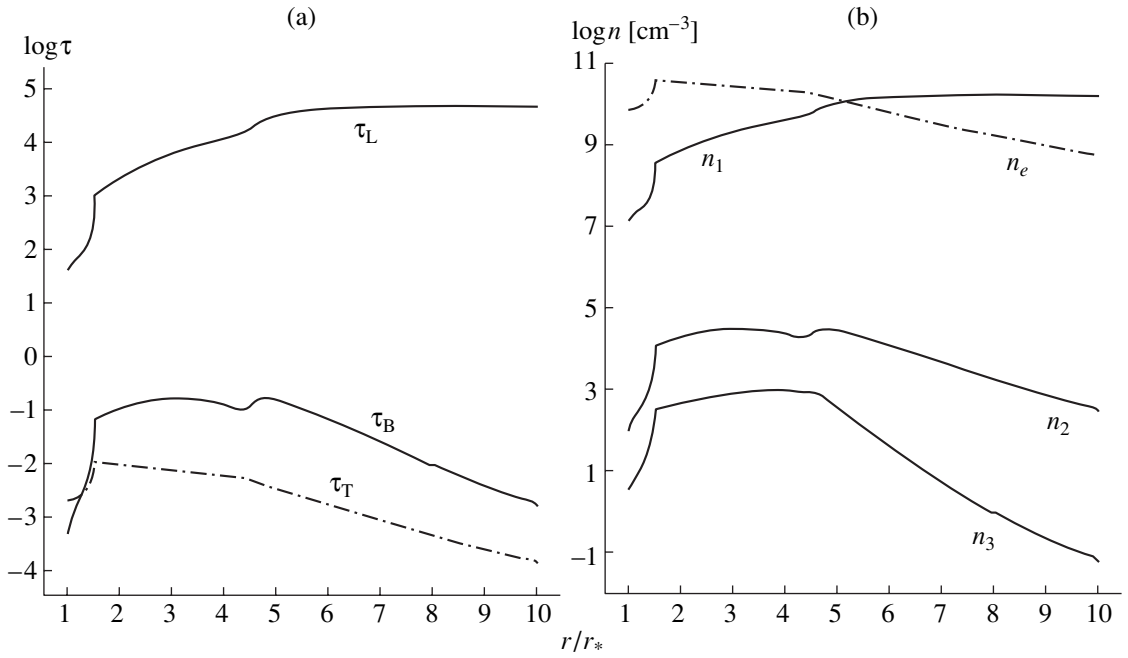

Fig. 6. (a) Optical depths in the Lyman τ_L and Balmer τ_B continua and in the case of Thomson scattering τ_T; (b) population for the first three levels and electron density n_e as a function of the distance from the star, calculated in model 11.

equivalent widths coincide with the observed values, but the Balmer decrement is close to the observed decrement only for model 12.

Our calculations indicate that models with small temperature gradients ($n > 4$) do not reproduce the observed Balmer profiles well. We also conclude that, independent of the temperature gradient or geometrical thickness of the disk, the temperature distribution with $T(r_*) = 10000$ K either does not fit the observed Br_γ and P_{14} equivalent widths (luminosity) or fails to satisfy another criterion—consistency between the theoretical and observed Balmer decrement.

Figure 6 presents the transverse optical depths of a circumstellar gaseous disk in the Lyman τ_L and Balmer τ_B continua and the continuum corresponding to Thomson scattering τ_T (Fig. 6a). The populations of the first three levels and the electron density as a function of distance from the star are also presented (Fig. 6b). The calculations were made for a model which provides good agreement between the theory and observations: $\dot{M}_a = 5 \times 10^{-9} M_\odot$/yr; $T(r_*) = 15000$, $n = 3$, $h = 1$. We can see that the accretion disk is transparent in all continua except for the Lyman continuum, while its maximum optical depth due to Thomson scattering is around 10^{-2}. The corresponding lateral optical depths of the disk in this model are $\tau_L = 1.3 \times 10^5$, $\tau_B = 0.33$, and $\tau_T = 1.6 \times 10^{-2}$.

It is obvious that we cannot in general expect that a "UX Ori star + accretion disk" system is exactly edge-on and that the angle α between the line of sight and the disk plane is zero. Indeed, as was shown recently in [36], the observed polarization of these stars in deep minima can also be explained for disk inclinations up to 10°–20°. Therefore, we also calculated line profiles for the case of an inclined disk, assuming the maximum inclination angle to be 20°. An inclination around 10° yielded somewhat better consistency between the theoretical and observed profiles: the calculated profiles become more symmetrical, and the central absorption, more shallow.

7. DISCUSSION

Our results indicate that the magnetospheric accretion model developed for young low-mass T Tauri stars [28, 37–40] can be adapted to young intermediate-mass stars. Here, the corotation radius is smaller than for T Tauri stars; therefore, the approach of the accretion disk to the star is closer and its radiation contributes appreciably to the line emission. In addition, most circumstellar absorption lines (shell components) are apparently formed in the accretion disks of Herbig Ae/Be stars. The low accretion rate ($M_a = 10^{-8}$–$10^{-9} M_\odot$/yr) in combination with the larger luminosity of these stars explains why intermediate-mass young stars, unlike T Tauri stars, do not experience veiling of their photospheric lines by the optical radiation of the boundary layer. For the same reason, the boundary layer cannot give rise to appreciable optical variability of the star, as suggested recently by Herbst and Shevchenko [17]. The asymmetry of the forbidden lines in Herbig Ae/Be

stars is weakly pronounced or not seen at all, which is sometimes considered to be an argument against the existence of accretion disks in these stars [41]. Recall, however, that, in this case, the radius for the sublimation of dust grains is located substantially farther from the star, at a distance of several AU. Thus, unlike the situation in cooler, young T Tauri stars, the screening of the dust disks in Herbig Ae/Be stars (which gives rise to the asymmetry of the forbidden lines [42]) should be much less effective.

Let us consider another aspect of the problem: the influence of the stellar wind. In disk accretion models, mass outflow is known to be a direct consequence of the accretion; it carries away the bulk of the angular momentum of the infalling matter (see, for example, [28, 37]). Therefore, stellar winds should also exist in UX Ori stars. Note that, among all Herbig Ae/Be stars, only UX Ori stars display clear signs of accretion, whereas, in other Herbig Ae/Be stars, these signs are either distorted by the wind (complicated H_α emission profiles are seen in the spectra) or are entirely absent (H_α has a P Cygni profile). The edge-on orientation of the circumstellar disks around UX Ori stars evidently suppresses the influence of the stellar wind on the formation of emission lines. The sole exception might be WW Vul: for this star, the intensity ratio V/R of the H_α "blue" and "red" components varies slightly from values for "wind" (<1) to "accretion" (>1) and back [12]. This system (star + disk) may be inclined to the line of sight, so that the wind and the accretion take turns in dominating.

To be certain that our results depend only weakly on the presence of a stellar wind, we made a test calculation for H_α profiles in one of the above models, having added the contributions of an accretion disk and stellar wind. According to [28, 43], the rate of mass loss in the form of magneto-centrifugal wind $\dot{M}_w$ is related to the accretion rate $\dot{M}_a$ by the expression $\dot{M}_w = f\dot{M}_a$, where the parameter f can take on values from 0.1 to 0.3. We assumed that the stellar wind originates at the surface of the accretion disk in the vicinity of the corotation zone and fills a region with the opening angle $\pi/2$; the matter outflow decelerates ballistically, and the rotational velocity in the wind decreases in accordance with angular-momentum conservation, inversely proportion to the distance from the axis of symmetry. The maximum rotational velocity (for $r = r_c$) and the outflow velocity are assumed to be 300 km/s. The temperature is specified to be $T(r_*) = 15000$ K for both the disk and the wind, with $n = 3$ in both cases. The ionization and excitation state of hydrogen atoms in the stellar wind is calculated using the same method as for the accretion disk. The results are presented in Fig. 7. We can see that, in the case of an edge-on accretion disk, the presence of the wind leaves the H_α profile essentially unaffected for f between 0.1 and 0.5.

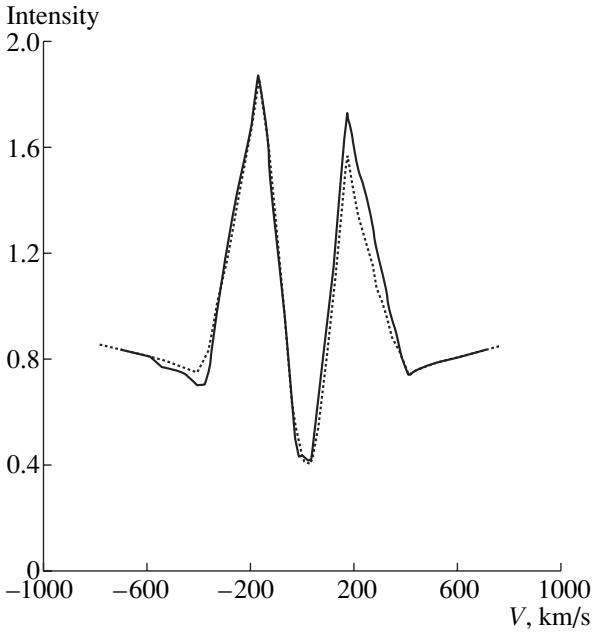

Fig. 7. Influence of the stellar wind on the H_α profile of UX Ori for $\dot{M}_a = 10^{-8} M_\odot$/yr and $\dot{M}_w = 3 \times 10^{-9} M_\odot$/yr. $T(r_*) = 15000$ K, $n = 3$, $r_c = 1.5r_*$, and $h = 0.5r_*$. The half-opening angle for the wind is assumed to be 45°. The solid curve corresponds to the case when the wind is taken into account in the calculations, and the dotted curve, to the calculations without the wind.

8. CONCLUSIONS

Summarizing, we can draw the following conclusions.

(1) We have shown using the example of the Herbig Ae star UX Ori that the magnetospheric-accretion model developed for young, low-mass T Tauri stars can satisfactorily reproduce the intensities and profiles of hydrogen lines in the spectrum of a young star of intermediate mass. The main difference between these two types of stars is that the corotation radius is smaller for Herbig stars than for T Tauri stars. As a result, the accretion disks in Herbig stars are located closer to the star and their radiation contributes substantially to the stellar emission spectrum.

(2) Due to the special orientation of the circumstellar disks around UX Ori stars (edge-on or at a small angle to the line of sight), the accretion profiles of lines dominate in their spectra, which include numerous absorption lines of a circumstellar origin (shell components). Spectroscopic signs of the stellar wind are weak or completely undetectable, since the thickness of the accretion disk in the vicinity of the star is comparable to the diameter of the star itself. As a result, the outflowing matter is not projected onto the stellar disk and a P Cygni profile is not formed.

(3) The rate of accretion of circumstellar gas onto UX Ori does not exceed $\dot{M} = 10^{-8} M_\odot$/yr, and the tem-

perature variation with radius is well represented by the relation $T(r) = T(r_*)(r/r_*)^{-1/n}$, where the temperature of the gas near the stellar surface $T(r_*)$ is 15000–20000 K and the power-law index n is roughly equal to two to three. The energy release for this accretion rate appears to be appreciably smaller than the luminosity of the star itself (by about two orders of magnitude). Therefore, the accretion disks around UX Ori stars are unable to contribute appreciably to their optical radiation and do not determine their observed variability, which is due mainly to variable circumstellar extinction [4]. Note that this is true only of quasi-stationary accretion and so characterizes the situation on average. Under the real conditions of an inhomogeneous circumstellar medium, both the accretion rate and energy-release rate can fluctuate, for example, due to collisions of massive gas and dust clouds.

In conclusion, we stress that these results refer primarily to Herbig Ae/Be stars of late spectral types. In the case of early-type Herbig Be stars, the dynamical parameters of the circumstellar gas are, to a much greater extent, specified by the radiation field of the stars [44, 45] whose luminosity exceeds those of Herbig Ae stars by a factor of several tens.

ACKNOWLEDGMENTS

This study was supported by the Russian Foundation for Basic Research (project no. 99-02-18520 and 99-02-16336) and the State Scientific and Technology Program "Astronomy."

REFERENCES

1. P. S. Thé, in *The Nature and Evolutionary Status of Herbig Ae/Be Stars*, Ed. by P. S. Thé, M. R. Pérez, and E.J.P. van den Heuvel; Astron. Soc. Pac. Conf. Ser. **62**, 23 (1994).
2. G. V. Zaĭtseva, Perem. Zvezdy **19**, 63 (1973).
3. W. Herbst, D. K. Herbst, E. J. Grossman, and D. Weinstein, Astron. J. **108**, 1906 (1994).
4. V. P. Grinin, N. N. Kiselev, N. Kh. Minikulov, *et al.*, Astrophys. Space Sci. **186**, 283 (1991).
5. V. P. Grinin, Astron. Astrophys. Trans. **3**, 17 (1992).
6. V. P. Grinin, in *The Nature and Evolutionary Status of Herbig Ae/Be Stars*, Ed. by P. S. Thé, M. R. Pérez, and E. J. P. van den Heuvel; Astron. Soc. Pac. Conf. Ser. **62**, 63 (1994).
7. V. P. Grinin, Pis'ma Astron. Zh. **14**, 65 (1988) [Sov. Astron. Lett. **14**, 27 (1988)].
8. V. P. Grinin, P. S. Thé, D. de Winter, *et al.*, Astron. Astrophys. **392**, 165 (1994).
9. S. Grady, M. R. Pérez, A. Talavera, *et al.*, Astron. Astrophys., Suppl. Ser. **120**, 157 (1996).
10. O. V. Kozlova, V. P. Grinin, and A. N. Rostopchina, Astron. Zh. **77**, 42 (2000) [Astron. Rep. **44**, 36 (2000)].
11. C. A. Grady, M. L. Sitko, R. W. Russel, *et al.*, in *Protostars and Planets IV*, Ed. by V. Mannings, A. P. Boss, and S. R. Russell (Univ. of Arizona Press, Tucson, 2000). p. 613.
12. V. P. Grinin, O. V. Kozlova, A. Natta, *et al.* (2000), in preparation.
13. V. P. Grinin, O. V. Kozlova, P. S. Thé, and A. N. Rostopchina, Astron. Astrophys. **309**, 474 (1996).
14. A.-M. Lagrange-Henry, A. Vidal-Madjar, and R. Ferlet, Astron. Astrophys. **190**, 275 (1988).
15. L. V. Tambovtseva, V. P. Grinin, and O. V. Kozlova, Astrofizika **42**, 75 (1999).
16. A. Natta, V. P. Grinin, and L. V. Tambovtseva, Astrophys. J. **542**, 421 (2000).
17. W. Herbst and V. S. Shevchenko, Astron. J. **118**, 1043 (1999).
18. L. Hartmann, New Astron. Rev. **45**, 1 (1999).
19. A. Königl, Astrophys. J. Lett. **370**, L39 (1991).
20. S. A. Lamzin, Astron. Zh. **66**, 1330 (1989) [Sov. Astron. **33**, 685 (1989)].
21. Yu. V. Glagolevskij and G. A. Chountonov, Bull. Spec. Astrophys. Obs. **45**, 105 (1998).
22. F. Praderie, T. Simon, C. Catala, and A. Boesgaard, Astrophys. J. **303**, 311 (1986).
23. V. P. Grinin and A. N. Rostopchina, Astron. Zh. **73**, 194 (1996) [Astron. Rep. **40**, 171 (1996)].
24. S. J. Kenyon and L. W. Hartmann, Astrophys. J. **323**, 714 (1987).
25. N. I. Shakura and R. A. Sunyaev, Astron. Astrophys. **24**, 337 (1973).
26. B. Rodgers, C. B. Woodward, and D. H. Wooden, Astron. J. (2000) (in press).
27. V. P. Grinin and O. V. Kozlova, Astrofizika **43**, 329 (2000).
28. F. Shu, J. Najita, E. Ostriker, *et al.*, Astrophys. J. **429**, 781 (1994).
29. V. P. Grinin and A. S. Mitskevich, Astrofizika **35**, 61 (1990).
30. V. V. Sobolev, *Moving Star Envelopes* (Leningr. Gos. Univ., Leningrad, 1947).
31. V. P. Grinin, Astrofizika **14**, 201 (1978).
32. S. I. Grachev and V. P. Grinin, Astrofizika **11**, 33 (1975).
33. G. B. Rybicki and D. G. Hummer, Astrophys. J. **219**, 654 (1978).
34. R. L. Kurucz, Astrophys. J., Suppl. Ser. **40**, 1 (1979).
35. V. P. Grinin and N. A. Katysheva, Izv. Krym. Astrofiz. Obs. **62**, 59 (1980).

36. A. Natta and B. A. Whitney, Astron. Astrophys. (2000) (in press).

37. A. Königl, Astrophys. J. **342**, 208 (1989).

38. F. Shu, J. Najita, S. Ruden, and S. Lizano, Astrophys. J. **429**, 797 (1994).

39. L. Hartmann, R. Hewett, and N. Calvet, Astrophys. J. **426**, 669 (1994).

40. L. Hartmann, S. J. Kenyon, and C. Calvet, Astrophys. J. **407**, 219 (1993).

41. T. Böhm and C. Catala, Astron. Astrophys. **290**, 167 (1994).

42. I. Appenzeller, I. Jankovics, and R. Östreicher, Astron. Astrophys. **141**, 108 (1984).

43. N. Calvet, in *Herbig–Haro and the Birth of Low Mass Stars (IAU Symposium 182*), Ed. by B. Reipurth and C. Bertout, 1997, p. 417.

44. D. Proga, J. M. Stone, and J. E. Drew, Mon. Not. R. Astron. Soc. **295**, 595 (1998).

45. A. Natta, V. P. Grinin, and V. Mannings, in *Protostars and Planets IV,* Ed. by V. Mannigs, A. P. Boss, and S. R. Russel (Univ. of Arizona Press, Tucson, 2000), p. 559.

Translated by K. Maslennikov

Astronomy Reports, Vol. 45, No. 6, 2001, pp. 452–460. Translated from Astronomicheskiĭ Zhurnal, Vol. 78, No. 6, 2001, pp. 525–534.

Roche-Lobe Overflow in the Vicinity of the Inner Lagrangian Point in Close Binary Systems

V. V. Nazarenko, L. V. Glazunova, and V. G. Karetnikov

Astronomical Observatory, Odessa State University, Odessa, Ukraine

Received January 2, 2000

Abstract—The formation of flows in the vicinity of the inner Lagrangian point has been computed for various close binary systems (from short-period U Gem to long-period β Lyr systems). The dependence of the mass-transfer rate through the inner Lagrangian point on the degree of Roche-lobe overflow is derived. One new aspect of this work is the use of Kurucz stellar model atmospheres when constructing the initial configuration of the outer layers of the mass-losing star and also the use of the "large particles" numerical method of Belotserkovskiĭ and Davydov. The application of these stellar model atmospheres provides a more realistic description of the stream than do polytropic models. The computations show that the influence of the Coriolis and centrifugal forces on the rate of mass transfer is negligible and does not exceed a few percent. In certain specific cases (β Per and W UMa), the stream models differ strongly from those of Lubow and Shu. The degree of Roche-lobe overflow and the rate of mass transfer indicated by observations are such that the atmospheric layers of the mass-losing star are nearly always located at the inner Lagrangian point. The only exceptions are compact binary systems and U Gem stars, in which the inner Lagrangian point resides in layers of the mass-losing star that are denser than its atmospheric layers, and the β Per system, in which the mass-losing atmosphere is located inside its Roche lobe. The numerical dependences of the mass-transfer rate on the degree of Roche-lobe overflow differ from the analytical dependences for both large and small overflows. This is due to differences between the Kurucz model stellar atmospheres and the polytropic models used in previous analytical calculations and also to the presence of dynamical effects connected with the mass transfer in the computations. The polytropic indices corresponding to the best agreement between the numerical and analytical dependences are 4.5 for β Lyr, 2.4–2.6 for the cataclysmic binaries, and 3.1–3.3 for the remaining stars. These polytropic indices indicate that the Roche lobes of the mass-losing stars in close binary systems are usually overflowing. *© 2001 MAIK "Nauka/Interperiodica".*

1. INTRODUCTION

Mass transfer through the inner Lagrangian point (L_1), along with the stellar wind, are the main processes resulting in the transfer of matter in close binary systems, which, accordingly, cause their evolution to deviate from that of isolated stars. Since about 90% of the stars in the Galaxy are components of binary or multiple systems, studying mass transfer in close binaries is a very important and topical problem.

The motion of flows and the formation of accretion disks in binary systems have been considered in many studies based on two- and three-dimensional numerical hydrodynamics investigating various aspects of these processes. We especially note the three-dimensional computations of Bisikalo *et al.* [1], carried out for several orbital periods on a numerical grid matched to the size of the system.

The largest drawback of these studies is their very schematic models for the stream in the vicinity of the point L_1 (often including only one or two cells) and the extremely large size of the cells in the Roche lobe of the accreting star. These conditions hinder adequate account of the effects of gas pressure on the propagation of the stream and make the initial conditions of the stream dependent on the parameters of the close binary and the degree of Roche-lobe overflow. These restrictions prevent the incorporation of gas-dynamical calculations into software used to compute the evolution of close binaries, in order to take into account the amount of matter and orbital momentum transfered from one star to the other and lost by the binary system via some parametrization. However, this mass and momentum transfer must be adequately taken into account if we wish to perform detailed calculations of binary systems at any stage of their evolution.

To close this gap, Nazarenko [2] proposed another approach, which we will develop in more detail in the present work. We consider here the first stage of mass transfer in close binaries—i.e., the formation of a stream near the point L_1—in order to obtain as complete a picture as possible of the corresponding processes in real binaries of various types and thereby determine differences in these processes in different types of close binary system.

The binary systems considered are β Lyr (an early contact binary), AO Cas (a massive semi-detached binary), β Per (a classical semi-detached binary), W UMa (a classical contact binary, assuming that the accreting star is

1063-7729/01/4506-0452$21.00

slightly smaller than its Roche lobe), and U Gem and SU UMa (short-period binaries). To compute the formation of the stream, we use a two-dimensional version of the "large-particles" method of Belotserkovskiĭ and Davydov [3]. We will construct the initial configuration of the stream using the well-established atmospheric models of Kurucz [4], which are more realistic than theoretical polytropic models.

The use of these atmospheric models provides a new and more exact approach for reconstructing the outer layers of the mass-losing star (usually the secondary), compared to the polytropic models used in the earlier computations of Paczynski and Sienkiewiez [5], Savonije [6], and Edwards and Pringle [7].

2. COMPUTATION METHOD

Only a few papers have been devoted to calculations of Roche-lobe overflow near the inner Lagrangian point. Among these, Lubow and Shu [8], Paczynski and Sienkiewiez [5], and Savonije [6] used analytical and semianalytical methods; Edwards and Pringle [7] computed the overflow at L_1 using numerical-hydrodynamics methods; and Blondin *et al.* [9] used a numerical method to study mass transfer in massive x-ray binary systems. All these papers considered the gravitational potential of the binary in a point-mass model and used polytropic models to construct the configuration of the outer layers of the mass-losing star in the vicinity of L_1 (apart from Blondin *et al.* [9], who used an isothermal atmosphere model). The centrifugal force of the orbital rotation of the binary system was taken into account in [6, 9]. Only Lubow and Shu [8] and Blondin *et al.* [9] took into account all forces influencing the motion of matter—the gravitational potential, centrifugal force, and Coriolis force.

From our point of view, the most important drawback of these earlier studies is the oversimplified initial models used for the outer layers of the mass-losing star, based on polytropic models. Lubow and Shu [8] do not consider any particular model for the mass-losing star at all, so that their calculations have a fundamental but very general character. On the other hand, the polytropic-model calculations of Paczynski and Sienkiewiez [5], Savonije [6], and Edwards and Pringle [7] are too far removed from real binary systems and it is difficult to trace the dependence of the final results on the binary parameters. The absence of Coriolis and centrifugal forces in these models does not appreciably affect the final results, as will be seen from our own calculation results presented below.

To simulate the formation of the stream more accurately than in these previous studies, we use the atmospheric models of Kurucz [4] to construct the initial configuration of the outer layers of the mass-losing star. As a result, our computations directly depend on the parameters of the binary system, since the atmospheric models are directly specified by the gravitational acceleration and temperature adopted for the specific star.

One very important feature of our calculations is that we do not use any special mechanisms to generate the process of mass transfer in the vicinity of L_1. In contrast to the single numerical work dealing with this issue, by Edwards and Pringle [7], we simply continue the computational region to the Roche lobe of the main component, where the pressure gradient and gravitational force are in the same direction, making hydrostatic equilibrium impossible. The gas accelerated in this region forms a stream in the vicinity of the inner Lagrangian point, clearly visible in our calculations. The gas penetrates to the Roche lobe of the primary due to the evolutionary expansion of the companion in the close binary. The degree of overflow of the Roche lobe by the companion is treated as a free parameter. Therefore, we concentrate on the hydrodynamical aspects of Roche-lobe overflow, without considering the evolutionary origins of this effect.

We use a standard model for the binary systems; i.e., the stars are taken to be gravitational point masses, the orbits of the binary systems are assumed to be circular, and the mass-losing star rotates about its axis in synchrony with its rotation about the common center of mass of the system. We assume that the gas is ideal and, for the sake of simplicity, composed purely of hydrogen. The specific heat capacity is taken to be close to unity (about 1.01–1.10); this is an implicit way to take into account the probable effects of interactions between the moving gas and radiation. This method is quite standard and was already applied, for example, by Molteni *et al.* [10] and Bisikalo *et al.* [1].

We solved the nonstationary Euler equations using the explicit "large-particle" method of Belotserkovskiĭ and Davydov [3], which has first-order accuracy in space and second-order accuracy in time. The advantages of this method include its simplicity and high stability, making it possible to use it to solve problems in nonstationary hydrodynamics on personal computers. We carried out the computations in two planes—the orbital plane and the plane perpendicular to it—to obtain at least some approximation of the three-dimensional gas-flow pattern. The computations were conducted from the initial to the final steady state, when all the gas-flow parameters were nearly independent of time over the entire computational region. In practice, a time interval of from one to three orbital periods of the close binary system was required to achieve this state.

3. THE INITIAL MODEL AND BOUNDARY CONDITIONS

We carried out the calculations in a rectangular coordinate grid whose origin was at the center of the mass-losing star (i.e., the secondary, or companion). This choice of coordinate system is possible due to the relatively small size of the region of the binary system

considered, covering only the vicinity of the point L_1, whose size does not exceed 0.1. (Here and below, we give all distances in the binary systems in units of the distance between the stellar centers.)

As already noted above, our use of model stellar atmospheres enables us to consider more realistic matter flows, compared to previous studies based on polytropic models. On the one hand, the atmospheric models themselves provide more accurate approximations of the outer layers of the stars than polytropic models. In addition, the direct dependence of the atmospheric models on the parameters of the binary systems (such as the orbital separation, the component masses, and the effective temperature of the contact component) enables us to take into account specific features of the mass transfer in different types of close binary systems.

The atlas of Kurucz [4] is the best known atlas of stellar atmospheres and covers a very wide range of variations in the parameters in the models: $\log g$ varies from 0.1 to 4.0, and the effective temperature varies from 4000 to 50000 K. These wide ranges of the model parameters enable calculation of the formation of the stream for almost any type of binary systems.

To choose the atmospheric model used for a computation, we specify two parameters—the effective temperature of the companion and the mean gravitational acceleration at its surface when such a star is not in a binary system $g_{\rm mean} = G*M_{\rm cont}/R^2_{\rm cont}$, where G is the gravitational constant, and $M_{\rm cont}$ and $R_{\rm cont}$ are the mass and mean radius of the contact component (mass-losing star). We derive a two-dimensional model for the outer layers of the contact component in the vicinity of L_1 assuming a barotropic condition for the mass-losing star (corresponding to its own rotation being in synchrony with its motion about the common center of mass of the binary); i.e., we assume that the contours of equal pressure coincide with the equal-potential contours for the common field of the binary. To satisfy this condition, we must first determine the cell sizes along the x and y axes from the equation of hydrostatic equilibrium. In this way, we specify a numerical grid whose main advantage is that it is calculated taking into account the specific features of each close binary, rather than being chosen arbitrarily.

As we will show below, the average size of the cells in this grid depends appreciably on the parameters of the binary system. Note also that the resulting numerical grid is not uniform: the cell dimensions decrease far from the central line and increase along the central line (x axis) outward, toward the Roche lobe of the main component. This nonuniformity of the numerical grid enables us to allow for rapid variations in physical quantities at the boundaries of the computational region with higher accuracy.

Taking into consideration the atmospheric model and cell sizes, we obtain a one-dimensional model for the outer atmospheric layers of the mass-losing star along the central line. To extend this model to the entire computational region, we approximate the dependences of the matter density $N(F)$ and temperature $T(F)$ along the central line by cubic splines (in the same manner as Edwards and Pringle [7]). Next, using these dependences, we can easily extend our one-dimensional model to the entire computational region. Thus, we obtain a pattern intermediate between a stream and the usual atmosphere of an isolated star.

The variation in the matter density in such an atmosphere still corresponds to the atmosphere of an isolated star, whereas the size of the atmosphere corresponds to the situation when the star is in a binary system, since the atmosphere is situated near the inner Lagrangian point. (When calculating the cell sizes using the condition of hydrostatic equilibrium, we take into account all forces acting in the binary, apart from the Coriolis force.)

We formulate the boundary conditions so that free gas outflow is allowed through the boundaries of the computational region. The conditions at boundary A (Fig. 1) are specified so that the corresponding velocity is close to zero and the physical quantities are almost constant over the entire computation. This is a quite important condition, since it is precisely this condition that is responsible for the character of the gas flow. The parameters of the flow at boundaries O and R are determined by the parameters of the flow from neighboring cells using extrapolation formulas.

We should specifically note the position of boundary O. In contrast to the analysis of Edwards and Pringle [7], where the boundary O passed through L_1, in our calculations, this boundary is located in the Roche lobe of the main component, so that the flow can be freely formed by the action of the force fields intrinsic to the problem, without imposing any extra conditions. (In other words, there are no other conditions specifying the pressure gradient or pressure at L_1 which give rise to the gas flow in the vicinity of the inner Lagrangian point.) We also emphasize that it thus becomes to some degree meaningless to ask whether the gas from the mass-losing star in the Roche lobe or at its boundary can overcome the potential barrier and enter the Roche lobe of the main, compact component. The gas overcomes this potential barrier due to the evolutionary expansion of the mass-losing star or the evolutionary decrease in the dimensions of its Roche lobe.

4. CALCULATION OF ROCHE-LOBE OVERFLOW AND FORMATION OF A STREAM AT THE INNER LAGRANGIAN POINT

We studied the formation of streams in binary systems characterized by very different physical and geometrical parameters. As a result, we can obtain a relatively comprehensive picture of Roche-lobe overflow in real close binary systems. The parameters of the binaries in our computations are listed in Table 1, which

gives (1) the name of the binary system, (2) the orbital period in days, (3) the orbital separation in solar radii, (4) the mass of the main component (expressed, as are all masses, in solar masses), (5) the mass of the companion (i.e., mass-losing star), (6) the effective temperature of the mass-losing star, and (7) the mass-transfer rate through the inner Lagrangian point in units of solar masses per year indicated by observations.

For each close binary system, we calculated the complete outflow pattern—from the minimum case, when the entire atmosphere of the mass-losing component is within its Roche lobe, to the maximum, when the entire atmosphere is outside the Roche lobe. The dimensions of the numerical grid changed in the course of the calculations from 200×200 to 200×500, with the mean number of cells equal to 60000. To take into account the influence of the numerical grid on the solutions obtained, we varied the number and thereby the dimension of the cells. (We used an atmospheric model composed of 200 layers rather than the usual 100 layers.) Since the computational results remained almost the same, we can assume that the numerical grid does not appreciably affect the solutions obtained.

It is quite interesting to compare the patterns of stream formation at the inner Lagrangian point obtained by Edwards and Pringle [7] with our results. To this end, we computed the formation of a stream in the binary SU UMa using a polytropic model, as in [7], and compared our radial distribution of mass density at L_1 with the same distribution from [7]. The results of this comparison are shown in Fig. 2. Taking into account the differences in the initial models, boundary conditions, and numerical methods used, the results of the two computations are in quite good agreement.

Since we have also taken into account the Coriolis and centrifugal forces in our calculations, we can study their influence on the stream formation and, especially, on the mass-transfer rate through L_1. The computations indicate that these forces have almost no affect on the formation of the stream, even in the cases of a high mass-transfer rate at L_1 of about 40 km/s (the Coriolis force in β Lyr) or of small mass ratios of about 0.1 (the centrifugal force in the SU UMa system). The effects of the Coriolis and centrifugal forces on the mass-transfer rate through the inner Lagrangian point are likewise not significant and have no observable consequences. Therefore, we conclude that the neglect of these forces in some previous studies does not represent a significant drawback of those calculations.

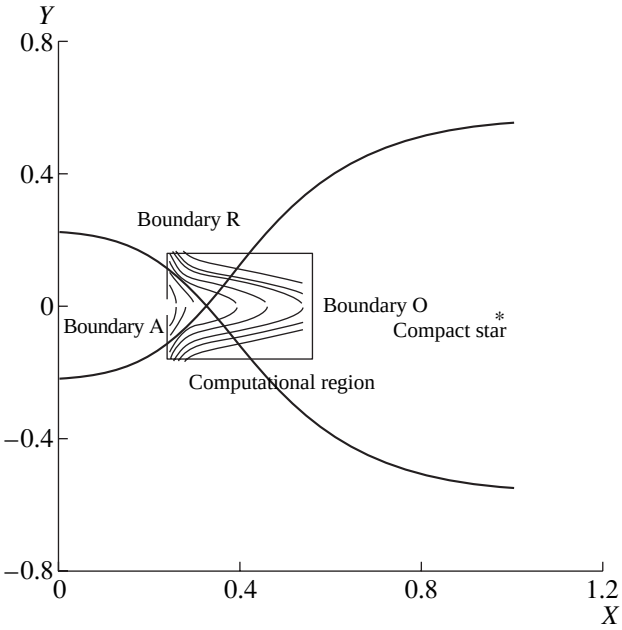

Fig. 1. Initial configuration of the atmosphere of the subgiant in the β Lyr system in the vicinity of the inner Lagrangian point L_1.

We also compared our results with the model of Lubow and Shu [8]. For all the binary systems (including the long-period ones), the velocity of the gas stream at L_1 is approximately equal to the local sound speed and the radial distribution of matter is consistent with a Gaussian distribution with $\sigma = R_{\text{stream}}/(3–4)$ to an accuracy of 10–15%, where R_{stream} is the stream radius, determined from the condition used by Edwards and Pringle [7] (namely, the stream radius is specified by the cylinder containing 99% of the entire mass flow). On the other hand, the stream radii calculated using the relation given by Lubow and Shu [8] sometimes differ from those obtained in the numerical calculations by

Table 1

Name of the system	Period, days	Orbital separation, $R_\odot$	M_{main}, $M_\odot$	M_{comp}, $M_\odot$	T_{eff}, K	Mass-loss rate, $M_\odot$/yr
β Lyr	13.00	55	12	2.0	11000	1.2×10^{-5}
β Per	2.87	14	3.4	0.7	6000	1.0×10^{-11}
AO Cas	3.50	33	23	17.0	39000	1.0×10^{-7}
W UMa	0.46	2.4	0.6	1.2	6000	1.0×10^{-8}
U Gem	0.03	0.5	0.5	0.5	4000	$10^{-10} – 10^{-9}$
SU UMa	0.12	1.3	1.0	0.6	4220	1.0×10^{-11}

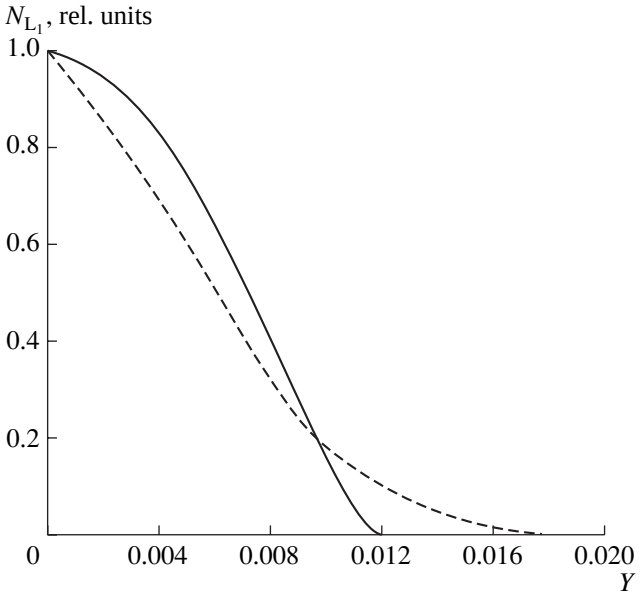

Fig. 2. Comparison of the radial distribution of the mass density at L_1 (dashed line) computed for the formation of the stream in the binary SU UMa using a polytropic model (as in [7]) with (solid line) the corresponding distribution from [7].

factors of two to three, as, for example, in the cases of W UMa and β Per (Table 2).

Another effect clearly visible in our computations is variations in the structure of the mass-losing component due to the mass transfer near the inner Lagrangian point. In the case of minimal degrees of overflow, when the pressure gradients in the atmosphere are fairly large, the density and temperature at L_1 increase over their initial values in the stationary solution; in the case of a large overflow, when the entire atmosphere is outside the Roche lobe, the density and temperature decrease in the stationary solution.

This effect, which can be called dynamical, leads to variations of the structure of the contact component compared to the atmosphere of the corresponding isolated star, which should be manifest in the dependence of the mass-transfer rate on the degree of Roche-lobe overflow. Since this dynamical effect could not be taken into account in the analytical formulas of Paczynski and Sienkiewiez [5] and Savonije [6] (which ignore the motion of matter in the vicinity of L_1), our numerical dependences should be different from the analytical formulas, as we will show in the next section.

The basic result of our computations are the structures of the streams in the close binary systems considered. Since we are interested in realistic descriptions of the mass transfer in such systems, we shall consider stream structures for which the computed mass-transfer rates are in agreement with the rates derived from observations.

The flow parameters at L_1 are presented in Table 2. The columns of this table give (1) the name of the system, (2) the density of matter N_{L1} at the point L_1, (3) the temperature at L_1, (4) the gas velocity U_{L1} at L_1, (5) the local sound speed V_{L1} at the inner Lagrangian point, (6) the calculated stream radius in units of the orbital separation, (7) the stream radius derived from the formula presented by Lubow and Shu [8] (i.e., the ratio of the local sound speed to the orbital velocity of the binary) expressed in the same units, and (8) the mass-transfer rate obtained in our calculations in solar masses per year.

As expected, due to variations in the physical conditions of the close binary systems, the stream parameters in the binaries considered differ appreciably. These differences are most pronounced for the stream radius, which varies in a wide range from 0.012 (for cataclysmic variables) to 0.13 (for β Lyr and the early-type contact systems), in units of the orbital separation. The particle density and temperature in the stream also vary appreciably, over the ranges 10^{12}–10^{17} cm^{-3} and 3000–50000 K, respectively. This is the result of variations in the physical parameters of the close binary systems and their evolutionary statuses (i.e., degrees of overflow). Therefore, there is no universal structure for the streams in close binaries, which are characterized by considerable variety over the entire spectrum from long-period to short-period systems.

Table 2

Name of the system	N_{L1}, cm^{-3}	T_{L1}, K	U_{L1}, km/s	V_{L1}, km/s	R_{L1}, A	R_{L1}^{LS}, Å	Mass-loss rate, $M_\odot$/yr
β Lyr	1.0×10^{15}	79097	43.7	33.0	0.130	0.150	1.2×10^{-5}
AO Cas	9.2×10^{14}	55043	34.8	28.1	0.056	0.059	4.0×10^{-7}
β Per	1.7×10^{12}	2439	6.4	5.9	0.045	0.024	2.6×10^{-11}
W UMa	8.4×10^{16}	14174	12.4	14.3	0.016	0.054	1.2×10^{-8}
U Gem	8.0×10^{16}	13919	9.8	14.2	0.013	0.021	1.2×10^{-9}
SU UMa	2.4×10^{16}	6800	5.3	9.9	0.015	0.019	2.7×10^{-10}

One new result obtained in our calculations is the degrees of Roche-lobe overflow of the contact components, which correspond to the mass-transfer rates derived from observations. The degree of overflow can be expressed numerically in one of two ways. The first uses the standard expression, defined as $\Delta r/r^*$, where Δr is the difference between the mean radii of the contact component and of its Roche lobe and r^* is the mean radius of the contact component. The second way is to express the overflow in units of the total atmospheric overflow (i.e., when the entire atmosphere of the contact component is outside its Roche lobe.)

These two degrees of overflow are equal to 2.4, 0.1 for β Lyr and 2.5, 0.04 for W UMa (both contact binaries); 0.5, 0.06 for AO Cas and –0.4, 0.009 for β Per (semi-detached systems); 0.3, 0.0010 for SU UMa and 100.7, 0.0015 for U Gem (cataclysmic systems). Here, the first quantities are expressed in units of the total atmospheric overflow and the second quantities, in the standard units.

We can see that, for all the binaries apart from the contact systems and U Gem, the atmospheric layers are located at L_1; i.e., atmospheric overflow is realized. The high degree of overflow for U Gem in atmospheric units stands out. This seems to be associated with physical processes occurring in this system. The negative degree of overflow for β Per indicates that the entire atmosphere of the mass-losing star in this system is located inside its Roche lobe, and the upper chromospheric or coronal layers are located at the inner Lagrangian point.

5. COMPARISON OF THE DEPENDENCES OF THE MASS-TRANSFER RATE ON THE DEGREE OF ROCHE-LOBE OVERFLOW BY THE CONTACT COMPONENT

Computation of the dependence of the mass-transfer rate at the inner Lagrangian point on the degree of Roche-lobe overflow is the most interesting application of gas-dynamical studies of mass transfer in the vicinity of L_1 from the viewpoint of the evolution of binary systems. To study this in detail, we calculated the corresponding dependences for the following grid of parameters of the close binary systems: orbital separations of 2×10^{12}, 3×10^{11}, and 3×10^{10} cm; effective temperatures of 4000, 6000, 8000, 10000, 25000, and 40000 K; mass ratios of 0.1, 0.3, 0,5, and 1.0; and the total masses of both components are 4 and $20M_\odot$. As noted above, the degree of overflow was treated as a free parameter and the physical origins for the Roche-lobe overflow were not considered. All parameters of the binary were assumed to remain constant during the course of the computations.

First, we looked for differences between our results and the analogous analytical calculations of Paczynski and Sienkiewiez [5] and Savonije [6], since the "analytical" overflows agree well with the numerical results of Edwards and Pringle [7]. There are two possible origins for such differences: the different models for the outer layers or the influence of dynamical effects in the mass transfer. To compare the analytical and numerical methods, we calculated the analytical dependences with the polytropic indices that gave the best coincidence between the numerical and analytical results.

To illustrate this comparison between the numerical and analytical dependences, we calculated the overflows for three well-known close binaries—β Lyr, SU UMa, and U Gem. We took the parameters of these systems from Tables 4 and 5 of Savonije [6]. For the first set of parameters from Table 4 in [6], the period of the binary system is $P_0 = 1^d$, the mass of the contact component is $4M_\odot$, the mass of the main component is $1.5M_\odot$, the effective temperature is $\log T_{\rm eff} = 4.2243$, and the polytropic index is 3.273. For the second set of parameters from Table 5 of [6], the period of the binary system is $P_0 = 2.09^d$, the mass of the contact component is $16M_\odot$, the mass of the main component is $1M_\odot$, the effective temperature is $\log T_{\rm eff} = 4.4013$, and the polytropic index is 3.220.

The results of these calculations are presented in Fig. 3, which shows the initial numerical dependences (where the matter velocity was taken to be equal to the local sound speed), the numerical dependences for the stationary solution, and the analytical dependences of Paczynski and Sienkiewiez [5] and Savonije [6] for various sets of close-binary parameters. Comparison of the numerical and analytical dependences in all the figures shows that the numerical dependences are in better agreement with the analytical formulas of Savonije [6], whereas the agreement with the formulas of Paczynski and Sienkiewiez [5] is considerably worse (except for β Lyr, where the opposite is true).

This could be due to the fact that, in both our computations and in [6], the photospheric density at the outer boundary is not zero, and the mass-transfer rate is not zero in the case of zero overflow. As a result, the analytic dependence turns out to be similar to our numerical dependence. On the other hand, when the densities at the outer boundary of the atmosphere are very small (about 10^9 cm^{-3}), the mass-transfer rate will be very close to zero and the distribution of Paczynski and Sienkiewiez [5] will be in better agreement with the numerical dependence (as occurs, for example, in β Lyr). Therefore, using the atmospheric models of Kurucz [4], we conclude that the formula of Savonije [6] is in better agreement with the numerical dependences when the effective temperatures of the mass-losing stars are less than 10000–12000 K, while the formula of Paczynski and Sienkiewiez [5] is in better agreement for higher effective temperatures.

Comparison of the numerical initial dependence and the dependence for the stationary solution shows the role of dynamical effects in the outflow of matter on the formation of the stream and the mass-transfer rate for various degrees of Roche-lobe overflow. As follows

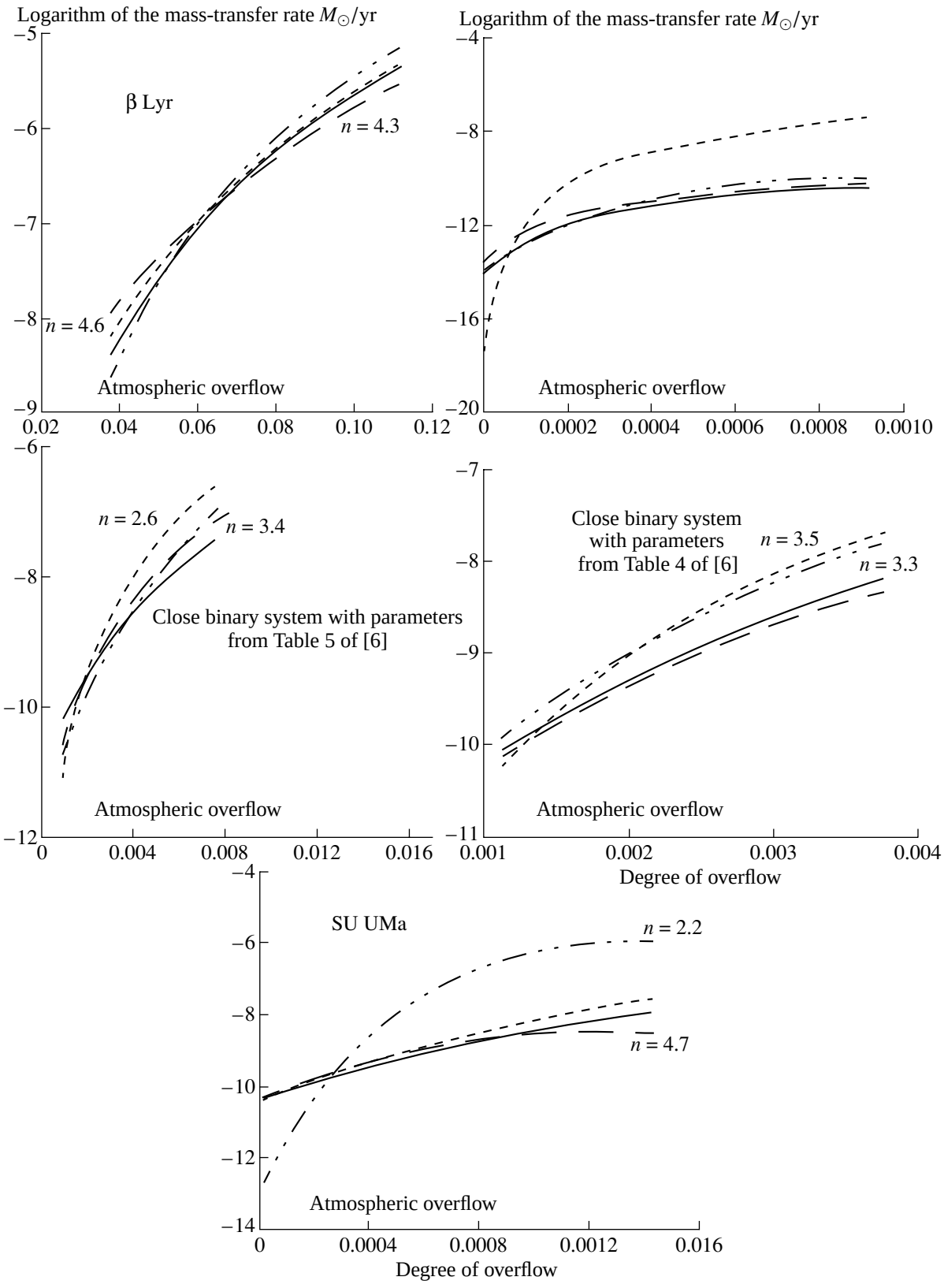

Fig. 3. Dependence of the mass-transfer rate on the degree of Roche-lobe overflow by the contact component for various close binary systems. Shown are the initial numerical dependence (dotted curve), the numerical dependence corresponding to the stationary solution (solid curve), the analytical dependence according to Paczynski and Sienkiewiez [5] (short-dashed curve), and the analytical dependence according to Savonije [6] (long-dashed curve). The adiabatic indices are given near the curves.

from Fig. 3, these two dependences often coincide at moderate degrees of overflow, the initial numerical dependence is usually below the numerical stationary dependence at small degrees of overflow, and the opposite is true at large degrees of overflow. Therefore, we can clearly see the influence of dynamical effects on variations in the mass-transfer rate. At small degrees of Roche-lobe overflow, these effects lead to a slight increase in the mass-transfer rate under the action of the moving gas (by approximately half an order of magnitude), compared to the initial values (where, as noted above, the local sound speed was used in the calculations instead of the gas velocity); at large degrees of Roche-lobe overflow, the mass-transfer rate decreases compared to its initial value.

Such dynamical effects are associated with the behavior of the density gradient near the inner Lagrangian point in various atmospheric layers. The density gradient in the outer atmospheric layers is fairly large (especially in stars with effective temperatures above 10000–12000 K) and is considerably higher than required for the stationary solution. At the initial time, matter is transferred from inner (denser) layers to the inner Lagrangian point under the action of the large density gradient. As a result, the density at L_1 increases and the density gradient correspondingly decreases. The mass-transfer rate also decreases compared to its initial value. On the other hand, in the case of moderate overflow, dynamical effects are often absent, since the initial density gradient in the vicinity of L_1 nearly coincides with the stationary value. Finally, the situation is opposite in the case of large overflow: the initial density gradient is less than required for the stationary solution. As a result, the density at L_1 decreases compared to its initial value and the density gradient increases, so that the mass-transfer rate for the stationary solution turns out to be less than at the initial time. Therefore, the role of dynamical effects in our calculations can be traced fairly clearly. These effects lead to considerable variations in the mass-transfer rate for the stationary regime, especially in the case of large overflows, when the entire atmosphere is located outside the Roche lobe of the mass-losing star (sometimes, by over half an order of magnitude, as can be seen in Fig. 3).

We should also point out the polytropic indices for the analytic dependences that are in the best agreement with the numerical dependences (Fig. 3). These polytropic indices are 4.6 and 4.3 in the model of Savonije [6] for β Lyr; 2.2 in the model of Paczynski and Sienkiewiez [5] and 2.8 in the model of [6] for SU UMa; 2.6 in the model of [5] and 3.4 in the model of [6] for U Gem; 3.2 in the model of [5] and 2.7 in the model of [6, Table 4]; and 3.5 in the model of [5] and 3.3 in the model of [6, Table 5].

All these polytropic indices are close to three and, therefore, correspond to atmospheric overflow at the inner Lagrangian point. Indeed, as was shown by our calculations, the atmospheric layers are located at L_1 in almost all cases. This suggests that there is good consistency between the numerical and analytical calculations when the numerical calculations are based on the atmospheric models and the analytical polytropic indices are close to three. In this case, the greater or smaller the extent of the atmosphere (or the greater or smaller the effective temperature), the more the polytropic index will be greater or smaller than three. The binary system β Lyr possesses the most extensive atmosphere, and the corresponding polytropic index takes on its greatest value (>4.5).

6. CONCLUSIONS

We obtained the following main results in the course of the present study.

(1) We have developed a numerical algorithm enabling more accurate calculation of the stream structure near the inner Lagrangian point, compared to previous methods. This algorithm uses the atmospheric models of Kurucz [4]. The direct dependence of the stellar-atmosphere models on the stellar parameters makes it possible to take into account the characteristic features of the mass transfer in each type of close binary system.

(2) The models for streams of matter in close binary systems obtained using our method show that, in some cases, the stream radius differs from that calculated in the model of Lubow and Shu [8] by factors of two to three.

(3) The concentrations and temperatures of the gas at the point L_1 for models for which the mass-loss rates are equal to those derived from observations lie in the ranges 10^{12}–10^{17} cm^{-3} and 3000–50000 K, respectively.

(4) Applying the numerical method to analyses of various close binary systems enabled us to estimate the degrees of overflow at L_1 at the current time. These overflows vary from 0.1 (for β Lyr) to 0.001 (for U Gem).

(5) A comparison of the numerical dependences for the mass-transfer rate on the degree of overflow and the analytical dependences of Paczynski and Sienkiewiez [5] and Savonije [6] showed that the numerical dependences are in a good agreement with the calculations of [6] when the effective temperature of the mass-losing star is less than 10000–12000 K. When the effective temperatures are higher than 12000 K, the numerical dependences are in good agreement with the model of [5].

In conclusion, we recommend the use of different analytical formulas in the case of different effective temperatures for the components in close binary systems being studied. Since the analytical dependences sometimes differ considerably from the numerical dependences, the derivation of exact dependences requires the use of hydrodynamical computations incorporating model atmospheres for the stars in the close binary systems.

REFERENCES

1. D. V. Bisikalo, A. A. Boyarchuk, V. M. Chechetkin, *et al.*, Mon. Not. R. Astron. Soc. **300**, 39 (1998).
2. V. V. Nazarenko, Astron. Zh. **70**, 12 (1993) [Astron. Rep. **37**, 55 (1993)].
3. O. M. Belotserkovskiĭ and Yu. M. Davydov, *Large Particles in Gas Dynamics* (Nauka, Moscow, 1982).
4. R. L. Kurucz, Astrophys. J., Suppl. Ser. **40**, 1 (1979).
5. B. Paczynski and R. Sienkiewiez, Acta Astron. **222**, 73 (1972).
6. G. J. Savonije, Astron. Astrophys. **62**, 317 (1978).
7. D. A. Edwards and J. E. Pringle, Mon. Not. R. Astron. Soc. **229**, 383 (1987).
8. S. H. Lubow and F. H. Shu, Astrophys. J. **198**, 383 (1975).
9. J. M. Blondin, I. R. Stevens, and T. R. Kallman, Astrophys. J. **371**, 684 (1991).
10. D. Molteni, G. Belvedere, and G. Lanzafame, Mon. Not. R. Astron. Soc. **249**, 748 (1991).

Translated by Yu. Dumin

Astronomy Reports, Vol. 45, No. 6, 2001, pp. 461–466. Translated from Astronomicheskiĭ Zhurnal, Vol. 78, No. 6, 2001, pp. 535–540.

The Dust Envelope of the Symbiotic Nova V1016 Cyg

M. B. Bogdanov[1] and O. G. Taranova[2]

[1]*Chernyshevskiĭ State University, ul. Universitetskaya 42, Saratov, 410601 Russia*
[2]*Sternberg Astronomical Institute, Universitetskiĭ pr. 13, Moscow, 119899 Russia*

Received August 3, 2000

Abstract—Brightness and color variations of V1016 Cyg are studied using many years of *UBVRJHKLM* photometric observations and information about its spectral energy distribution in the intermediate IR (7.7 to 22.7 μm) obtained with the IRAS and ISO low-resolution spectrometers. Models for its stationary, spherically symmetrical, extended dust envelope are computed for two cases of heating: by the radiation of the cool component only and by the combined radiation from both components. Model fitting of the IRAS and ISO observations shows that the model with a single central source—the Mira star—provides a better fit to the data, indicating that the hot component's radiation is appreciably reprocessed by the ambient gas medium and has almost no direct influence on the IR spectrum of the symbiotic nova. The mean spectral energy distributions measured by IRAS in 1983 and ISO on October 1, 1996, differ considerably. The observed evolution of the envelope's spectrum probably reflects an increasing grain concentration and decreasing grain temperature at the inner edge of the envelope, associated with decreased luminosity and increased temperature of the hot component. The total mass-loss rate, gas-expansion velocity at the outer edge of the envelope, and upper limit to the mass of the central radiation source are estimated. © *2001 MAIK "Nauka/Interperiodica".*

1. INTRODUCTION

The preoutburst spectrum of the symbiotic nova V1016 Cyg was typical of long-period variables, with TiO, VO, and CO absorption bands in the optical and IR. After the outburst, the star acquired a well-developed, high-excitation emission spectrum with forbidden lines. This transformation of the spectrum requires the presence of a hot component in the system and the existence of a circumstellar envelope. Mass loss by the red giant could be a source of material for the gaseous nebula (observed as a radio source), as well as for the dust envelope, which radiates in the IR. After the 1964 optical outburst of V1016 Cyg [1], when the object's V brightness increased by almost 5^m, extensive observations of the star were initiated in all accessible parts of the spectrum.

The peculiar object V1016 Cyg is now attributed to a small subclass of symbiotic stars and is classified as a very slow type D symbiotic nova (with appreciable radiation from the dust envelope in the near IR). The system's cool component is a Mira variable with periodic pulsations of its IR brightness [2, 3]; the hot component, which experienced the 1964 outburst, is a white dwarf. After the hot source's outburst, its UV radiation began to evaporate and dissipate the dust envelope, and, since the late 1970s, near-IR radiation from the Mira has been clearly detected (1.25 to 2.5 μm) in the spectrum of V1016 Cyg. Symbiotic novae like V1016 Cyg remain in quiescence for a long time then experience a single major outburst in their photometric histories. Polarimetric observations of V1016 Cyg [4] indicate that this binary's orbital period could be as long as 60 to 100 yrs.

High-spatial-resolution observations revealed a bipolar structure in the V1016 Cyg system characteristic of many planetary nebulae. The variability of the Mira superposed on the slow brightness changes of the gaseous envelope and dust density variations associated with the variable luminosity and effective temperature of the hot component makes the observed flux changes for V1016 Cyg rather complicated.

The current paper analyzes brightness and color variations of the symbiotic nova V1016 Cyg based on our optical and IR photometric data acquired from 1978 to May 2000, together with IR observations from the IRAS satellite and the ISO orbiting observatory. We also compute a model for the system's dust envelope and estimate the parameters of the stellar wind.

2. OBSERVATIONS

Our optical and IR photometry of V1016 Cyg was carried out with the 1.25-m telescope of the Crimean Laboratory, Sternberg Astronomical Institute, starting in 1978, as part of a program to study circumstellar dust envelopes. The photometric standards were the stars BS 7784 (for the *UBVR* observations) and BS 7796 (for the IR photometry). The angular diameter of the exit diaphragm of the photometer was about 12″; during modulation, the beams were separated by ~30″ in the East–West direction. The uncertainties of the optical and *JHKL* brightness estimates were no more than $0^m.03$; those for the M filter were no more than $0^m.05$.

1063-7729/01/4506-0461$21.00 © 2001 MAIK "Nauka/Interperiodica"

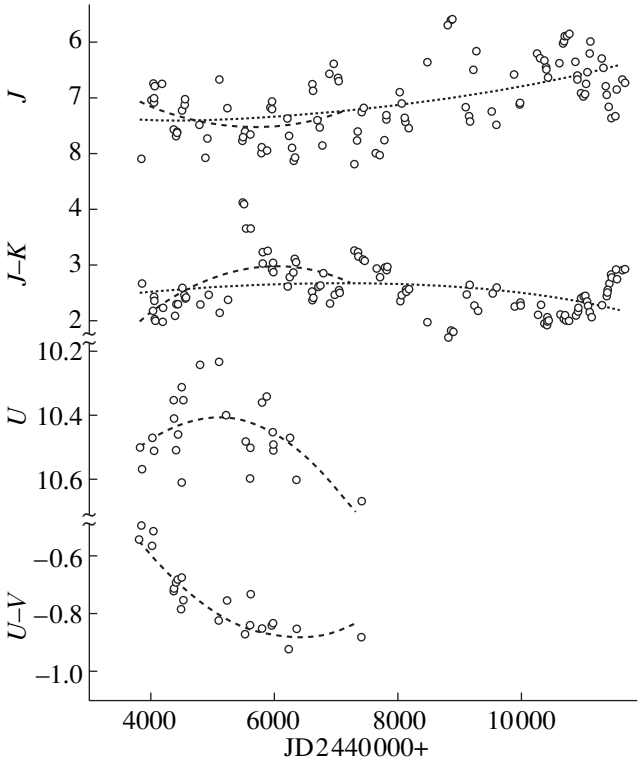

Fig. 1. Variations of the brightness and color indices of V1016 Cyg in the optical and IR, 1978–2000 (circles). The dotted and dashed curves represent parabolic approximations to the observations.

Our observed *U* and *J* magnitudes and (*J*–*K*) and (*U*–*V*) color indices for V1016 Cyg are plotted as circles in Fig. 1. Figure 2 displays the changes of these same quantities with phase. The variability phases were computed for the Mira pulsation period P = 470^d, adopting the initial epoch JD 2440000. The results of our *JHKLM* photometry of V1016 Cyg are discussed in more detail in [5]. In our corrections for interstellar absorption, we used the value $E(B–V) = 0.25^m$ [6].

3. ANALYSIS OF BRIGHTNESS AND COLOR VARIATIONS

The dashed and dotted curves in Fig. 1 show parabolic approximations to our observations of V1016 Cyg. The dashed curves correspond to 1978–1988, when we obtained simultaneous optical and IR observations. Figure 1 shows that the *J* brightness (like *HKLM*) monotonically increased from the beginning of our observations in 1978 until May 2000. During these changes of the IR brightness, the system became bluer in the IR (on average, *J*–*K* decreased). The observed smooth changes of the IR brightness and color of V1016 Cyg were explained in [5] as an effect of changes of the optical depth of the dust envelope, which had decreased somewhat by May 2000 compared to the beginning of our observations in 1978.

As for the symbiotic nova HM Sge, we can see changes in the brightness and color of V1016 Cyg at opposite phases in the optical and IR in 1978–1988, when we had simultaneous optical and IR observations (Fig. 1). The visual radiation of V1016 Cyg after its outburst is almost completely formed in the ionized gaseous envelope, and the observed brightness and color variations are due to changes in this envelope's parameters. In 1978–1983, the *U*-band brightness increased, whereas *U*–*V* decreased. This suggests that

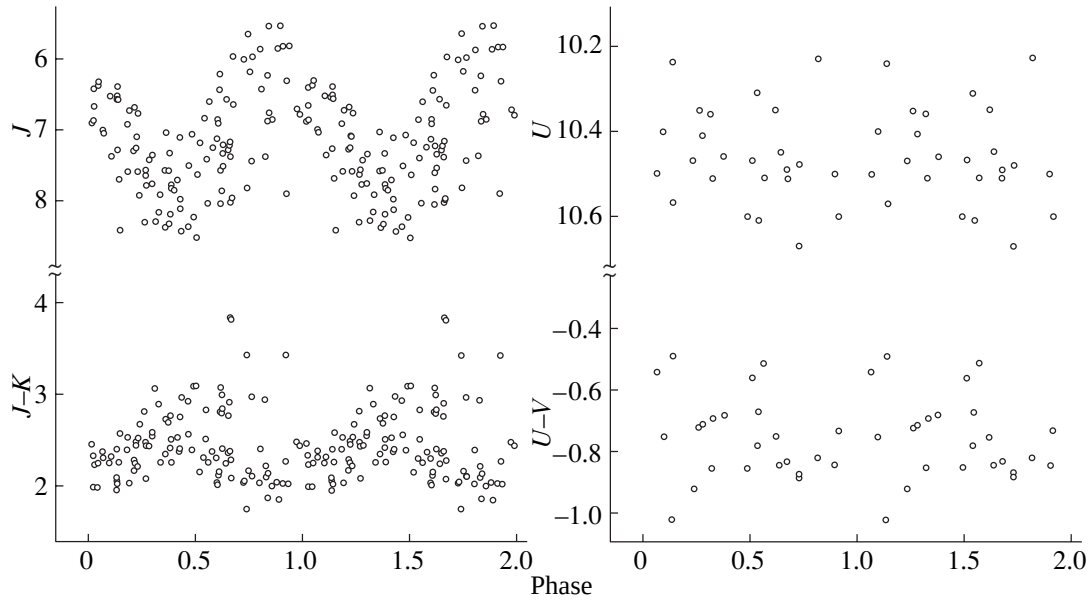

Fig. 2. 1978–1999 photometry of V1016 Cyg folded with the 470^d period for the brightness variations of the Mira star (the initial epoch is JD 2440000).

the density of the ionized envelope was increasing during that period. In 1983, the density achieved its maximum value, after which the ionized gaseous envelope apparently began to expand, giving rise to a smooth decrease in the *U*-band flux and in *U–V* in 1983–1988 (Fig. 1). Thus, the densities of the dust and gas components of the envelope simultaneously decreased in 1983–1988, probably due to expansion.

Figure 2, which presents phase light and color curves for the 470^d period, shows changes in the IR that are typical of Mira variables: from maximum to minimum brightness, for example in the *J* band, the Mira becomes cooler (*J–K* increases towards minimum brightness).

4. MODEL COMPUTATIONS FOR THE DUST ENVELOPE OF V1016 CYG

The problems encountered in computations of dust-envelope models for symbiotic novae were discussed by us in detail in [7], where we analyzed observations of HM Sge [7]. The main difficulty is the presence of two sources heating the envelope, with comparable luminosities but quite different temperatures. The characteristic emission peaks of silicates in the IR spectrum of V1016 Cyg, typical of oxygen Miras, provide evidence that the cool component is the main supplier of dust in the system. However, there is no doubt that the hot component's radiation and stellar wind should influence the heat balance and grain dynamics. The existence of this component, whose hard radiation is largely reprocessed by the ambient gas, leads to uncertainty in the resulting spectrum of the radiation heating the dust and violates the spherical symmetry of the envelope.

Bryan and Kwok [8] noted that the expected distance between the components of symbiotic novae (~10 to 100 AU) was much smaller than the size of their envelopes (~1 pc), making it possible to take the stars to be at the center of their envelope and the envelope itself to be spherically symmetrical. In the case of V1016, this is confirmed by observations. The rotation of the plane of polarization detected by Schild and Schmid [9] yields an estimate for the orbital period of 80 ± 25 years. For a total mass of the components of $2M_\odot$, the 80-year period corresponds to an orbital semi-major axis of 3.5×10^{14} cm (23 AU). For a Mira with the luminosity and effective temperature corresponding to a variability period of 470^d, the condensation of silicates should occur at approximately this distance. Thus, we can consider both components of V1016 Cyg to be situated within the inner edge of the dust envelope.

Taking into account uncertainties due to the spectrum of the hot component reprocessed by the ambient gas, we computed, as we had for HM Sge [7], models for the stationary, spherically symmetrical gaseous envelope of V1016 Cyg for two cases of heating: by radiation only from the cool component (hereafter, model 1) and by the combined radiation from both components, not taking into account the absorption of high-energy photons by the gaseous medium (model 2). To choose the model parameters, we again limited our consideration to the spectral energy distribution in the intermediate IR, 7.7 to 22.7 μm, measured by the spectrometers of the IRAS satellite and ISO orbiting observatory. We retrieved the $F(\lambda)$ values from the Internet, from the databases of the University of Calgary and the ISO observatory. The IRAS observations were reduced using the calibration from [10]. The $\lambda F(\lambda)$ values (in erg s^{-1} cm^{-2}) are plotted as a function of wavelength λ (in μm) as circles in Figs. 3 and 4.

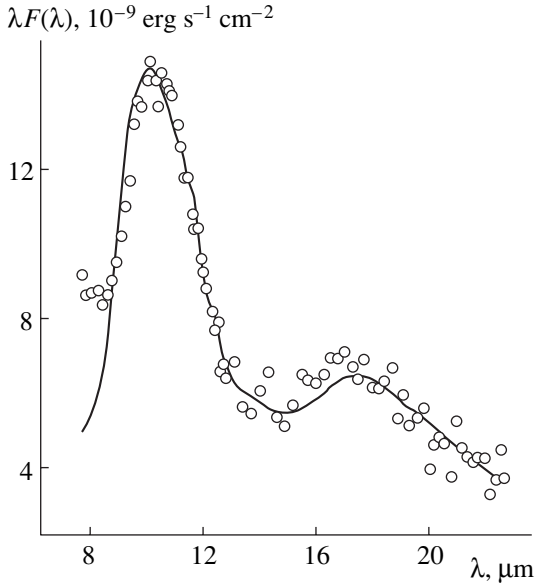

Fig. 3. Spectral energy distribution $\lambda F(\lambda)$ of V1016 Cyg obtained with the low-resolution IRAS spectrometer (circles). The solid curve is the spectral energy distribution for our model for the dust envelope with a single radiation source (model 1), with parameters from the table.

Model parameters of the dust envelope and stellar wind of V1016 Cyg from IRAS and ISO observations

Parameter	IRAS		ISO	
	model 1	model 2	model 1	model 2
L_h, $L_\odot$		35000		33000
L_c, $L_\odot$	9000	9000	9000	9000
$T_{ef,\,h}$, K		150000		145000
$T_{ef,\,c}$, K	2600	2600	2600	2600
T_1, K	700	900	700	900
r_1, 10^{14}cm	5.30	42.2	5.21	40.6
τ_V	11.0	7.0	9.5	6.5
d, kpc	3.4	8.8	3.4	8.8
$\dot{M}$, $10^{-5}\,M_\odot$/yr	1.2	8.8	1.1	8.1
V_e, km/s	8.2	7.2	8.4	7.3
M_s, $M_\odot$	1.7	24.4	1.7	24.0
Σ, 10^{-10}	0.98	1.38	0.55	0.78

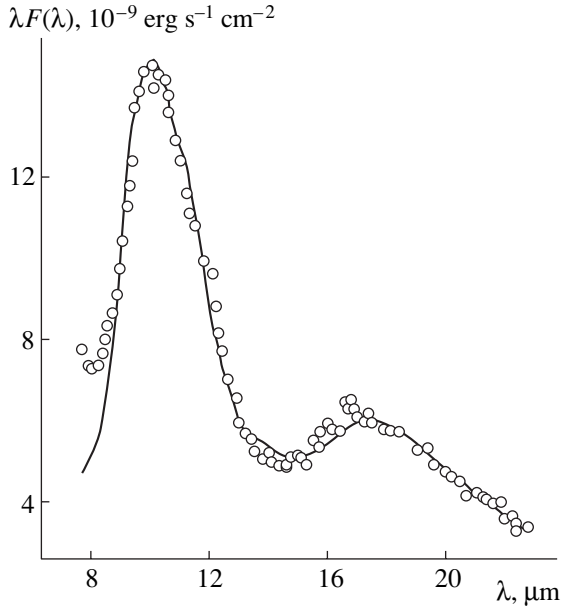

Fig. 4. Spectral energy distribution $\lambda F(\lambda)$ of V1016 Cyg obtained with the short-wavelength spectrometer of the ISO orbital observatory (circles). The solid curve is the spectral energy distribution for our model for the dust envelope with a single radiation source (model 1), with parameters from the table.

In contrast to the case of HM Sge [7], the mean spectral energy distribution for V1016 Cyg based on the IRAS data (acquired in 1983) is almost the same as that for the ISO data of November 5, 1996. This is due to the fairly slow variation of the parameters of the hot component. According to the data of [11], its luminosity and effective temperature at the epoch of the IRAS observations were $L_h = 35000L_\odot$ and $T_{ef,h} = 150000$ K, whereas the values of [11] extrapolated to the epoch of the ISO observations give $L_h = 33000L_\odot$ and $T_{ef,h} = 145000$ K. Nevertheless, our choice of models 1 and 2 was made independently for the IRAS and ISO observations.

To estimate the luminosity of the cool component, we used the period–luminosity relation [12] derived from observations of oxygen Miras in the Large Magellanic Cloud: $M_b = 2.88–3.00\log P$, with the brightness variability period $P = 470^d$. We adopted $M_{b,\odot} = 4\overset{m}{.}75$ for the absolute bolometric magnitude of the Sun [13]. The Mira's effective temperature, $T_{ef,c}$, was found from the relation [14] $\log T_{ef,c} = 3.888–0.174\log P$.

For both models 1 and 2, we made the usual assumptions. Namely, we assumed that the dust envelope had a sharp inner edge at a distance r_1 from the center and that the grain concentration decreased in inverse proportion to the distance squared, out to the envelope's outer edge at $r_2 = 1000r_1$. The optical characteristics of the grain material were chosen to coincide with those of "warm silicate" [15], and the size distribution of the grains, $n(a)$, was described with an MRN model [16]: $n(a) \propto a^{-q}$ (for radii of the spherical grains in the range $a_{min} \le a \le a_{max}$), with $q = 3.5$, $a_{min} = 0.005$ μm, and $a_{max} = 0.25$ μm. In the center of the envelope for model 1, there is a blackbody with the parameters of the Mira, $L_c = 9000L_\odot$ and $T_{ef,c} = 2600$ K, whereas the flux from the central source in model 2 is the sum of the fluxes from two blackbodies with the luminosities and effective temperatures presented in the table. In the latter case, we assumed that the two components did not screen each other and were situated inside a sphere with radius r_1. As noted above, this is approximately the case.

We solved for the radiative transport in the dust envelope using the DUSTY code (version 2.0) for a grid with 30 nodes in radius and 99 nodes in wavelength, in the interval from 0.01 μm to 3.6 cm. The code algorithm is described in [17, 18]. The model input parameters were the dust temperature at the inner edge, T_1, and the optical depth of the envelope at the 0.55 μm wavelength, τ_V. After computing the spectral energy distribution for a model, we then determined the distance d giving the minimum sum of squared deviations of the observed fluxes from the theoretical fluxes Σ. The resulting best fit parameters of the two models for the IRAS and ISO data are collected in the table.

The table demonstrates that the parameters for model 1 derived from independent IRAS and ISO observations are in fairly good agreement. Analysis of the results also shows that model 2 gives an appreciably worse fit to the observed spectral energy distribution in the intermediate IR than model 1. This is confirmed by the data from the table: the sums of squared deviations Σ for model 2 are higher than those for model 1 by approximately a factor of 1.5. Since the total radiation flux is conserved, the increased luminosity of the central source in model 2 leads to overestimation of d, in contradiction with the results of earlier studies of V1016 Cyg. All this suggests that the short-wavelength radiation from the hot component is almost completely absorbed by the ambient gas [8]. For this reason, we will mainly concentrate on the results for model 1.

The solid curves in Figs. 3 and 4 show the spectral energy distributions for model 1, chosen to fit the data from the IRAS and ISO spectrometers. The figures show that the model describes the observations rather well. Figure 5 presents a comparison with observations over a wider spectral range. Here, the solid curve is the logarithm of the flux (in erg s^{-1} cm^{-2} cm^{-1}) as a function of the logarithm of the wavelength (in μm) for model 1, chosen to fit the ISO data. The open circles in Fig. 5 are our *JHKLM* photometric measurements at maximum and minimum brightness of the 470-day variations, and the filled circles are photometric data from IRAS. Though these data were not used to fit the models, the computed curve passes fairly close to the observations in both the near IR and far IR.

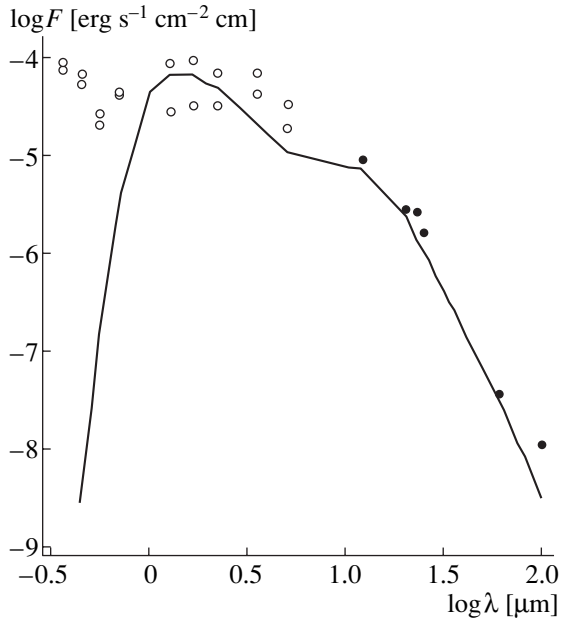

Fig. 5. The 0.4–100 μm spectral energy distribution $\log F(\lambda)$ of V1016 Cyg from our data (open circles) and IRAS data (filled circles). The solid curve is the energy distribution for our dust-envelope model with a single source, selected to fit the ISO data.

5. DETERMINATION OF STELLAR-WIND PARAMETERS

To estimate the parameters of the stellar wind in V1016 Cyg due to the action of the radiation pressure on the dust and the subsequent transfer of momentum to the gaseous medium, we used the gas-dynamics mode of the DUSTY code and carried out computations for the sources of radiation considered and the derived values for the envelope's optical depth. In this mode, the code realizes a self-consistent solution for the radiation transfer and dust motion in a stellar envelope [19]. The density of the silicates was taken to be 3 g/cm^3, and the gas-to-dust mass ratio, to be 200. Using these data, the DUSTY code computed the total mass-loss rate $\dot{M}$, the gas-expansion velocity at the outer edge of the envelope V_e, and an upper limit to the mass of the central radiation source M_s. The resulting stellar-wind parameters for various models are given in the table.

The table again shows that model 2 (with two radiation sources) is less adequate. For example, the upper limits for the masses of the stars are implausibly high, as are the estimates of the mass-loss rate. On the contrary, model 1 yields stellar-wind parameters that are fairly close to those estimated in earlier studies.

Note that we considered only the stellar wind associated with radiation pressure on the dust. This must be supplemented with the stellar wind of the hot component due to the pressure of its radiation on the gas component of the envelope. Despite its low density, the very high velocity of this wind (~500 km/s) could result in a significant mass-loss rate. For this reason, the $\dot{M}$ values given in the Table for model 1 should be considered lower limits for the true mass-loss rate from the symbiotic nova.

6. CONCLUSIONS

Our model fitting to IRAS and ISO observations shows that, as for the symbiotic nova HM Sge [7], a model with a single central source—the Mira star—provides a better description of the observations. This confirms that the hot component's radiation is largely reprocessed by the ambient gas medium and exerts almost no direct influence on the IR spectrum of the symbiotic nova.

We have derived the parameters of the dust envelope and stellar wind from V1016 Cyg using new algorithms and a code for computing radiative transport and dust dynamics. Our results based on independent observational data are in good agreement with earlier studies.

ACKNOWLEDGMENTS

The authors are grateful to astrophysicists from the University of Kentucky (Zeljko Ivezic, Maia Nenkova, Moshe Elitzur) for the possibility to use the DUSTY code for solution of the radiative transport equation and to the scientific teams of the SIMBAD database, the University of Calgary, and the ISO observatory for providing access to observations of V1016 Cyg. This study was supported by grants from the Federal Scientific and Technological Program "Astronomy" the Ministry of Education of the Russian Federation and in part by the Russian Foundation for Basic Research (project no. 00-02-16272).

REFERENCES

1. S. W. McCuskey, IAU Circ., No. 1916 (1965); No. 1917 (1965).
2. O. G. Taranova and B. F. Yudin, Astron. Astrophys. **117**, 209 (1983).
3. O. G. Taranova and B. F. Yudin, Astron. Zh. **63**, 317 (1986) [Sov. Astron. **30**, 193 (1986)].
4. H. M. Schmid, in *Physical Processes in Symbiotic Binaries and Related Systems*, Ed. by J. Mikolajewska (Copernicus Foundation for Polish Astronomy, 1997).
5. O. G. Taranova and V. I. Shenavrin, Pis'ma Astron. Zh. **26** (9), 695 (2000) [Astron. Lett. **26**, 600 (2000)].
6. S. J. Kenyon and R. F. Webbink, Astrophys. J. **279**, 252 (1984).
7. M. B. Bogdanov and O. G. Taranova, Astron. Zh. **78**, 52 (2001) [Astron. Rep. **45**, 44 (2001)].
8. G. L. Bryan and S. Kwok, Astrophys. J. **368**, 252 (1991).

9. H. Schild and H. M. Schmid, Astron. Astrophys. **310**, 211 (1996).
10. M. Cohen, R. G. Walker, and F. C. Witteborn, Astron. J. **104**, 2030 (1992).
11. U. Murset and H. Nussbaumer, Astron. Asrophys. **282**, 586 (1994).
12. M. W. Feast, I. S. Glass, P. A. Whitelock, and R. M. Catchpole, Mon. Not. R. Astron. Soc. **241**, 375 (1989).
13. C. W. Allen, *Astrophysical Quantities* (Athlone Press, London, 1973; Mir, Moscow, 1977).
14. R. Álvarez and M. O. Mennessier, Astron. Asrophys. **317**, 761 (1997).
15. V. Ossenkopf, T. Henning, and J. S. Mathis, Astron. Asrophys. **261**, 567 (1992).
16. J. S. Mathis, W. Rumpl, and K. H. Nordsieck, Astrophys. J. **217**, 425 (1977).
17. Z. Ivezic and M. Elitzur, Mon. Not. R. Astron. Soc. **287**, 799 (1997).
18. Z. Ivezic and M. Elitzur, Mon. Not. R. Astron. Soc. **303**, 864 (1999).
19. Z. Ivezic and M. Elitzur, Astrophys. J. **445**, 415 (1995).

Translated by N. Samus'

Astronomy Reports, Vol. 45, No. 6, 2001, pp. 467–474. Translated from Astronomicheskiĭ Zhurnal, Vol. 78, No. 6, 2001, pp. 541–549.

Partial Mixing of Material in the Radiative Envelope and Convective Core of a Rotating Main-Sequence Star with Mass $16M_\odot$

E. I. Staritsin

Ural State University, Yekaterinburg, 620083 Russia

Received May 11, 2000

Abstract—The evolution of a rotating main-sequence star with a mass of $16M_\odot$ is studied. The flow of material in the radiative envelope is turbulent. When the exchange of energy and chemical elements is taken into account, this turbulence transfers helium and momentum from the convective core to the radiative envelope. The helium content at the stellar surface is enhanced toward the end of the evolution on the main sequence by 0.006–0.306, depending on the character of the star's initial rotation and the horizontal coefficient of the turbulent viscosity. *© 2001 MAIK "Nauka/Interperiodica".*

1. INTRODUCTION

Spectroscopic studies of stellar atmospheres have shown that their helium content increases with the age of the stars in some open clusters [1–3], as well as with the ratio of the linear velocity of the stellar rotation at the equator to the critical velocity [4–6]. The critical velocity is defined here as the velocity of rotation at which material begins to flow outward from the equatorial region. The increase in the helium contents in the atmospheres of binary components with their ages may be even stronger than in the case of isolated stars [7].

The production of helium in a massive main-sequence star ($M \geq 10M_\odot$) is the result of hydrogen burning in its central region. The enhanced helium contents in the atmospheres of massive stars testify to possible partial mixing of materials of the outer stellar layers, whose chemical composition is specified by the properties of the protostellar material, and inner layers, whose chemical composition has been changed by nuclear reactions in the stellar core.

Under the standard assumption of spherical symmetry in the absence of rotation and magnetic fields, complete mixing takes place in a massive main-sequence star only in its central region, the convective core. On the other hand, partial mixing can occur in the layer of variable chemical composition adjacent to the convective core if the conditions for semiconvection are satisfied [8, 9]. No processes able to transport material through the radiative envelope, whose mass represents a substantial part of the stellar mass, are known in the framework of standard, spherically-symmetric models.

One basic and well-observed property of stars is their rotation. Flows of matter in rotating stars are subject to a number of instabilities, whose onset could lead to partial mixing of material in the stellar interiors [10]. We note here first and foremost the shear instability, since it can develop on a dynamic time scale, creating turbulence in the flows in rotating stars. Stratification of the stellar material makes the turbulence anisotropic [11, 12]. Shear flows in horizontal planes (surfaces of constant pressure) arise due to the transport of angular momentum through these surfaces by meridional circulation. The viscosity of the stellar material could prove to be insufficient to suppress horizontal turbulent flows [13]. Vertical shear flows can be produced during the formation of the star, as a result of the evolutionary expansion/compression of various stellar layers, and also during the transfer of angular momentum by vertical meridional circulation. However, the development of vertical turbulence can be suppressed by powerful buoyancy forces in the convective, unstable layers of the star. Energy exchange between a turbulent element and the surrounding medium decreases the stabilizing action of the buoyancy forces [14–16], and the flow of matter in the chemically uniform radiative envelope of a rotating star becomes turbulent [17, 18].

We shall consider in the present paper the possibility of partial mixing of matter in the turbulent radiative envelope and convective core of a rotating star with mass $16M_\odot$ in a model with anisotropic turbulence [11], taking into account the exchange of energy and chemical elements between the turbulent element and the surrounding medium [19, 20].

2. THE MODIFIED RICHARDSON CRITERION

A shear flow in a gravitational field should be turbulent if the work required to interchange two arbitrary fluid elements is less than the kinetic energy released by equalizing their velocities [21]:

$$g\frac{\partial \Delta \ln \rho}{\partial z} < \mathrm{Ri}_c\left(\frac{\partial U}{\partial z}\right)^2, \qquad (1)$$

1063-7729/01/4506-0467$21.00

where Ri_c is the critical value of the Richardson number, g is the free-fall acceleration, U is the flow velocity, and $\Delta\ln\rho$ is the difference between the densities inside and outside the element after movement through a distance z.

In the case of a medium stable to convection, a vertical shift of an element is associated with work against the gravitational force. If the excess of kinetic energy in the flow is not sufficiently large, the vertical shear flow will be laminar. Flow in a horizontal surface of a rotating star becomes nonuniform due to the transport of angular momentum via meridional circulation. The gravitational force does no work when an element is shifted horizontally. The viscosity of the stellar material is also insufficient to stabilize the flow in the horizontal direction. If we suppose that a turbulent flow becomes laminar when the Reynolds number Re becomes comparable to unity, for the characteristic viscosities in massive stars, $\nu_m \sim 10^3$ cm^2/s, the relative difference $\delta\Omega/\Omega$ between the angular velocities of some specified surface of constant pressure near the pole and the equator cannot exceed $\sim 10^{-14}$. The horizontal coefficient of turbulent viscosity ν_h is considerably greater than the vertical coefficient ν_v. As a result, the turbulence almost equalizes the angular velocity in a horizontal surface. Therefore, the change of angular velocity in the horizontal direction is considerably less than in the vertical direction [11]. The angular velocity Ω of a star depends only on the average distance r to the surface of constant pressure: $\Omega = \Omega(r)$. This is referred to as the stratified stellar rotation law.

Let us rewrite $\Delta\ln\rho$ using the differential equation of state

$$d\ln\rho = \alpha d\ln P + \varphi d\ln\mu - \delta d\ln T,$$

where P is the pressure, μ is the mean molecular mass, T is the temperature, $\alpha = (\partial\ln\rho/\partial\ln P)_{T,\mu}$, $\varphi = (\partial\ln\rho/\partial\ln\mu)_{P,T}$, and $\delta = -(\partial\ln\rho/\partial\ln T)_{P,\mu}$. Next, let $H_P = -dz/d\ln P$ be the pressure scale height. Then, the Richardson criterion (1) will take the form

$$\frac{g}{H_P}[\delta(\nabla' - \nabla) - \varphi(\nabla'_\mu - \nabla_\mu)] < \mathrm{Ri}_c\left(\frac{\partial U}{\partial z}\right)^2.$$

We have used the standard notation $\nabla = d\ln T/d\ln P$ and $\nabla_\mu = d\ln\mu/d\ln P$. Primed quantities refer to the material of the element under consideration, and nonprimed quantities, to the surrounding medium. If the element exchanges energy with the surrounding medium, the difference $\nabla' - \nabla$ becomes smaller and the work required to interchange two elements also decreases. Even if the medium is stable in the absence of this energy exchange, it can become turbulent when this exchange is taken into account. On the other hand, if the mean molecular mass of the element does not change ($\nabla'_\mu = 0$) but the chemical composition of the surrounding material varies so that $\nabla_\mu > 0$, then interchanging elements requires more work than in the case of a uniform chemical composition. The gradient of the molecular mass stabilizes the flow.

The exchange of energy between the element and surrounding medium due to remission of photons can be taken into account using the mixing-length theory [22, 23]. The ratio Γ of the difference between the internal energies of the element and the surrounding medium and the energy received by the element from the surrounding medium during its lifetime is related to the adiabatic temperature gradient ∇_a, velocity v, and size l of the element as follows:

$$(\nabla' - \nabla) = \frac{\Gamma}{\Gamma + 1}(\nabla_a - \nabla),$$

$$\Gamma = \frac{vl}{6K},$$

$$K = \frac{4acT^3}{3c_P\rho^2\kappa},$$

where a is Stefan's constant, c is the speed of light, c_P is the specific heat capacity at constant pressure, and κ is the opacity. Taking into account energy exchange in the layers with uniform chemical composition, the Richardson criterion takes the form

$$\frac{\Gamma}{\Gamma + 1}\frac{g\delta}{H_P}(\nabla_a - \nabla) < \mathrm{Ri}_c\left(\frac{\partial U}{\partial z}\right)^2.$$

In the absence of energy exchange, $\Gamma \longrightarrow \infty$, $\Gamma/(\Gamma + 1) \longrightarrow 1$, and we obtain the classical Richardson criterion [21]. On the other hand, if the energy exchange is fairly intensive, then $\Gamma \ll 1$, $\Gamma/(\Gamma + 1) \approx \Gamma$, and the work required to interchange the elements decreases [11]:

$$\Gamma\frac{g\delta}{H_P}(\nabla_a - \nabla) < \mathrm{Ri}_c\left(\frac{\partial U}{\partial z}\right)^2. \quad (2)$$

We will call the state of the medium when the work required to interchange two elements is exactly equal to the kinetic energy released when their velocities are equalized the "state of moderate turbulence." Taking $\nu_v = vl/3$, we obtain from (2) for the state of moderate turbulence

$$\nu_v = 2\mathrm{Ri}_c\frac{H_P}{g\delta}\frac{K}{\nabla_a - \nabla}\left(\frac{\partial U}{\partial z}\right)^2. \quad (3)$$

The turbulence will be suppressed in a layer with variable chemical composition if the work required to interchange two elements is greater than the kinetic energy released when their velocities are equalized:

$$\frac{g\varphi\nabla_\mu}{H_P} > \mathrm{Ri}_c\left(\frac{\partial U}{\partial z}\right)^2. \quad (4)$$

Here, we have assumed that the chemical composition of the turbulent medium does not change.

Our calculations of the evolution of a rotating main-sequence star with mass $16M_\odot$ showed that, when the

energy exchange is taken into account, the turbulence encompasses all layers of the star from the initial boundary of the convective core to the surface [18]. The coefficient of turbulent viscosity, defined by (3), takes on the approximately constant value $\nu_v \approx (2-4)\times 10^7$ cm^2/s over the entire turbulent envelope, and, by the end of the main-sequence evolution, the angular velocity of rotation at the base of the turbulent envelope exceeds the corresponding surface velocity by a factor of 2.1–2.2 in all cases considered. The gradient of the molecular mass in the layer between the current and initial positions of the boundary of the convective core stabilizes the flow, so that turbulence does not develop in this layer. Therefore, the turbulence transfers angular momentum from inner to outer layers of the star. The radial distribution of chemical elements is determined by the nuclear reactions and mixing of material in the convective core.

Variations in the mean molecular mass of a rising element can be produced by horizontal exchanges of material with the surrounding medium due to anisotropic turbulence [19]. The mean molecular mass of an individual element can change due to the disruption of some elements and formation of others from "pieces" of material with different molecular masses [20]. By introducing the quantity Γ_μ in the same way as in mixing-length theory, we can obtain [19]

$$\Gamma_\mu = \frac{vl}{6\nu_h} \quad \text{and} \quad \nabla'_\mu - \nabla_\mu = -\frac{\Gamma_\mu}{\Gamma_\mu + 1}\nabla_\mu.$$

In this case, the exchange of energy between the element and surrounding medium occurs not only via the remission of photons, but also due to turbulence in the horizontal plane, so that

$$\Gamma = \frac{vl}{6(K+\nu_h)}.$$

The Richardson criterion then takes the form

$$\frac{\Gamma}{\Gamma+1}\frac{g\delta}{H_P}(\nabla_a - \nabla) + \frac{\Gamma_\mu}{\Gamma_\mu+1}\frac{g\varphi}{H_P}\nabla_\mu < \mathrm{Ri}_c\left(\frac{\partial U}{\partial z}\right)^2. \quad (5)$$

If $\Gamma_\mu \longrightarrow \infty$, then $\Gamma_\mu/(\Gamma_\mu+1) \longrightarrow 1$, and we obtain the previous restriction (4) for the onset of turbulence in a layer with variable chemical composition. On the other hand, if $\Gamma_\mu \ll 1$, then $\Gamma_\mu/(\Gamma_\mu+1) \approx \Gamma_\mu$, so that less work is required to interchange two small elements. For the same excess kinetic energy in the flow, turbulence will develop due to elements with small sizes. The minimum size of such elements is restricted by the viscosity. The turbulence should not be suppressed if

$$\frac{vl}{\nu_m} > \mathrm{Re}_c, \quad (6)$$

where Re_c is the critical Reynolds number. To estimate the viscosity of the stellar material ν_m, we use here the following expression for a completely ionized hydrogen plasma [10, 24]:

$$\nu_m = \frac{1}{\rho}\frac{2m_\mathrm{H}^{1/2}(kT)^{5/2}}{5e^4\ln\Lambda},$$

$$\Lambda = \frac{3}{2}e^{-3}\left(\frac{m_\mathrm{H}k^3T^3}{\pi\rho}\right)^{1/2},$$

where m_H is the proton mass, e is the electron charge, and k is Boltzmann's constant.

In the case of anisotropic turbulence, $\nu_v \ll \nu_h$ and we obtain from (5) for the state of moderate turbulence:

$$\nu_v = 2\mathrm{Ri}_c\frac{(\partial U/\partial z)^2}{\dfrac{g\delta}{H_P}\dfrac{(\nabla_a - \nabla)}{K+\nu_h} + \dfrac{g\varphi}{H_P}\dfrac{\nabla_\mu}{\nu_h}}. \quad (7)$$

3. BASIC EQUATIONS

In the case of stratified rotation, $\mathrm{div}\,\mathbf{U} = 0$. We can use the Boussinesq approximation to describe the turbulent stress [25]. Then, the motion of material in the rotating star will be described by the Reynolds equation:

$$\rho\frac{d\mathbf{U}}{dt} = \rho\mathbf{g} - \mathrm{grad}\,P + \mathrm{div}(2\rho\nu_t\dot{S}),$$

where $\dot{S}$ is the deformation-rate tensor for the mean turbulent flow, ν_t is the coefficient of turbulent viscosity, and P is the pressure of an ideal gas with radiation. The turbulent pressure in the subsonic flow can be neglected.

Let us introduce the spherical coordinate system (r, θ, φ), whose center is coincident with the center of the star and whose polar axis is coincident with the rotational axis. Then, the φ component of the Reynolds equation [10]

$$\frac{\partial(\rho\omega^2\Omega)}{\partial t} = \mathrm{div}(\rho\omega^2\nu_v\,\mathrm{grad}\,\Omega) \quad (8)$$

describes transfer of angular momentum in the radial direction. Considering the material in a main-sequence star in a two-component approximation, we can write the transfer equation for the concentration X of hydrogen in the radial direction [25]

$$\frac{\partial(\rho X)}{\partial t} = \mathrm{div}(\rho D\,\mathrm{grad}\,X). \quad (9)$$

In (8) and (9), ω is the distance from the rotational axis and D is the coefficient of turbulent diffusion.

The r and θ components in the Reynolds equation describe the influence of the centrifugal force on the mechanical equilibrium of the star. In the particular case when the stellar rotation does not appreciably differ from rigid-body rotation, the action of the centrifugal force can be taken into account via correction fac-

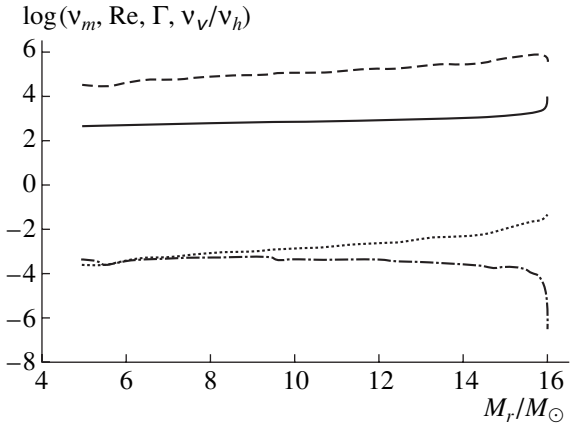

Fig. 1. Distribution of physical parameters in the turbulent radiative envelope of a star with mass $16M_\odot$ for the case of $(\alpha^0, \nu_h) = (2, 10^{10})$ and a hydrogen content in the convective core $X_c = 0.1$: the viscosity ν_m in cm^2/s (solid curve), Reynolds number Re (dashed curve), mixing-length theory parameter Γ (dot–dash curve), and ratio of the coefficients of turbulent viscosity in the vertical and horizontal directions ν_v/ν_h (dotted curve).

tors in the mechanical-equilibrium and radiative-diffusion equations. These correction factors are calculated using the Clairaut–Legendre theory described in [18].

We calculated the evolution of a rotating star in the standard way. All physical variables are treated as functions of the mean distance r from the center to a surface of constant pressure. Thus, the evolution of a rotating star can be calculated in a one-dimensional approximation [18, 26]. We computed the stellar structure using the software of Paczynski [27], modified to take into account the centrifugal force [18]. The evolutions of the distributions of the angular velocity $\Omega(r)$ and hydrogen content $X(r)$ are described by (8) and (9), taking into account the burning of hydrogen in nuclear reactions. We take the fluxes of the angular momentum and hydrogen concentration at the center and stellar surface to be zero. The turbulent viscosity ν_v is determined by (7) if condition (6) is satisfied and is zero otherwise. We adopted the form $\nu_v = v_c l_c/3$ for the turbulent viscosity in the convective core, where the velocity v_c and size l_c of a convective element are determined from the mixing-length theory [22, 23]. All the calculations were carried out with the turbulent Schmidt number $Sc_t = \nu_v/D$ equal to unity. The critical Richardson number Ri_c was taken to be 1/4 [28].

4. HELIUM TRANSPORT IN THE RADIATIVE ENVELOPE

We considered three cases of evolution of a star with mass $16M_\odot$ during the stage of hydrogen burning at its center: $(\alpha^0, \nu_h) = \{(1, 10^{10}), (2, 10^{10}),$ and $(1, 10^{12})\}$. Here, α^0 is the ratio of the angular velocities of the convective core displaying rigid-body rotation and the stellar surface in a chemically-uniform, zero-age model. The value $\alpha^0 = 1$ corresponds to the case of initial rigid-body rotation. When $\alpha^0 = 2$, we specified a linear decrease of the angular velocity $\Omega(m)$ as a function of the current mass m from the boundary of the convective core to the stellar surface. The angular velocity of the surface in the zero-age model Ω_s^0 was taken to be 5.72×10^{-5} s^{-1} in all cases. This angular velocity corresponds to a linear rotational velocity of ~200 km/s at the surface at the equator. We assumed that the coefficient of horizontal turbulent viscosity ν_h $[cm^2/s]$ is independent of the position in the turbulent envelope and of time. We took the chemical composition at the beginning of the evolution to be similar to the solar composition: $(X, Z)^0 = (0.75, 0.02)$, where Z is the heavy-element content.

Typical viscosities in the radiative envelope of a star with mass $16M_\odot$ are 200–1000 cm^2/s and do not appreciably change during the main-sequence evolution. With such viscosities, the Reynolds number in the radiative envelope is in the range 4×10^4–10^6 (Fig. 1). These large Reynolds numbers reflect the fact that the buoyancy forces considerably exceed the viscous forces in the stellar material. The viscosity cannot suppress turbulence in the radiative envelope of the star. The mixing-length theory parameter Γ does not exceed 10^{-3} in the turbulent radiative envelope (Fig. 1). With such values of Γ, turbulence does not contribute to the energy transport in the radiative envelope [23]. The ratio of the coefficients of turbulent viscosity in the vertical direction, calculated using (7), and in the horizontal direction $\nu_v/\nu_h \ll 1$ turns out to be considerably less than unity (Fig. 1); i.e., the criterion for the applicability of (7) is satisfied. The rotating main-sequence star with mass $16M_\odot$ is composed of a convective core, semiconvective zone, and turbulent radiative envelope. We took the diffusion coefficient in the semiconvective zone to be 10^8 cm^2/s [29, 30].

The coefficient of turbulent viscosity ν_v increases from $\sim 3 \times 10^6$ cm^2/s at the base of the turbulent envelope to $(1–10) \times 10^8$ cm^2/s near the stellar surface (Fig. 2). The smaller values of ν_v at the base of the turbulent envelope are associated with the larger gradient of the molecular mass and, consequently, the smaller characteristic scales for turbulent elements whose interchange requires work equal to the released kinetic energy.

The turbulence transfers angular momentum outward from the convective core. As a result, the angular velocity of the convective core decreases as the star evolves on the main sequence (Fig. 3). The decrease in the rotational velocity in the turbulent layers is associated with their motion from the center of the star due to the usual nuclear evolution of central parts of the star. A final increase in the rotational velocity of the inner layers of the star results from their compression upon

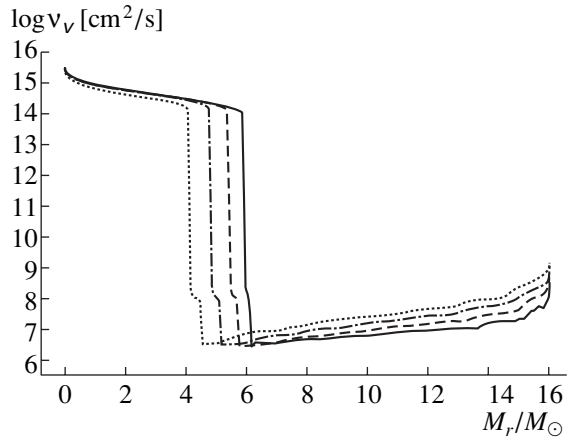

Fig. 2. Distribution of the coefficient of turbulent viscosity in the vertical direction ν_v in the convective core and turbulent radiative envelope of a star with mass $16M_\odot$ for the case of $(\alpha^0, \nu_h) = (2, 10^{10})$ and several values of the hydrogen content at the center: 0.6 (solid curve), 0.4 (dashed curve), 0.2 (dot–dash curve), and 0.0 (dotted curve).

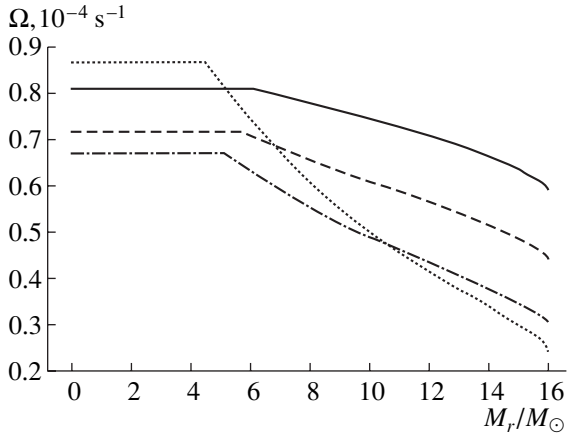

Fig. 3. Distribution of the angular velocity Ω in a star with mass $16M_\odot$ for $(\alpha^0, \nu_h) = (2, 10^{10})$ and several central hydrogen contents: 0.6 (solid curve), 0.4 (dashed curve), 0.2 (dot–dash curve), and 0.0 (dotted curve).

the completion of hydrogen burning in the convective core.

The evolution of the distribution of the hydrogen content in the turbulent envelope depends both on the horizontal coefficient of turbulent viscosity ν_h and the extent to which the rotation is differential in the zero-age model (Figs. 4 and 5). Turbulence transfers hydrogen from the radiative envelope to the convective core. As a result, the amount of hydrogen burned in nuclear reactions in rotating main-sequence stars proves to be greater than under the standard assumption of spherical symmetry without rotation. The products of nuclear burning are carried out from the convective core by turbulence and distributed over the turbulent radiative envelope.

The increase in the helium content in the turbulent radiative envelope increases its transparency, which, in turn, allows a greater energy flux from the central regions. The mass of material for which the condition of convective instability is satisfied in the central part of the star will be greater than in the spherically symmetric case. As a result, when $\nu_h = 10^{10}$ cm^2/s, the mass of the convective core decreases in the course of its evolution less rapidly than in spherically symmetric models (Figs. 4a and 5b). Moreover, the mass of the convective core increases when $\nu_h = 10^{12}$ cm^2/s (Fig. 4b). There are no jumps in the distribution of the hydrogen content at the boundary of the convective core in this case, since shear turbulence in the radiative envelope and semiconvection transfer hydrogen from adjacent layers to the convective core. This action of mixing processes in the radiative envelope on the mass variations in the convective core during the evolution of the star also promotes an increase in the amount of hydrogen burned in nuclear reactions on the main sequence. The increased energy flux also promotes the onset of semiconvection in layers near the convective core. On the other hand, the more uniform hydrogen distribution established by turbulent transport hinders realization of these conditions. As a result, the mass involved in semiconvection

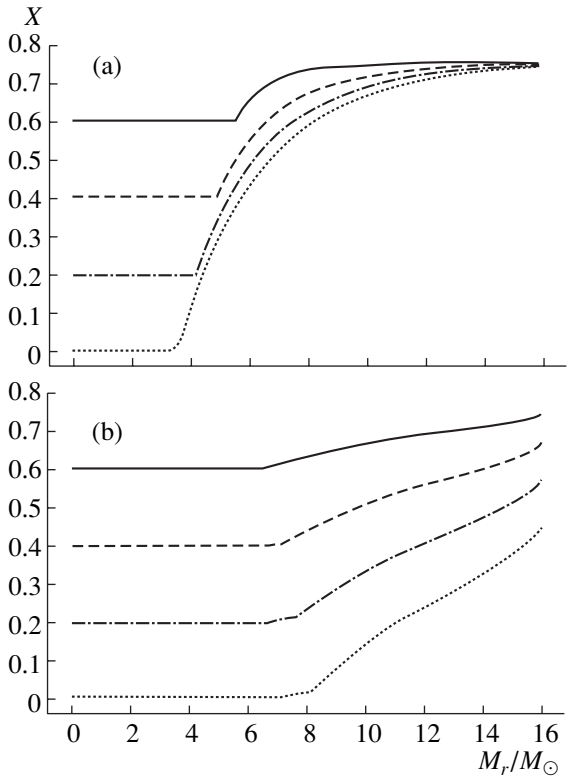

Fig. 4. Distribution of hydrogen in a star with mass $16M_\odot$ for (a) $(\alpha^0, \nu_h) = (1, 10^{10})$ and (b) $(\alpha^0, \nu_h) = (1, 10^{12})$ and several values of the central hydrogen content: 0.6 (solid curve), 0.4 (dashed curve), 0.2 (dot–dash curve), and 0.0 (dotted curve).

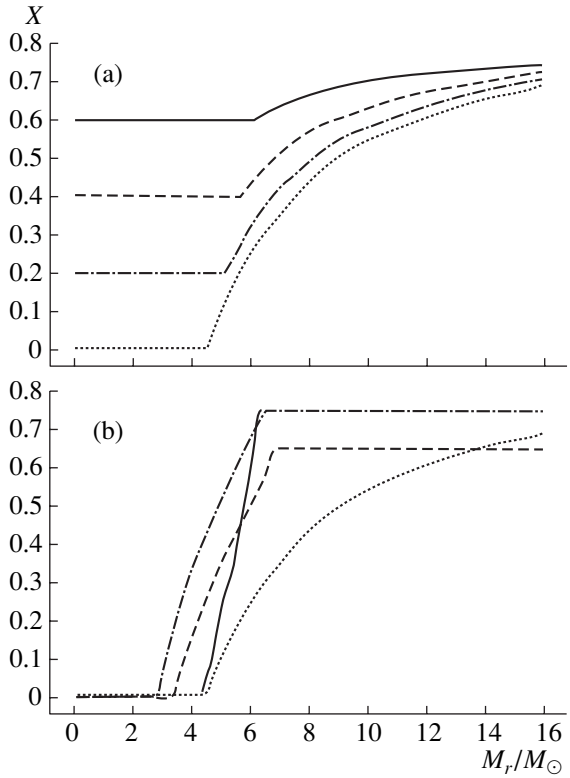

Fig. 5. (a) Distribution of hydrogen in a star with mass $16M_\odot$ for $(\alpha^0, \nu_h) = (2, 10^{10})$ and several central hydrogen contents: 0.6 (solid curve), 0.4 (dashed curve), 0.2 (dot–dash curve), and 0.0 (dotted curve). (b) Distribution of hydrogen in a star with mass $16M_\odot$ by the end of its main-sequence evolution for models without rotation and initial hydrogen contents $X^0 = 0.75$ (dot–dash curve) and $X^0 = 0.65$ (dashed curve) and also for the case $(\alpha^0, \nu_h) = (2, 10^{10})$ (dotted curve). The variations of the boundary of the convective core on the main sequence for $(\alpha^0, \nu_h) = (2, 10^{10})$ are shown by the solid curve.

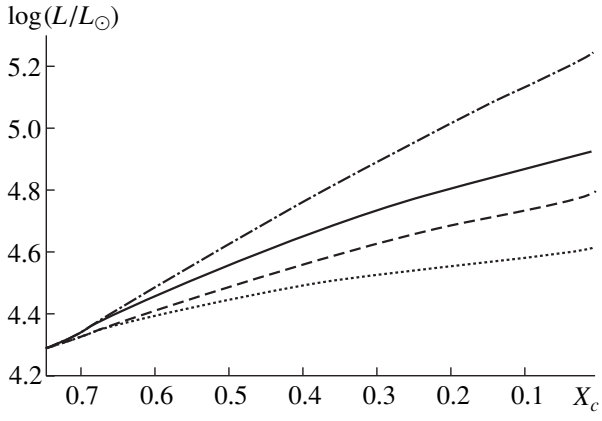

Fig. 6. Luminosity of a star with mass $16M_\odot$ as a function of hydrogen content in the convective core for $(\alpha^0, \nu_h) = (1, 10^{10})$ (dashed curve), $(\alpha^0, \nu_h) = (2, 10^{10})$ (solid curve), $(\alpha^0, \nu_h) = (1, 10^{12})$ (dot–dash curve), and the case without rotation (dotted curve).

is less than $\sim 0.1M_\odot$ when $\nu_h = 10^{10}$ cm^2/s. When $\nu_h = 10^{12}$ cm^2/s, the conditions for semiconvection propagate outward as the star evolves and encompass layers with mass $\sim 1M_\odot$ by the final stage of central hydrogen burning.

The helium mass content in the stellar atmosphere Y_s increases with time due to partial mixing of material in the turbulent radiative envelope and convective core. The final increase in the helium content ΔY_s in the atmosphere of a star with mass $16M_\odot$ during its main-sequence evolution can reach values from 0.006 to 0.306 in the cases considered, with this increase depending on both the rotational state at the time of formation of the star and the horizontal coefficient of turbulent viscosity.

The increase in the transparency of the radiative envelope due to the inflow of a large amount of helium due to turbulent mixing affects the total luminosity and radius of the star. The greater the flux of helium from the convective core to the radiative envelope, the more pronounced the increase in the luminosity of the star during its evolution on the main sequence (Fig. 6). The increased helium content at the base of the turbulent envelope can be approximately described as an outward shift of the layer with variable chemical composition. This shift results in an increase in the stellar radius [31], independent of the reasons for its occurrence. On the other hand, the increase in the helium content in the entire envelope leads to a decrease of the stellar radius. Finally, the transfer of angular momentum from inner to outer layers of the star enhances the action of the centrifugal force on the surface layers, increasing the stellar radius. Thus, the evolutionary change of the stellar radius compared to spherically symmetric models varies with the helium flux from the convective core to the radiative envelope. The stellar radius increases more rapidly than in spherically symmetric models, especially when the helium flux is large. However, if the helium flux increases further, the evolutionary increase in the stellar radius becomes less than in the spherically symmetric case (Fig. 7).

The differences in the evolutionary changes of the luminosities and radii of rotating stars with partial mixing and transfer of momentum in their turbulent radiative envelopes compared to the spherically symmetric case is also reflected in their evolutionary tracks in the Hertzsprung–Russell diagram (Fig. 8). The stronger growth in the luminosity and radius of the rotating stars increases the width of the main sequence. This broadening of the main sequence in models with turbulent mixing in the radiative envelope is limited: as the flux of helium from the convective core to the radiative envelope increases, the evolutionary variations of the radius of the rotating star become smaller than in the spherically symmetric case, and, when the hydrogen in the convective core is depleted, the star moves upward along the main sequence in the Hertzsprung–Russell diagram (see case $(1, 10^{12})$ in Fig. 8).

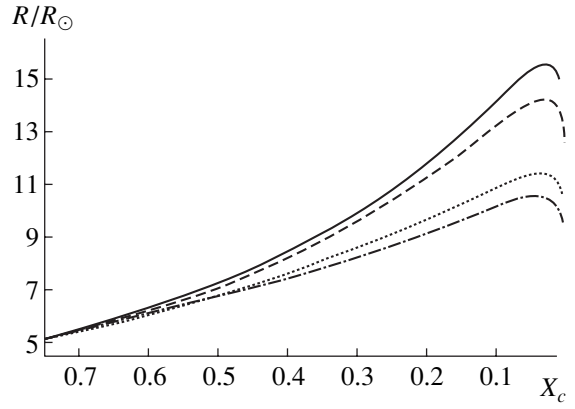

Fig. 7. Radius of a star with mass $16M_\odot$ as function of the hydrogen content in the convective envelope for $(\alpha^0, \nu_h) = (1, 10^{10})$ (dashed curve), $(\alpha^0, \nu_h) = (2, 10^{10})$ (solid curve), $(\alpha^0, \nu_h) = (1, 10^{12})$ (dot–dash curve), and the case without rotation (dotted curve).

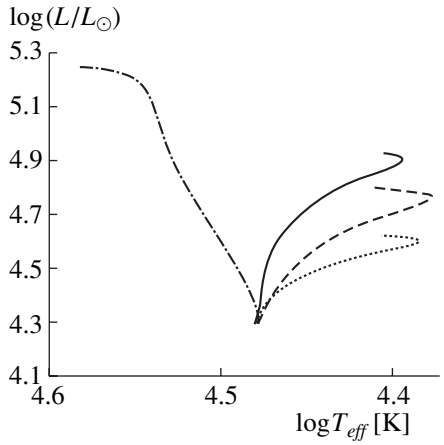

Fig. 8. Evolutionary tracks of a star with mass $16M_\odot$ for $(\alpha^0, \nu_h) = (1, 10^{10})$ (dashed curve), $(\alpha^0, \nu_h) = (2, 10^{10})$ (solid curve), $(\alpha^0, \nu_h) = (1, 10^{12})$ (dot–dash curve), and the case without rotation (dotted curve).

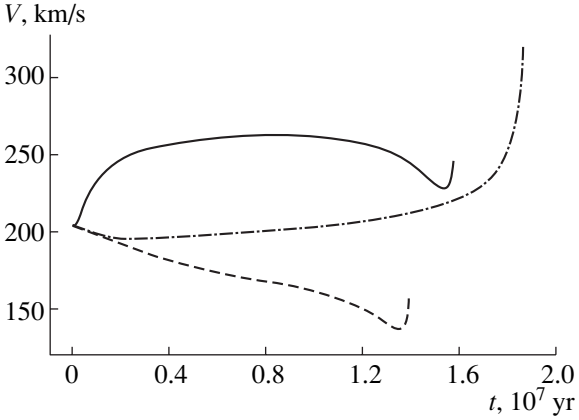

Fig. 9. Evolution of the linear velocity of rotation at the surface of a star with mass $16M_\odot$ at the equator for $(\alpha^0, \nu_h) = (1, 10^{10})$ (dashed curve), $(\alpha^0, \nu_h) = (2, 10^{10})$ (solid curve), and $(\alpha^0, \nu_h) = (1, 10^{12})$ (dot–dash curve).

The main-sequence lifetime is proportional to the mass of hydrogen burned in nuclear reactions in the convective core, and is inversely proportional to the stellar luminosity. The total main-sequence lifetime of a star with mass $16M_\odot$ increases by ~30, ~50, and ~70% for the cases $(1, 10^{10})$, $(2, 10^{10})$, and $(1, 10^{12})$, respectively, compared to the results of calculations assuming spherical symmetry.

The evolution of the linear velocity of rotation at the stellar surface (Fig. 9) depends on both the transfer of angular momentum from inner to outer layers and the flux of helium from the convective core to the radiative envelope. This occurs because the variations in the transparency of the envelope exert a considerable influence on evolutionary variations in the stellar radius.

5. CONCLUSION

The influence of rotation on the evolution of a star with mass $16M_\odot$ is associated primarily with mixing of material from the outer layers of the star, characterized by the chemical composition of the protostellar material, and from the central regions, whose chemical composition has been changed by nuclear reactions. Such mixing takes place due to the turbulent character of the flows in the radiative envelope of the rotating star. This turbulence transfers angular momentum and the products of nuclear reactions from the convective core to the outer layers. On the other hand, the energy transferred by the turbulence is negligible compared to that transferred by radiative diffusion. The mixing increases the helium content in the radiative envelope, which, consequently, increases the stellar luminosity. The mass of hydrogen burned in the convective core on the main sequence, the duration of main-sequence evolution, and the mass of the helium core produced at the center of the star by the end of its main-sequence lifetime are greater than in calculations of the evolution of spherically symmetric, nonrotating stars. The evolutionary changes of the stellar radius compared to those in models without rotation depend on the rate of transfer of helium to the turbulent radiative envelope in a nonmonotonic fashion. When this rate is small, the growth in the stellar radius in the course of hydrogen burning is stronger than in models without rotation. On the other hand, when the rate of helium transfer is large, the growth in radius is less pronounced than in models without rotation. This limits the broadening of the main sequence in the Hertzsprung–Russell diagram, in contrast, for example, to models in which convective elements penetrate beyond the boundary of the convective core [32, 33]. As a result of turbulent mixing in the radiative envelope, the helium content in the atmosphere of a star with mass $16M_\odot$ increases during its main-sequence evolution. The concentrations of CNO-cycle elements in the stellar atmosphere should also vary with time. A similar action of rotation on the evolution of massive stars was established in [34]. On the other hand, the influence of

the centrifugal force on the stellar structure for the characteristic rotational speeds of massive stars is negligible.

Increases in the accuracy of fundamental stellar parameters associated with the use of CCD matrices, refined models of hydrogen and helium atoms and ions, and the development of non-LTE models for stellar atmospheres have enabled the detection of discrepancies between the predictions of the standard theory of stellar evolution, which assumes spherical symmetry, and the results of spectral observations. The masses of stars determined from spectral analyses are always systematically lower than those derived from theories of the evolution of spherically symmetric, nonrotating stars [4]. This same result was obtained earlier for stellar masses derived from the theory of stellar winds [35]. When rotation is taken into account, the stellar evolution occurs at higher luminosities. In other words, a given luminosity corresponds to stars with smaller masses than in models without rotation. Taking into account mixing associated with the rotation opens possibilities for finding agreement between the stellar masses determined from spectral analyses and stellar-wind theory, on the one hand, and evolutionary masses, on the other. Including these processes also enables us to explain the time variations of the helium content in the atmospheres of massive stars. The overall influence of rotation on the evolution of a massive star depends on both the character if its rotation after its formation and the parameters of the turbulent viscosity in the horizontal direction. These conditions can be studied on the basis of meridional-circulation theory.

REFERENCES

1. L. S. Lyubimkov, Pis'ma Astron. Zh. **61**, 29 (1975) [Sov. Astron. Lett. **1**, 226 (1975)].
2. L. S. Lyubimkov, Izv. Krym. Astrofiz. Obs. **55**, 112 (1976).
3. L. S. Lyubimkov, Astrofizika **29**, 479 (1988).
4. A. Herrero, R. P. Kudritzki, J. M. Vilchez, *et al.*, Astron. Astrophys. **261**, 209 (1992).
5. A. Herrero, R. P. Kudritzki, R. Gabler, *et al.*, Astron. Astrophys. **297**, 556 (1995).
6. A. Herrero, L. J. Corral, M. R. Villamariz, and E. L. Martin, Astron. Astrophys. **348**, 542 (1999).
7. V. V. Leushin, Pis'ma Astron. Zh. **61**, 733 (1984).
8. M. Schwarzshild and R. Harm, Astrophys. J. **128**, 248 (1958).
9. A. G. Masevich and A. V. Tutukov, *Stellar Evolution: Theory and Observations* [in Russian] (Nauka, Moscow, 1988).
10. J.-L. Tassoul, *Theory of Rotating Stars* (Princeton Univ. Press, Princeton, 1979; Mir, Moscow, 1982).
11. J.-P. Zahn, Astron. Astrophys. **265**, 115 (1992).
12. J.-P. Zahn, Space Sci. Rev. **66**, 285 (1993).
13. J.-P. Zahn, Mem. Soc. R. Sci. Liege **8**, 31 (1975).
14. J.-P. Zahn, in *Stellar Instability and Evolution*, Ed. by P. Ledoux, A. Noels, and A. W. Rodgers (D. Reidel, Dordrecht, 1974), p. 185.
15. A. Maeder, Astron. Astrophys. **299**, 84 (1995).
16. A. Maeder and G. Meynet, Astron. Astrophys. **313**, 140 (1996).
17. G. Meynet and A. Maeder, Astron. Astrophys. **321**, 465 (1997).
18. E. I. Staritsin, Astron. Zh. **76**, 678 (1999) [Astron. Rep. **43**, 592 (1999)].
19. S. Talon and J.-P. Zahn, Astron. Astrophys. **317**, 749 (1997).
20. A. Maeder, Astron. Astrophys. **321**, 134 (1997).
21. S. Chandrasekhar, *Hydrodynamic and Hydromagnetic Stability* (Clarendon Press, Oxford, 1961).
22. E. Bohm-Vitenze, Z. Astrophys. **46**, 108 (1958).
23. J. P. Cox and R. T. Giuli, *Principles of Stellar Structure* (Gordon and Breach, New York, 1968), Vol. 1, Chap. 14.
24. K. R. Lang, *Astrophysical Formulae: a Compendium for the Physicist and Astrophysicist* (Springer-Verlag, Berlin, 1974; Mir, Moscow, 1978), Vol. 1.
25. E. V. Bruyatskiĭ, *Turbulent Stratified Flows* [in Russian] (Naukova Dumka, Kiev, 1986).
26. A. S. Endal and S. Sofeia, Astrophys. J. **210**, 184 (1976).
27. B. Paczynski, Acta Astron. **20**, 47 (1970).
28. *Hydrodynamic Instabilities and Turbulence*, Ed. by H. Swinney and J. Gollub (Springer-Verlag, Berlin, 1981; Mir, Moscow, 1984).
29. E. I. Staritsin, Nauch. Inf. Astrosovet Akad. Nauk SSSR **67**, 117 (1989).
30. E. I. Staritsin, Nauch. Inf. Astrosovet Akad. Nauk SSSR **68**, 35 (1990).
31. D. Lauterborn, S. Refsdal, and A. Weigert, Astron. Astrophys. **10**, 97 (1971).
32. A. G. Masevich, E. I. Popova, A. V. Tutukov, and L. R. Yungel'son, Nauch. Inf. Astrosovet Akad. Nauk SSSR **47**, 31 (1981).
33. E. I. Staritsin, Nauch. Inf. Astrosovet Akad. Nauk SSSR **65**, 17 (1988).
34. G. Meynet, Astron. Soc. Pac. Conf. Ser. **131**, 96 (1998).
35. M. Groenewegen, H. Lamers, and A. Pauldrach, Astron. Astrophys. **221**, 78 (1989).

Translated by Yu. Dumin

Astronomy Reports, Vol. 45, No. 6, 2001, pp. 475–481. Translated from Astronomicheskiĭ Zhurnal, Vol. 78, No. 6, 2001, pp. 550–557.

Measurements of the General Magnetic Fields of Active Late-Type Stars

T. N. Tarasova, S. I. Plachinda, and V. V. Rumyantsev

Crimean Astrophysical Observatory, p/o Nauchnyĭ, Crimea, 98409 Ukraine

Received September 14, 2000

Abstract—Measurements of the general magnetic fields of active, late-type stars obtained with the 2.6-m Shaĭn telescope of the Crimean Astrophysical Observatory are reported. Statistically significant values of the magnetic fields of ϵ Eri and 61 Cyg A have been detected. The magnetic fields range from –10 to 21 G. The magnetic-field values for ϵ Eri and 61 Cyg A exceed the solar field by an order of magnitude; ϵ Eri is more active than the Sun, while 61 Cyg A has approximately the same activity level as the Sun. There is some evidence for variations in the general magnetic fields of these stars associated with their axial rotation. © *2001 MAIK "Nauka/Interperiodica".*

1. INTRODUCTION

The activity of late-type stars has been well studied, and observational data for over two thousand active, late-type stars have been obtained. An analogy between the activity of such stars and solar activity was recently established, based on a number of observational facts. For example, the x-ray luminosity of these stars depends on their angular velocity [1], providing evidence that their x-ray emission is generated by processes similar to those associated with solar activity. Observations in the chromospheric ionized calcium line carried out over several decades showed that a large fraction of active, late-type stars display a long-term cyclic variability similar to that of the Sun [2]. Drawing an analogy with the Sun has also been fruitful in describing the spots on red dwarfs [3]. Moreover, certain common features were detected for short-lived stellar and solar flares [4].

The magnetic fields of spots and active regions play the determining role in the physical processes in the Sun responsible for solar activity. On the other hand, information about strong, local magnetic fields alone is insufficient to describe the global magnetic-field structure and long-term variations similar to the magnetic solar cycle and data on large-scale magnetic fields are also necessary.

Studies of the magnetic field of the Sun as a star (the so-called general magnetic field) conducted at the Mount Wilson, Stanford, and Crimean Astrophysical Observatories have shown that the general field has a number of properties that enable us to consider it a special large-scale characteristic of solar magnetism. The structure of the magnetic fields of active late-type stars seems to be similar to that of the solar field. This is confirmed by the parameters of the local magnetic fields on such stars obtained spectroscopically [5–14].

Measurements of the magnetic fields of late-type active stars via Zeeman polarimetry and of the magnetic field of the Sun as a star yield the intensity of the longitudinal component of the magnetic field averaged over the surface, which is usually called the general magnetic field [15]. The general magnetic field of the Sun is quite small (slightly over 1 G at activity maximum [15]), and its role in the processes responsible for activity is not as important as the role of local magnetic fields. Nevertheless, there is evidence that the large-scale magnetic field is a considerably more important factor in the activity of some active, late-type stars than in the case of the Sun [16]. For this reason, investigations of the large-scale magnetic fields of active, late-type stars are of considerable interest.

Unfortunately, it is quite difficult to measure the large-scale magnetic fields of such stars. First, the magnetic fields of active regions can make a substantial contribution to the measured magnetic fields of stars more active than the Sun. Second, a pure dipolar large-scale field can be observed on active, late-type stars very rarely, for example, at certain fixed phases of the stellar cycle. Moreover, observations must take into account the fact that deviations from the dipolar structure of the large-scale magnetic field can be substantial due to the arbitrary angles between the rotational axis, magnetic axis, and the line of sight to the observer. Therefore, the sinusoidal behavior of the general magnetic field as a function of the stellar-rotation phase cannot be expected *a priori*. Finally, the accuracy required to carry out such measurements is several G. As a result, until recently, only a few statistically significant measurements had been made [17–20]. Magnetic fields similar to the general magnetic field of the Sun were not detected on these stars.

On the other hand, measurements of the magnetic-field intensity on ξ Boo A revealed variations in the

1063-7729/01/4506-0475$21.00 © 2001 MAIK "Nauka/Interperiodica"

Table 1. Spectral lines used in the magnetic-field measurements

No.	λ, Å	Chemical element	Multiplet	*J*–*J*	Configuration	g_{eff}	χ^1 Ori	ξ Boo A	ϵ Eri	61 Cyg A
1	2	3	4	5	6	7	8	9	10	11
1	6200.313	Fe I	207	2–3	^{3}F–^{3}F	1.510	×	×	×	×
2	6213.430	Fe I	62	1–1	^{5}P–^{5}D	2.000	×	×	×	×
3	6213.866	V I	20	9/2–9/2	^{6}D–^{6}F	1.470				×
4	6215.144	Fe I	1018	2–3	^{3}F–^{3}G	0.850	×	×		
5	6216.354	V I	19	5/2–7/2	^{6}D–^{6}D	1.440				×
6	6219.281	Fe I	62	2–2	^{5}P–^{5}D	1.660	×	×	×	×
7	6224.529	V I	20	7/2–7/2	^{6}D–^{6}F	1.430			×	×
8	6226.736	Fe I	981	3–4	^{3}D–^{5}F	1.350		×	×	
9	6229.228	Fe I	342	1–1	^{3}P–^{3}D	0.990			×	
10	6230.723	Fe I	207	4–4	^{3}F–^{3}F	1.240	×	×		
11	6232.641	Fe I	816	2–1	^{5}P–^{5}D	1.990	×	×	×	×
12	6233.164	V I	20	5/2–5/2	^{6}D–^{6}F	1.470				×
13	6237.319	Si I	28	1–2	^{3}D–^{3}F	0.750*	×	×	×	
14	6238.392	Fe II	74	3/2–3/2	^{4}D–^{4}P	1.460	×	×		
15	6244.466	Si I	27	2–2	^{3}D–^{1}D	1.083*		×		
16	6246.319	Fe I	816	3–3	^{5}P–^{5}D	1.580	×	×	×	×
17	6247.557	Fe II	74	5/2–3/2	^{4}D–^{4}P	1.030	×	×		
18	6251.827	V I	19	7/2–7/2	^{6}D–^{6}D	1.570			×	×
19	6252.555	Fe I	169	6–5	^{3}H–^{3}G	0.950	×	×	×	×
20	6254.258	Fe I	111	2–1	^{3}P–^{3}P	1.510				×
21	6256.887	V I	19	5/2–5/2	^{6}D–^{6}D	1.620				×
22	6258.102	Ti I	104	3–4	^{3}F–^{3}G	1.000		×	×	
23	6258.706	Ti I	104	4–5	^{3}F–^{3}G	1.110		×		
24	6261.098	Ti I	104	2–3	^{3}F–^{3}G	0.830		×	×	
25	6265.134	Fe I	62	3–3	^{5}P–^{5}D	1.580	×		×	×
26	6266.307	V I	20	5/2–3/2	^{6}D–^{6}F	2.050				×

Lande factors taken from [25] are marked by asterisks.

field as a function of the axial-rotation phase [21], making it possible to begin measurements of the general magnetic fields of solar-type stars. Such observations are of considerable interest, even if they can be carried out for a limited number of such stars.

The aim of the present study was to try to detect the general magnetic fields of stars whose levels of activity are higher than (e.g., ϵ Eri and χ^1 Ori) or close to (e.g., 61 Cyg A) that of the Sun.

2. APPARATUS AND OBSERVATIONS

The observations were carried out using a modified Zeeman analyzer mounted at the Coudé focus of the 2.6-m Shaĭn telescope of the Crimean Astrophysical Observatory. Circular polarization was recorded in the profiles of spectral lines, providing measurements of the longitudinal component of the magnetic field averaged over the entire observable disk.

The entrance λ/4 plate was rotated through 90° before each exposure, so that spectra with different circular polarizations were projected onto the same location on a CCD. This method for measuring the magnetic field enabled us to achieve a considerable increase in the measurement accuracy (for more detail, see [20]).

The observations were conducted at 6200–6260 Å. The reciprocal dispersion was 3 Å/mm, and the resolution was about 30 000. The signal-to-noise ratio for the spectra varied from 300 to 450. Preliminary reduction of the spectra was carried out using standard methods and the SPE software developed at the Crimean Astrophysical Observatory by S.G. Sergeev and V.V. Rumyantsev.

For our magnetic-field estimates, we selected lines free from blending and with depths exceeding 10%. For this purpose, we calculated synthetic spectra for each star using the MERSEN software [22, 23] and the VALD database [24]. The characteristics of spectral lines taken from the VALD database and used for our magnetic-field calculations are presented in Table 1. The columns give a line's (1) identification number, (2) wavelength, (3) corresponding chemical element, (4) multiplet number, (5) quantum transition, (6) configuration of this transition, and (7) Landé factor. There

were no Landé factors for two lines in the VALD database, and we adopted values from the tables of Beckers [25] (marked by asterisks in Table 1). The crosses in the four last columns (8–11) indicate the lines used to calculate the magnetic fields of the stars χ^1 Ori, ξ Boo A, ϵ Eri, and 61 Cyg A.

3. CHARACTERISTICS OF THE ACTIVITY OF THE STUDIED STARS

Such manifestations of the magnetic fields of solar-type stars as chromospheric and coronal activity have been widely studied. Observations conducted at the Mount Wilson Observatory over two decades (1976–1995) for over 100 early F to late K dwarfs and subgiants showed that the character of the variable emission at the centers of the H and K lines of Ca II is cyclic for some stars, and similar to the 11-year solar cycle. The variations in the Ca II H and K emission of other stars are irregular, while this emission is constant for a third group of stars [2]. The stars with irregular variability are characterized by greater chromospheric emission in the Ca II H and K lines compared to stars displaying cyclic variability or a constant level of emission [26, 27]. In their analysis of the x-ray flux detected from 0.1 to 2.4 keV by the *ROSAT* satellite during its all-sky survey, Hempelmann *et al.* [28] found that the average x-ray fluxes for these three groups of stars differ by an order of magnitude, with the stars with irregular variability in their Ca II H and K emission having the largest x-ray fluxes.

We carried out magnetic-field measurements for two stars with chromospheric and coronal activity levels exceeding the solar level (χ^1 Ori and ξ Eri) and for one star whose activity level is close to that of the Sun (61 Cyg A). We shall compare our magnetic-field measurements for these stars with the characteristics of the general magnetic field and activity level of ξ Boo A.

The star ξ Boo A (HD 131156A, G8V) is a visual binary system whose components have the masses 0.85 and $0.72M_\odot$ [29–31]. Its chromospheric activity is higher than average [2] and has an irregular character with a variability timescale of several years (see Fig. 1 in [32]). The x-ray flux exceeds the solar value by almost two orders of magnitude (see Table 3 below). Studies taking into account the effects of radiative transport indicate that about 18% of the stellar surface is covered by magnetic fields and the field intensity in active regions is 1900 G [7, 11].

On the other hand, χ^1 Ori (HD 39587, G0V) is a spectroscopic binary with an orbital period of 14.2 ± 0.06 yr. The mass of the secondary is $0.15 \pm 0.01M_\odot$, and its brightness is less than $V = 8.8$ [33]. Therefore, only the main component of the system can be detected in the spectrum. This is an active and quite young star, whose age is 6×10^8 yr [34]. Its chromospheric activity exceeds the average level and has an irregular character [2]. The x-ray flux is almost two orders of magnitude higher than the solar value [28]. Savanov and Savel'eva [14] estimated the magnetic flux from active regions (i.e., the magnetic-field intensity multiplied by the fraction of the stellar surface covered by this field) to be $fB = 3590 \pm 870$ G.

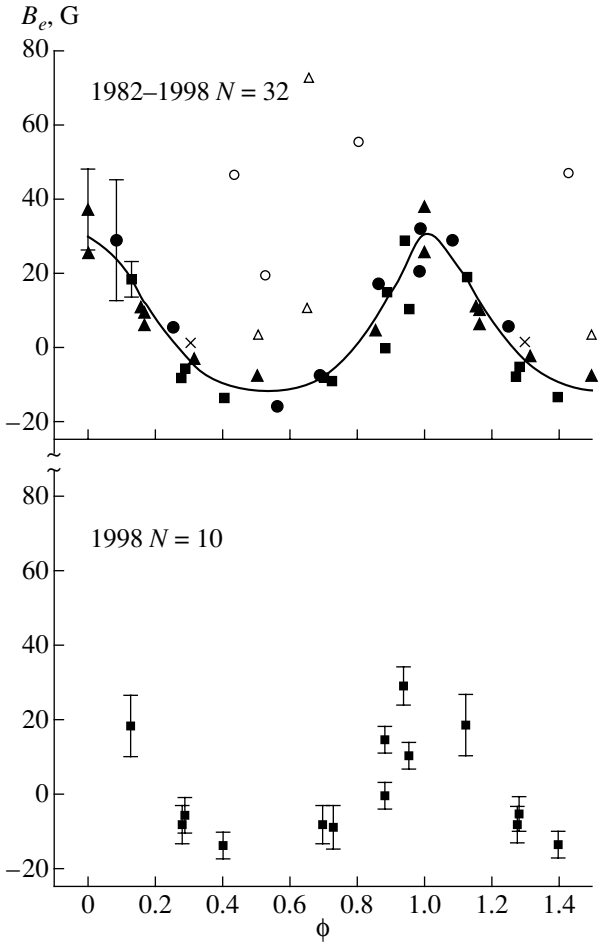

The dependence of the intensity of the general magnetic field of ξ Boo A on its axial-rotation phase is drawn in the top panel. The measurements of Borra *et al.* [18] are marked by the filled triangles, the single measurement of Brown and Landstreet [17] by the cross, the Stokes-meter measurements of Hubrig *et al.* [19] by the filled circles, and the measurements of Plachinda and Tarasova [21] by the filled squares. The hollow symbols refer to measurements that are not in agreement with the phase curve. The plot in the bottom panel contains only the measurements of Plachinda and Tarasova [21].

ϵ Eri (HD 22049, K2V) is an active dwarf with strong Ca II H and K emission. Its rotational period is 11.68 d [35]. The Ca II H and K emission is characterized by long-term chaotic variability with a weakly expressed five-year cycle [36]. The x-ray flux exceeds the solar value by over an order of magnitude [28]. Danks and Lambert [37] found some evidence for rotational modulation of the equivalent width of the He I D3 line (5876 Å), whose 11.3-d period agrees well with the rotational period derived from variations of the Ca II H and K emission (see Table 3 below). The intensity

of the local magnetic fields on this star derived from spectroscopic observations is $B = 1440$ G, and the fraction of its surface covered by magnetic fields is $f = 8.8\%$ [12].

Finally, 61 Cyg A (HD 201091, K5V) is one component of a visual binary. This star possesses a lower level of chromospheric and coronal activity than the other stars described above. The observed variability of the Ca II H and K emission demonstrates a clearly expressed activity cycle with a 7.3-yr period. During the observations, the star was at its activity minimum [2]. The Ca II H and K and x-ray fluxes are approximately equal to the solar values (see Table 3 below). According to [38], 25–30% of the total stellar surface is covered by spots and the intensity of the magnetic fields in active regions were 2660 and 3240 G. Savanov and Savel'eva [39] estimated $fB = 1300 \pm 250$ G. However, subsequent studies of the local magnetic fields taking into account radiative transport yielded infrared filling factors of 2–3% and magnetic-field intensities of about 2–3 kG for stars similar to 61 Cyg A [12].

We determined the radial velocities for 61 Cyg A at seven epochs over August 1–8, 1998. The average radial velocity was -65.32 ± 0.16 km/s. A Th–Ar lamp spectrum was used as a laboratory reference for the wavelength scale. Reduction to the barycenter of the solar system was carried out with accuracy better than 1 m/s.

4. OBSERVATIONAL RESULTS AND DISCUSSION

The general magnetic-field intensities we derived for the stars listed above and the corresponding results of other authors are presented in Table 2. By analogy with the Sun, we will call the measured intensity of the longitudinal component of the magnetic field averaged over the stellar surface the general magnetic field. The columns of Table 2 give the (1) name of the star, (2) observation date, (3) corresponding Julian date, (4) intensity of the general magnetic field, (5) rms error in the field measurement, (6) ratio of the magnetic-field intensity to the rms error (if this ratio ≥ 2), and (7) number of individual magnetic-field measurements for the specified star on the specified date. Table 2 also presents the magnetic-field intensity estimates of Borra *et al.* [18] and Brown and Landstreet [17].

Since there are no previous data on the general magnetic fields of active, late-type stars, our results can be compared only with the characteristics of the general magnetic fields of the Sun and of ξ Boo A, described by Plachinda and Tarasova [21]. The general magnetic field of ξ Boo A as a function of the phase of its axial rotation is shown in the figure. All available measurements of the magnetic field of this star are presented in the top panel. The average errors of the magnetic-field measurements of various authors at various epochs are indicated by the vertical bars. Our magnetic-field measurements in 1998 with their errors for each phase of the rotational period are presented in the bottom panel. In both panels, the field in G is plotted along the vertical axis and the phase of the rotational period along the horizontal axis.

A period search was carried out using standard methods and the ISDA software [40]. A method most suitable for small numbers of observations was applied [41]. The period of the rotational modulation of the magnetic field found in this way was 6.1455 ± 0.0003 d [21], quite close to the rotational period of the star derived from variations in the chromospheric emission [35]. When calculating the phase, the date corresponding to the maximum magnetic field was adopted as the zero epoch. The hollow symbols in the top panel of the figure denote values that are not in agreement with the assumed phase curve. We do not know the reasons for these deviations. When constructing the phase curve, they were treated as random outliers, probably reflecting low quality of the corresponding measurements. The figure shows that the general magnetic-field intensities obtained by different authors are in quite good agreement. The range of variations in the general magnetic field of this star is from +30 G to –10 G. Therefore, this magnetic field exceeds the solar field by over an order of magnitude.

Only two measurements had been carried out previously for ϵ Eri [18], neither of them statistically significant. In contrast, three of our nine measurements were statistically significant. These measurements indicate that the magnetic field of ϵ Eri varies from –9.9 to 21.3 G; apparently, the magnetic field of this star is variable. However, more measurements are needed to confirm this. The activity of this star exceeds the solar level and is approximately the same as the activity of ξ Boo A. The statistically significant estimates of the general magnetic field exceed the general magnetic field of the Sun by more than an order of magnitude and are comparable with the general magnetic field of ξ Boo A.

Three previous measurements of the general magnetic field of χ^1 Ori are available [18] (see Table 2), none of them statistically significant. Despite our higher accuracy, our five measurements were likewise not statistically significant. Further studies are required to detect possible variability in the magnetic field of this star.

The magnetic field of 61 Cyg A was measured in two previous studies—by Brown and Landstreet [17] and Borra *et al.* [18] (see Table 2)—but none of these measurements were statistically significant. We carried out 15 measurements for this star, three of which were statistically significant. Our series of magnetic-field measurements for this star also provide some evidence for variability in the general magnetic field. However, as for the other stars discussed above, further measurements are required before firm conclusions can be drawn. The activity level of this star is lower than that of ξ Boo A and approximately the same as the solar level. The statistically significant values of the general

Table 2. Magnetic-field intensities

1	2	3	4	5	6	7	8
star	date	JD2400000+	B_e, G	σ, G	B_e/σ	N	author
ϵ Eri	09.09.98	51065.555	0.1	2.3		66	
	02.10.98	51088.565	2.9	2.3		64	
	25.10.98	51112.466	−6.3	2.1	3	60	
	15.11.98	51133.475	−5.4	2.7	2	60	
	27.12.98	51175.262	−1.9	4.7		38	
	28.12.98	51176.260	21.3	4.5	4.7	27	
	03.01.99	51182.215	−9.5	4.5	2.1	38	
	04.01.99	51183.198	−9.9	2.2	4.5	43	
	05.01.99	51184.222	−3.0	2.2		65	
		44918.486	−1.4	7.1			Borra *et al.* [18]
		45291.507	4.7	10.8			Borra *et al.* [18]
χ^1 Ori	16.11.98	51133.571	10.9	5.4	2.0	63	
	28.12.98	51175.351	1.6	4.2		61	
	03.01.99	51182.357	4.1	11.0		72	
	04.01.99	51183.378	−8.5	3.8	2.2	57	
	05.01.99	51184.381	4.5	4.9		54	
		44918.548	9.5	21.0			Borra *et al.* [18]
		44925.589	4.7	6.6			Borra *et al.* [18]
		45293.589	1.5	24.0			Borra *et al.* [18]
61 Cyg A	15.07.98	51010.343	−12.3	2.4	5.1	69	
	16.07.98	51011.324	−13.8	3.2	4.3	35	
	22.07.98	51017.482	3.8	1.5	2.5	96	
	26.07.98	51021.349	−1.6	1.8		76	
	01.08.98	51027.457	4.5	2.0		64	
	02.08.98	51028.449	0.6	1.6		58	
	03.08.98	51029.460	1.6	2.7		65	
	04.08.98	51030.462	−0.2	1.8		63	
	05.08.98	51031.449	−1.9	2.2		64	
	07.08.98	51033.462	7.0	2.5	2.8	65	
	08.08.98	51034.469	0.6	1.7		113	
	01.09.98	51058.262	−1.4	2.5		27	
	02.09.98	51059.500	3.1	1.7		112	
	08.09.98	51065.455	3.1	1.9		59	
	05.10.98	51092.331	−6.2	1.7	3.6	70	
		44035.889	14.0	14.0			Brown and Landstreet [17]
		45293.333	−9.0	40.0			Borra *et al.* [18]

magnetic field exceed the solar general magnetic field by more than an order of magnitude and are comparable to the fields measured for ξ Boo A.

Table 3 presents the statistically significant magnetic-field values and some characteristics of the activity of the Sun and the studied stars. The columns give (1) the name of the star; (2) its HD number; (3) its spectral class; (4) its rotational period, derived from analyses of time variations in the chromospheric-emission index [35]; (5) the logarithm of the quantity $\langle R_{HK}\rangle$, equal to the ratio of the flux in the Ca II H and K lines to the total bolometric flux of the star [27]; (6) the log-

Table 3. Activity and maximum values of the general magnetic field of the Sun and studied stars

Star	HD	Spectral class	P_{rot}, d	$\log R_{HK}$	$\log L_x$ [erg/s]	B_{e_-}, B_{e_+}, G
Sun		G2 V	26.09	–4.901	26.70	–1.0, 1.0
ϵ Eri	22049	K2 V	11.68	–4.455	28.32	–9.9, 21.3
χ^1 Ori	39587	G0 V	5.36	–4.426	29.08	–
ξ Boo A	131156	G8 V	6.31	–4.363	28.94	–13.9, 28.9
61 Cyg A	201091	K5 V	35.37	–4.764	27.45	–13.8

The following sources of data were used: P_{rot} was taken from Donahue *et al.* [35]; $\log R_{HK}$ from Baliunas *et al.* [27]; $\log L_x$ from Hunsch *et al.* [42]; and B_{e_-}, B_{e_+}, for the Sun from Khaneĭchuk [15].

arithm of the x-ray luminosity [42]; and (7) the maximum statistically-significant values of the magnetic-field intensity with opposite signs measured in our study. The absence of statistically significant measurements for χ^1 Ori is indicated by a dash in this last column.

The tabulated Ca II H and K fluxes, x-ray fluxes, and rotational periods suggest that 61 Cyg A can be considered similar to the Sun; i.e., it is older and less active than ξ Boo A, ϵ Eri, and χ^1 Ori. The local magnetic fields of older stars, with lower levels of chromospheric and coronal emission, are weaker than the fields of younger stars, with higher levels of emission. This is associated with the fact that stars lose angular momentum in the course of their evolution, since some of the rotational energy is transferred to the surrounding medium by their magnetized stellar winds. The decrease in the axial-rotation velocity reduces the efficiency of magnetic-field generation. It has been established that the x-ray luminosities of late-type stars decrease as their ages increase [43]. In addition, observations of the Ca II H and K emission of more than 100 early F to late K main-sequence stars have shown that stars possessing higher levels of activity and irregular variability in their emission are younger than those possessing lower activity levels and cyclic or constant emission [44]. The studies of Saar [45] demonstrated that the magnetic flux from active regions (spots, faculae) is correlated with the chromospheric and coronal flux. However, as we can see in Table 3, the statistically significant measurement of the general magnetic field of 61 Cyg A is comparable to the values for the other two, more active, stars and exceeds the solar value by an order of magnitude.

5. CONCLUSION

The aim of the present paper was investigation of the general magnetic fields of solar-type stars displaying various types of activity. Three of these stars (ξ Boo A, ϵ Eri, and χ^1 Ori) are younger and more active than the Sun. The remaining star studied, 61 Cyg A, is older, and its level of activity is similar to the solar level. We were able to derive statistically significant values of the general magnetic fields of two stars—ϵ Eri and 61 Cyg A—for the first time.

The statistically significant values of the general magnetic field for the young, active star ϵ Eri exceed the general magnetic field of the Sun by more than an order of magnitude and are comparable to the fields of ξ Boo A.

Despite its lower level of coronal and chromospheric emission, similar to the solar level, the general magnetic field of the less active and older star 61 Cyg A is comparable to that of the active star ξ Boo A and exceeds the general magnetic field of the Sun by more than an order of magnitude.

The variation of the magnetic field of ξ Boo A as a function of its rotational phase (see figure) shows that the observed magnetic field includes a dipolar component of the large-scale magnetic field. The geometric configuration of the rotational axis, magnetic axis, and their orientation relative to the line of sight to the observer enabled us to detect this component.

We have now conducted measurements of the magnetic field of 61 Cyg A covering all phases of the rotational period. As in the case of ξ Boo A, we observe clearly expressed variability in the magnetic field as a function of the rotational phase of this star. Our results for this star are now being prepared for publication.

ACKNOWLEDGMENTS

We are grateful to V.A. Kotov and V.I. Khaneĭchuk for fruitful discussion of the problem under consideration, as well as to V.V. Tsymbal and C.R. Cowley for the software that enabled us to calculate the synthetic spectra.

REFERENCES

1. R. Palavicini, Astron. Astrophys. Rev. **1**, 177 (1989).
2. S. L. Baliunas, R. A. Donahue, W. H. Soon, *et al.*, Astrophys. J. **438**, 269 (1995).
3. I. Yu. Alekseev and R. E. Gershberg, Astron. Zh. **74**, 240 (1997) [Astron. Rep. **41**, 207 (1997)].
4. M. M. Katsova, A. Ya. Boiko, and M. A. Livshits, Astron. Astrophys. **321**, 549 (1997).
5. R. D. Robinson, Astrophys. J. **239**, 961 (1980).

6. S. H. Saar, Astrophys. J. **324**, 441 (1988).
7. G. W. Marcy and G. S. Basri, Astrophys. J. **345**, 480 (1989).
8. G. Mathys and S. K. Solanki, Astron. Astrophys. **208**, 189 (1989).
9. G. S. Basri, G. W. Marsy, and J. A. Valenti, Astrophys. J. **390**, 622 (1992).
10. S. H. Saar and S. L. Baliunas, in *The Solar Cycle (Proc. of the NSO/Sac Peak 4th Solar Cycle Workshop)*, Ed. by K. L. Harvey (ASP, San Francisko, 1992), p. 197.
11. J. L. Linsky, C. Andrielis, S. H. Saar, *et al.*, in *The Eighth Cambridge Workshop on Cool Stars, Stellar Systems, and the Sun*, Ed. by J.-P. Caillault (ASP, San Francisko, 1994), p. 438.
12. J. A. Valenti, G. W. Marcy, and G. S. Basri, Astrophys. J. **439**, 939 (1995).
13. I. Ruedi, S. K. Solanki, G. Mathys, and S. H. Saar, Astron. Astrophys. **318**, 429 (1997).
14. I. S. Savanov and Yu. Yu. Savel'eva, Astron. Zh. **74**, 919 (1997) [Astron. Rep. **41**, 821 (1997)].
15. V. I. Khaneĭchuk, Astron. Zh. **76**, 385 (1999) [Astron. Rep. **43**, 330 (1999)].
16. M. M. Katsova and M. A. Livshits, in *The Eleventh Cambridge Workshop on Cool Stars, Stellar Systems and the Sun, Tenerife, 1999*, Ed. by M. R. Zapatero Osorio, R. García López, and R. Rebolo (in press).
17. D. N. Brown and M. A. Landstreet, Astrophys. J. **246**, 899 (1981).
18. E. F. Borra, G. Edwards, and M. Mayor, Astrophys. J. **284**, 211 (1984).
19. S. Hubrig, S. I. Plachinda, M. Hunsch, and K. P. Schroder, Astron. Astrophys. **291**, 890 (1994).
20. S. I. Plachinda and T. N. Tarasova, Astrophys. J. **514**, 402 (1999).
21. S. I. Plachinda and T. N. Tarasova, Astrophys. J. **533**, 1016 (2000).
22. C. R. Cowley, in *Model Atmospheres and Spectrum Synthesis*, Ed. by S. J. Adelman, F. Kupka, and W. W. Weiss (ASP, San Francisco, 1996), p. 170.
23. V. V. Tsymbal, private communication (1999).
24. F. Kupka, N. E. Piskunov, T. A. Ryabchikova, *et al.*, Astron. Astrophys., Suppl. Ser. **138**, 119 (1999).
25. J. M. Beckers, *A Table of Zeeman Multiplets*, Phys. Sci. Res. (Sacramento Peak Observatory, 1969), Paper 371.
26. R. W. Noyes, L. W. Hartmann, S. L. Baliunas, *et al.*, Astrophys. J. **279**, 763 (1984).
27. S. L. Baliunas, D. Sokoloff, and W. H. Soon, Astrophys. J. Lett. **457**, L99 (1996).
28. A. Hempelmann, J. H. M. M. Schmitt, and K. Stepien, Astron. Astrophys. **305**, 284 (1996).
29. K. A. Strand, Publ. Astron. Soc. Pac. **55**, 28 (1943).
30. R. Wielen, Astron. J. **67**, 599 (1962).
31. D. L. Harris, K. Aa. Strand, and C. E. Worley, *Basic Astronomical Data*, Ed. by K. Aa. Strand (Univ. of Chicago Press, Chicago, 1963), p. 273.
32. D. F. Gray, S. L. Baliunas, G. W. Lockwood, and B. A. Skiff, Astrophys. J. **465**, 945 (1996).
33. A. W. Irwin, S. Yang, and G. A. H. Walker, Publ. Astron. Soc. Pac. **104**, 101 (1992).
34. D. K. Duncan, Astrophys. J. **248**, 651 (1981).
35. R. A. Donahue, S. H. Saar, and S. L. Baliunas, Astrophys. J. **466**, 384 (1996).
36. D. F. Gray and S. L. Baliunas, Astrophys. J. **441**, 436 (1995).
37. A. C. Danks and D. L. Lambert, Astron. Astrophys. **148**, 293 (1985).
38. G. W. Marcy, Astrophys. J. **276**, 286 (1984).
39. I. S. Savanov and Yu. Yu. Savel'eva, Astrofizika **39**, 5 (1996).
40. J. Pelt, *Irregularly Spaced Data Analysis* (Univ. of Helsinki, Helsinki, 1992).
41. E. W. Burke, W. W. Rolland, and W. R. Boy, J. R. Astron. Soc. Can. **64**, 353 (1970).
42. M. H. Hunsch, J. H. M. M. Schmitt, M. F. Sterzik, and W. Voges, Astron. Astrophys., Suppl. Ser. **135**, 319 (1999).
43. D. Dravins, P. Linde, T. R. Ayres, *et al.*, Astrophys. J. **403**, 412 (1993).
44. R. A. Donahue, Ph.D. Thesis (1993).
45. S. H. Saar, in *Stellar Surface Structure (IAU Symposium 176)*, Ed. by K. G. Strassmeier and J. L. Linsky (Kluwer, Dordrecht, 1996), p. 237.

Translated by Yu. Dumin

Astronomy Reports, Vol. 45, No. 6, 2001, pp. 482–496. Translated from Astronomicheskiĭ Zhurnal, Vol. 78, No. 6, 2001, pp. 558–574.

The Flux Deficits in Star Spots

I. Yu. Alekseev[1], R. E. Gershberg[1], M. M. Katsova[2], and M. A. Livshits[3]

[1]*Crimean Astrophysical Observatory, p/o Nauchnyĭ, Crimea, Ukraine*

[2]*Sternberg Astronomical Institute, Universitetskiĭ pr. 13, Moscow, 119899 Russia*

[3]*Institute of Terrestrial Magnetism, the Ionosphere, and Radio-Wave Propagation, Troitsk, Russia*

Received October 10, 2000

Abstract—The bolometric flux deficits of the photospheres of spotted stars are derived for the first time in the framework of zonal spottedness models for red dwarfs computed at the Crimean Astrophysical Observatory. The resulting flux deficits are compared to the estimated radiative losses from the chromospheres and coronas measured during quasi-simultaneous observations. A linear correlation is found between the logarithms of these quantities, with the Sun fitting these relations. Radiative losses from the outer stellar atmospheres in quiescence and during individual sporadic flares are significantly lower than the bolometric deficits of the spotted photospheres of active stars. This suggests that the flux deficit due to spots leads to global reconstruction of the atmospheres of red dwarfs, analogous to the local atmospheric reconstruction that occurs during solar and stellar flares. This process may be realized via the superposition of a large number of weak impulsive flares and other dynamic events, which develop on these stars and heat their coronas (i.e., in this view, microflaring is favored as the principal coronal heating mechanism for these stars). A brief analysis of the long-term variations in the chromospheric and photospheric radiation of F–K stars from the HK project and of the Sun suggests that such dynamical reconstruction of the outer atmosphere by energy associated with the flux deficit of the spotted photosphere occurs at times of increased surface activity in all F–M stars. © *2001 MAIK "Nauka/Interperiodica"*.

1. INTRODUCTION

The problem of sunspot flux deficits is now one of the most topical issues in solar–terrestrial physics. Currently, there is no consensus about the answer to a simple question: where does the energy "underradiated" by the Sun due to the appearance of dark spots on its surface go? The corresponding flux deficit per unit sunspot area is rather large—about 40% of the photospheric flux. Generally speaking, this missing energy could either fail to reach the photospheric level and remain inside the star, or spread across the surface, or be transported to the outer atmospheric layers.

Spruit [1] showed that, in the first hypothesis, the energy trapped in subphotospheric layers should heat the convection zone slightly. According to his estimates, this effect should produce no observable structural changes in the inner regions of the Sun. Currently published and future helioseismological data will enable clarification of whether or not the underradiated energy in spots is "reflected" downward.

In several models discussed about 30 years ago, the energy missing from the spot flows around the spot region and heats the adjoining photospheric area. Although direct enhancement of the superpenumbral optical flux proved to be insufficient to compensate for the spot energy deficit, the total flux of the superpenumbra and surrounding facular fields is close to the required level. Mullan [2] and Parker [3] suggested independently that the flux deficit is transported upward from the spots by Alfvén waves. However, later extra-atmospheric solar observations failed to support this hypothesis.

The problem becomes much more acute when we turn from the Sun, where spots account for a mere 0.5% of the total surface, to red dwarfs with spotted regions covering several tens of percent of their surface areas, for which the optical-radiation deficit can run as high as 30–40% of the total flux. Hartmann and Rosner [4] concluded that the observed flux deficits of spotted stellar atmospheres are not compensated by wavelength or spatial redistribution of energy and must be associated with slow variations of convective transfer.

Recently constructed homogeneous spottedness models for 24 dwarfs at more than 340 epochs can be used to compare the flux deficits of spotted stellar photospheres to the radiative losses of their atmospheres, based on a fairly extensive and homogeneous dataset. In this paper, we perform such a comparison using multiwavelength data obtained during only one observing season. We have computed the bolometric photospheric flux deficits $\Delta L_{\rm bol}$ for the first time, based on the *V*-band flux deficits derived for the spottedness models. The resulting $\Delta L_{\rm bol}$ values exceed substantially the radiative losses from all outer layers in the atmospheres of the most active stars. We suggest that this deficit goes into a global reconstruction of the stellar atmosphere, analogous to the local atmospheric reconstruction that occurs during solar flares. We discuss problems connected with the bolometric flux deficits in spotted stellar atmospheres covering a wide range of spectral types and different activity levels.

1063-7729/01/4506-0482$21.00

2. THE FLUX DEFICIT IN SPOTTED PHOTOSPHERES AND RADIATIVE LOSSES FROM THE CHROMOSPHERES AND CORONAS OF RED DWARFS

2.1. Bolometric Flux Deficit in Spotted Photospheres

The bolometric flux deficit of the photosphere due to spots ΔL_{bol} is determined by the relation

$$\Delta L_{bol} = (1 - \beta_{bol}) S L_{bol}, \quad (1)$$

where β_{bol} is the ratio of the integrated brightness of the spot to the brightness of the quiescent photosphere (the so-called bolometric spot contrast), S is the fraction of the stellar area covered by spots, and L_{bol} is the bolometric luminosity of the star. We derived these quantities from the results of a systematic analysis of red dwarfs in the framework of the zonal spottedness model developed by Alekseev and Gershberg [5, 6]. This model enables estimation of the total spot area and the *V*-band spot-to-photosphere surface brightness ratio from multicolor photoelectric observations and suggests a picture of stellar spottedness that is qualitatively similar to that observed on the Sun, with numerous spots at middle and low latitudes.

In a blackbody approximation, the spot-to-photosphere contrast at wavelength λ is

$$\beta_\lambda = B_\lambda(T_{spot})/B_\lambda(T_{phot}), \quad (2)$$

where $B_\lambda(T)$ is the Planck function. We therefore have for the *V* band

$$T_{spot} = 26\,200/\ln(1 + (\exp(26\,200/T_{phot}) - 1)/\beta_V). \quad (3)$$

The spot-to-quiescent-photosphere bolometric brightness ratio in the same approximation is

$$\beta_{bol} = (T_{spot}/T_{phot})^4. \quad (4)$$

We derived T_{phot} from the *V–R* and *V–I* color indices using available calibrations, e.g., that of Johnson [7]. We estimated the bolometric luminosity L_{bol} from the absolute magnitude M_V, color indices, and bolometric correction when the star was at its brightest during the entire observing period. As in the spottedness modeling, we assumed that this brightest state represents a spot-free star.

Table 1 gives the following parameters for 24 red dwarfs and the Sun: photometric variability parameters, including the maximum amplitudes of rotational modulation ΔV and the amplitudes of seasonal variations of the mean brightness $\Delta\langle V\rangle$; the photospheric temperature T_{phot}; the maximum spot coverage S; the contrast β_V; the temperature difference between the photosphere and spots $\Delta T = T_{phot} - T_{spot}$; and the maximum ratios $\Delta L_{bol}/L_{bol}$ computed using formulas (1)–(4). It is evident that, in most cases, the flux deficit of the spotted photospheres is about ten percent of the total bolometric luminosity of the star and can reach 30% for the most heavily spotted stars. The absolute bolometric flux deficits ΔL_{bol} range from 3.2×10^{29} to 5.0×10^{32} erg/s for this sample of stars.

2.2 Radiation of the Outer Atmospheres of Red Dwarfs

We used the equivalent width of pure H_α emission as the principal parameter used to characterize the chromospheric emission. We followed the approach of Young *et al.* [8], who determine this quantity as the difference between the equivalent widths of the observed emission-line profiles and those of the corresponding absorption lines measured in the spectra of quiescent stars of the same spectral type. In most cases, the absorption equivalent widths can be estimated from the color index of the star [9]:

$$EW(H_\alpha)_{abs} = 0.62(R–I) - 1.19\ \text{Å}. \quad (5)$$

For VY Ari, LQ Hya, and MS Ser, we use the results of Alekseev and Kozlova [10, 11], who subtracted synthetic absorption-line profiles computed using model atmospheres [12–14] from the observed H_α profiles. The absorption-line equivalent widths determined in this way agree well with the estimates given by (5).

Table 1 lists all published measurements of the equivalent widths of pure H_α emission for our program stars. In our subsequent analysis, we used only data for epochs with spottedness estimates. Based on the absolute magnitudes of the program stars and their color indices at the observation epoch, we transformed the equivalent widths of pure H_α emission into absolute luminosities using the well-known calibration and the response curve of the Johnson *R* band [7]:

$$L(H_\alpha) = 2.1 \times 10^{31 - 0.4 M_R} EW(H_\alpha)\ \text{erg/s}, \quad (6)$$

where $M_R = M_V - (V–R)$. The total radiative losses from the stellar chromosphere L_{chr} can be estimated from the relation

$$L_{chr} = L(H_\alpha)/kl, \quad (7)$$

where k is the ratio of the H_α line flux to the total Balmer flux and l is the ratio of the Balmer emission to the total radiative losses. According to [15], H_α emits about 53% of the total chromospheric Balmer line emission of AD Leo. The Balmer decrements of flare stars vary little over a wide range of absolute magnitudes [16], and we accordingly take $k = 0.53$ to be typical of all the flare stars. Further [17], the contribution of the Balmer lines to the total radiative losses from the chromosphere depends on the spectral type and ranges from 13% for the Sun (dG2) to 77% for UV Cet (dM6e). We accordingly assigned a value for l to each of the program stars based on its spectral type. The resulting radiative losses L_{chr} are summarized in Table 1.

Our main coronal emission indicator was the soft x-ray luminosities of the program stars in their quiescent states. We derived these luminosities from EINSTEIN,

Table 1. Parameters of Zonal Spottedness Models

No.	Star	Sp	ΔV mag	$\langle\Delta V\rangle$ mag	T_{phot}, K	S, %	β_V	ΔT	$\Delta L_{bol}/L_{bol}$, %	EW(H_α), Å	$\log L_{chr}$ [erg/s]	$\log L_X$ [erg/s]
1	EK Dra	G0Ve	0.12	0.10	5870	27	0.07	2200	22.8			29.5–30.1
2	BE Cet	dG2e	0.04	0.02	5800	3.3	0.24	1400	2.2	0.023	29.3	28.7–29.1
3	VY Ari	dG9e	0.31	0.27	4860	41	0.13	1300	28.9	0.5–1.6	30.2–30.6	30.2–31.1
4	V775 Her	dK0e	0.15	0.43	4950	42	0.30	900	23.3	0.4–1.2	29.9–30.3	28.8–30.1
5	LQ Hya	dK0–2e	0.19	0.09	4800	27	0.46	600	11.0	0.5–1.2	29.7–30.1	29.1–29.9
6	V838 Cen	dK0–1p	0.10	0.11	4700	26	0.23	1000	16.3	0.9	30.3	29.9
7	AG Dor	dK2e	0.10	0.26	4800	18	0.12	1300	13.3			29.8
8	MS Ser	dK2e	0.15	0.18	4800	14	0.08	1500	10.9	0.5	29.9	29.5–30.7
9	OU Gem	dK3e	0.09	0.09	4700	12	0.07	1500	9.3	0.2–0.7	29.2–29.7	29.1–29.5
10	V833 Tau	dK5e	0.08	0.31	4450	48	0.22	900	28.8	0.7–1.3	29.5–29.6	29.6–29.9
11	EQ Vir	dK5(7)e	0.15	0.15	4250	14	0.10	1160	9.3	0.6 –1.7	29.4–29.7	29.1–29.6
12	BY Dra	dK6e(M0e)	0.20	0.38	4000	37	0.05	1250	29.0	0.8–1.5	29.6–30.1	29.4–29.8
13	CC Eri	dK7e	0.33	0.14	4000	33	0.06	1100	24.0	2.5–4.5	29.6–29.8	29.2–29.8
14	DK Leo	dM0e	0.13	0.20	4100	15	0.03	1500	12.7	1.5–1.7	29.9	29.1–29.2
15	V1005 Ori	dM0.5e	0.14	0.16	3580	11	0.07	930	8.0	1.4–4.7	29.2–29.3	28.9–29.6
16	BF CVn	dM1.5e	0.10	0.16	3500	15	0.03	1100	11.4	1.6–3.1	29.1 - 29.5	28.7–29.4
17	DT Vir	dM1.5e	0.07	0.14	3550	26	0.06	1000	18.8	1.8–3.7	29.0–29.4	29.0–29.4
18	AU Mic	dM2e	0.32	0.25	3730	17	0.07	1000	11.9	2.0–4.4	29.1–29.2	29.3–29.9
19	FK Aqr	dM2e	0.10	0.14	3600	17	0.08	900	11.3	1.2–2.5	29.1–29.2	29.1–29.8
20	V1396 Cyg	dM3e	0.10	0.11	3400	27	0.38	380	10.2	1.7–3.9	28.9–29.0	28.5–29.3
21	AD Leo	dM3.5e	0.04	0.04	3450	11	0.23	560	5.7	2.5–8.9	28.6–28.8	28.6–29.0
22	GT Peg	dM3.5e	0.13	0.14	3350	12	0.20	570	6.4	3.8–9.3	28.9–29.3	28.8–29.7
23	YZ CMi	dM4.5e	0.16	0.13	3300	21	0.32	420	8.7	4.4–14	28.3–28.6	28.2–28.6
24	EV Lac	dM4.5e	0.14	0.25	3300	27	0.50	250	7.2	2.8–7.2	28.3–28.6	28.5–29.4
	Sun	G2Ve			5785	0.01	0.04	2085	0.01	0.005	28.4	27.0–27.3

A full version of the table with references to H_α emission and x-ray data can be found on the Internet at the address http://www.crao.crimea.ua/~ilya.

ROSAT, EXOSAT, and ASCA data after reducing them to a single ROSAT PSPC system (see, e.g., [18, 19]). The nonflare x-ray luminosities based on all published data are listed in Table 1.

2.3. Comparison of Radiative Losses with Flux Deficit of Spotted Photospheres

Figures 1 and 2 compare the total radiative losses from the stellar chromospheres and coronas to the bolometric flux deficit ΔL_{bol} of the spotted photospheres for similar epochs. These figures show that there is a correlation between these quantities over three orders of magnitude in ΔL_{bol}, for ΔL_{bol} = 29.5–32.7. Our computations yield the correlations

$$\log L_{chr} = (0.70 \pm 0.03)\log\Delta L_{bol} + (7.6 \pm 0.9) \quad (8)$$

with the linear correlation coefficient $r(\log L_{chr}, \log\Delta L_{bol}) = 0.86 \pm 0.07$ and

$$\log L_X = (0.78 \pm 0.05)\log\Delta L_{bol} + (4.9 \pm 1.0) \quad (9)$$

with $r(\log L_X, \log\Delta L_{bol}) = 0.78 \pm 0.17$. The equivalent relations

$$\begin{aligned} L_{chr}/\Delta L_{bol} &= 10^{7.6\pm0.9}\Delta L_{bol}^{-0.30\pm0.03}, \\ L_X/\Delta L_{bol} &= 10^{4.9\pm1.0}\Delta L_{bol}^{-0.22\pm0.05} \end{aligned} \quad (10)$$

show that the ratios of chromospheric and coronal radiative losses to the flux deficit of the spotted photosphere decrease with the flux deficit and range from 6 to 0.6% and 5 to 0.5% for the chromospheric losses and x-ray coronal radiation, respectively, over the entire ΔL_{bol} interval considered. Finally, according to Shakhovskaya [21], the optical radiative losses due to stellar flares are close

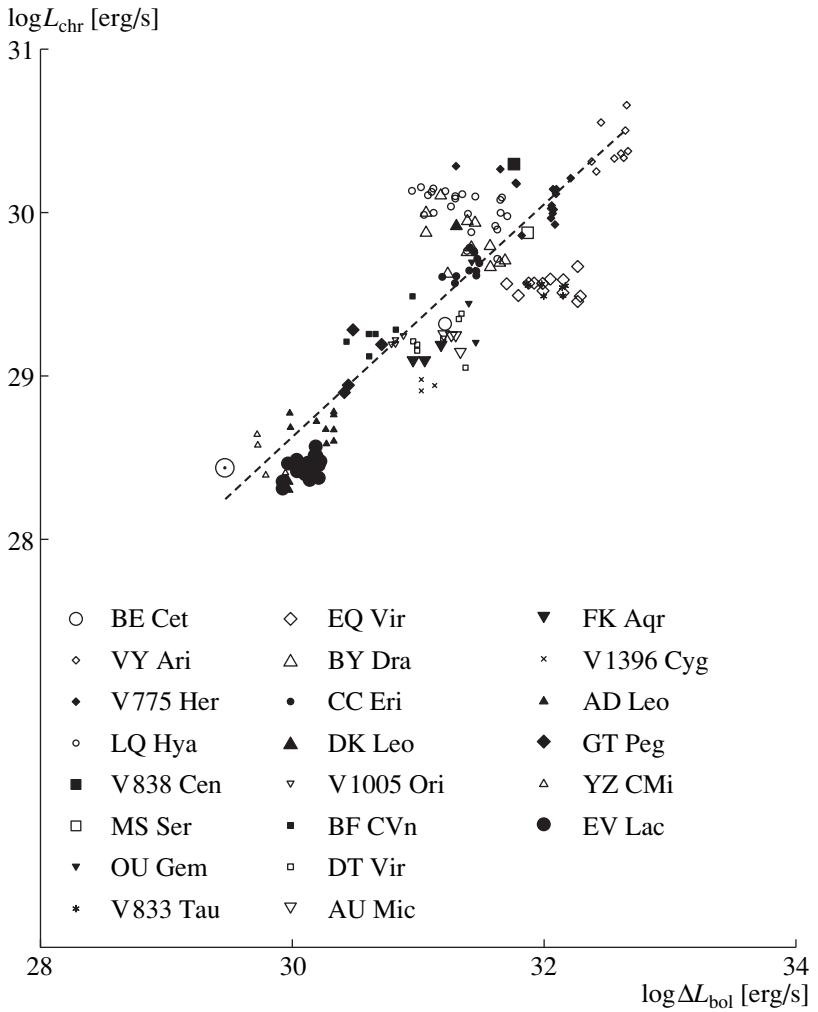

Fig. 1. Chromospheric radiation as a function of the bolometric flux deficit for spotted stellar atmospheres.

to one-quarter of the quiescent coronal radiation. Thus, the steady-state radiation of the outer atmospheres and radiative energy of sporadic flares in active stars fall far short of the flux deficit of their spotted photospheres.

The contributions of different layers of the outer atmospheres of red dwarfs to the radiative flux are known to vary appreciably with the overall activity level. The most general manifestations of this are nonlinear relations between the radiative losses of different layers of the stellar atmosphere [22–24]. For example, whereas the Sun, which is a star with fairly low activity, has $R_{chr} : R_{tr} : R_{cor} = 1 : 0.4 : 0.03$ and total $R = 0.003\%$ (here, R are the radiative losses from different atmospheric layers normalized to the bolometric luminosity), AU Mic, one of the most active stars, has $R_{chr} : R_{tr} : R_{cor} = 1 : 0.6 : 0.7$ and $R = 1\%$ [20]. In other words, the contribution of the coronal radiation increases rapidly with the total radiative losses. This also follows directly from a statistical analysis of the ratios of the H_α to soft x-ray luminosities for chromospherically active M dwarfs: Young *et al.* [8] found the average ratio for about three dozen such stars to be $L(H_\alpha)/L_X = 0.22$. Repeating the above conversion of H_α luminosity into the total chromospheric luminosity yields the ratio $\langle L_{chr}/L_X \rangle \sim 1$ for $\langle l(\mathrm{dMe}) \rangle = 0.50$, which is substantially below the corresponding ratio for the Sun but close to that for AU Mic. [A similar chromospheric-to-coronal luminosity ratio can also be inferred, albeit with much higher errors due to the large uncertainties in the coefficients, from relations (8) and (9).]

Thus, as the level of stellar activity increases, the radiation fluxes from different layers of the outer atmospheres of active red dwarfs become comparable. Clearly, such major changes in the radiation properties must be the result of substantial structural changes in the outer atmospheres. We believe that this reconstruction of the stellar atmosphere with increasing activity is due to the development of dynamical processes associated with the emergence and evolution of magnetic fields with complex configurations.

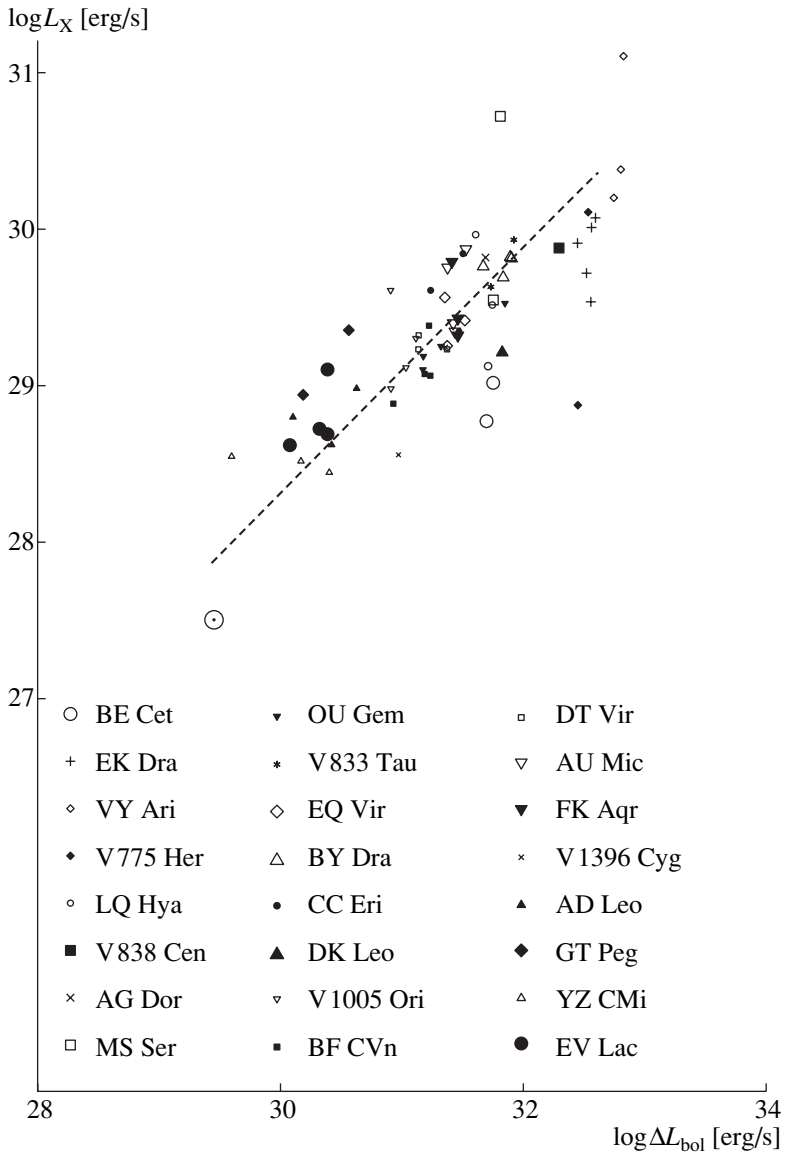

Fig. 2. X-ray radiation of stellar coronas as a function of the bolometric flux deficit for stellar photospheres.

3. SPOTS AND DYNAMICAL PROCESSES ON THE SURFACES OF RED DWARFS

In the next two sections, we propose the new idea that the spot flux deficit is redistributed over adjacent photospheric regions (forming bright facular grains and strengthening the chromospheric network) and the uncompensated part of the energy flux goes into global reconstruction of the outer atmosphere of the active star. In other words, the emergence of a large number of spots triggers an entire set of dynamical processes, resulting in a redistribution of the density throughout the outer atmosphere, the formation of high-temperature coronal loops, and an enhancement of motions in all layers, including coronal plasma outflows (the stellar wind). In the case of some heavily spotted dwarfs, this reduces to the hypothesis that the flux deficits of their spotted photospheres go into a global reconstruction of their outer atmospheres, analogous to the local reconstructions that occur during flares. In this section, we present a number of arguments supporting this hypothesis as applied to red dwarfs.

First and foremost, we should recall a number of recent results of solar-atmospheric studies. The emergence of local magnetic fields on the solar surface is known to give rise to an entire series of events that transform the quiescent outer atmosphere into an active state, characterized by increased chromospheric density and the development of coronal condensations, i.e., concentrations of loops filled with dense and sometimes hot plasma. Flares interrupt the smooth evolution of local magnetic fields.

Continuous soft x-ray monitoring of the Sun with a spatial resolution of 2.5″ revealed, in addition to the usual flares detected in the signal for the entire Sun, numerous dynamical events, mostly x-ray jets [25]. The corresponding processes are characterized by a wide range of powers, sizes, and durations for individual events, the most powerful of which are detected by the Solar Service as subflares. Most of these processes develop inside or very near active regions, although a considerable number of weak events develop in more quiescent regions, such as adjacent to or inside coronal holes (bright x-ray points, ephemeral active regions). The occurrence rate of these events, including events such as flashes, appreciably exceeds the rate of common subflares [26].

Here, we indicate two possible mechanisms that could be responsible for the development of numerous solar subflares. The first is associated with variations of the magnetic field of a spot, which occur, for example, during its formation or disruption. An appreciable number of subflares [27] and many Ellerman bombs [28] are observed even in the penumbrae of stationary spots. The second mechanism operates when a neutral line of the longitudinal magnetic field crosses the active region in a very complex manner, especially in the case of a δ-configuration magnetic field with umbrae of opposite polarities located within a common penumbra. This leads to numerous brightenings of low coronal loops (subflares) in the immediate vicinity of the neutral line; after several hours or even days, this dynamic activity often ends in one or several large flares, resulting in a simplification of the magnetic-field configuration. A number of such episodes were observed on the Sun in August 1972, June 1991, and at other times. The events observed in June 2000 have a similar nature. Thus, the development of the most powerful spot groups—activity complexes—is accompanied by both the most powerful flares and a substantial increase in the occurrence rate of weak dynamical phenomena. This is in agreement with the result of Kasinsky and Sotnikova [29], who found a well-defined correlation between the spectral index of solar x-ray flares and the Wolf number: during periods of minimum activity, the spectral indices are appreciably less than unity, so that rare and powerful flares dominate, while, during periods of maximum activity, they are close to unity, indicating an increased contribution of numerous weak flares (here and below, we use the "integrated" spectral index β; i.e., we consider the total number of flares per unit time with energies exceeding a given level).

Can this solar situation be extrapolated to active red dwarfs? Since the spot coverage for such stars can exceed the corresponding solar values by factors of several tens or several hundred, the mechanisms described above should operate in a continuous rather than discrete fashion. Of course, in many dwarfs, this is manifest as an increase of the flare rate over that for the Sun. However, although the term "dynamical sun" is often used in the post-Yohkoh era, the level of development of weak, nonstationary phenomena on red dwarfs should be appreciably higher. As a result, the exponent of the power-law dependence of the energies of nonstationary phenomena on their occurrence rates might differ substantially from the exponents for usual flares at energies corresponding to weak events. In addition, according to [30], the theory of current sheets predicts a power-law spectrum with the index $\simeq 0.75$, as is observed for flares, while the spectrum should become softer at lower energies; i.e., the contribution of microflares should be higher than estimated using the spectral index found from individual detections of flares.

Usually, the atmospheric state of an active red dwarf is described using quasi-stationary models. However, in this case, there are two observational facts, probably associated with weak dynamical processes, that lead to changes in the relative contributions of the radiation fluxes from the chromosphere, transition region, and corona. The first implication of the models of [31] is that the dense coronas of active red dwarfs begin at low altitudes, at large Lagrangian coordinates m, defined as the column density of gas integrated from the outer coronal layers down to the coronal base. The typical value of m for flare stars is $\log m \approx -3$, in contrast to the value $\log m \approx -6$ for solar-type stars. The chromospheres of active red dwarfs develop a so-called "temperature plateau" [32]. The typical electron densities in the chromospheres of active dwarfs are an order of magnitude higher than in the solar chromosphere and close to the densities of solar flares [33].

The second implication is associated with the fact that active stars have a persistent, hot, coronal-plasma component whose temperature ranges from 6 to 15 MK, which, in the case of the Sun, is detected only during flares. This was first established by EXOSAT observations and has been confirmed in multiple studies since then [34].

Note also that active stars are sources of quasi-stationary radio emission generated by relativistic electrons moving in magnetic fields. The short lifetimes of these particles in the stellar atmospheres require the action of virtually continuous flare processes accelerating these particles [35].

These considerations lead us to conclude that the structure of the outer atmosphere of a red dwarf should change substantially when its activity increases, even in the absence of well-defined flares. This reconstruction of the outer atmosphere is most likely associated with the collective effect of a large number of very weak flares. The corresponding transformation of the outer atmosphere by impulsive flares is already fairly well understood.

Changes of the atmospheric structure due to impulsive thermal fluxes or accelerated particles are referred to as the standard response to heating (see, e.g., [36, 37]). Very rapid heating of the outer chromosphere generates two disturbances propagating upward and downward,

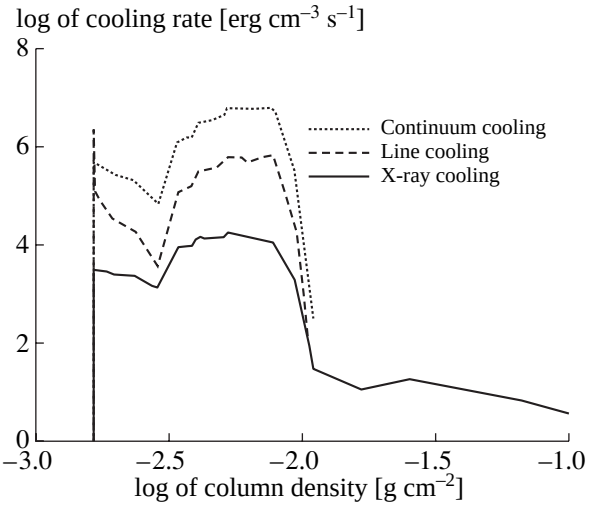

Fig. 3. Radiative losses for the H_α, Ca II H, and optical continuum emission as functions of the heating due to x-ray absorption in the low-temperature condensation that was the source of the optical radiation of the impulsive flare of AD Leo. The horizontal axis plots the Lagrangian mass coordinates ($\log m$). A 20-km thick source is located at a height of 250 km above the photosphere [41].

away from the resulting region of high pressure. The temperature jump then slowly drifts downward, and a shock develops in front of it. The gas behind the downward-propagating shock front filled with radiation is compressed by factors of several tens, and a geometrically thin, low-temperature condensation forms between the fronts of the shock and thermal wave; this condensation is the source of optical radiation in rapid flares. Hot gas flows upward from the region of the temperature jump, filling a coronal loop with dense plasma heated to temperatures above 10 MK. This lowering of the corona during flares is supported by empirical models, in which the flaring chromosphere is dense and geometrically thick [38], so that the corona descends to low altitudes.

The corresponding numerical simulations have been used many times in the interpretation of data on impulsive solar and stellar flares, and the main conclusions have been confirmed by observations (see, e.g., review [39]). However, usual flare computations apply to heat flows exceeding 10^{11} erg cm^{-2} s^{-1}. In a number of cases, weak heat flows of the order of 10^{10} erg cm^{-2} s^{-1} also result in the development of a low-temperature chromospheric condensation and the efficient evaporation of hot gas [40]. Thus, overall, the changes in the outer atmosphere of a red dwarf as its activity level increases are similar to those occurring during flare processes.

In gas-dynamical computations, the total energy of a flare does not consist only of its radiative energy. Moreover, if an impulsive flare is accompanied by the emergence of an optical continuum—as is true of most stellar flares with medium and high powers—the energy emitted by the flare continues to make up only a small fraction of the total energy of the process, despite the abrupt increase in radiative losses. This is illustrated by the results of gas-dynamical modeling [37] of an elementary impulsive event and its associated radiation [41]. Figure 3 shows the energy losses in the optical continuum, the Balmer lines, and the H and K lines of Ca II four seconds after the onset of the flare. The distribution is shown only for the height interval in the red-dwarf atmosphere corresponding to the source of the optical flare emission [41]. This figure characterizes the relative contributions of the continuum and line emission. The energy released as a result of the absorption of soft flare x-rays is also shown. This absorption occurs not at the bases of magnetic loops, but in a "halo" whose area exceeds that of the main source of the optical continuum—the low-temperature condensation. Experience with these computations shows that, if some nonstationary process is accompanied by the appearance of an optical continuum, the power of the entire event should be a factor of 5–10 higher than the power of the radiation of the condensation and "halo."

Perhaps the best evidence for this is provided by the following estimate. In the case of rapid flares, multichannel photometry or the spectral energy distribution in the optical continuum can be used to determine the temperature of the emission region on the star, which, in turn, provides the best estimate of the flare area. We have applied this procedure carefully in [42] and a number of later papers. The areas of white-light emission in rapid events are of the order of $(3–5) \times 10^{17}$ cm^2. The areas of optical emission for the most powerful flares can be an order of magnitude higher (see, e.g., the results for EV Lac reported in [43]).

Gas-dynamical modeling of the flare process enables derivation of the energy flux injected into the chromosphere, which, given an estimate of the flare area, yields the power of the entire process. For example, our recent gas-dynamical simulations of a flare on UV Cet (similar to those in [37]) with a duration of 2.5 min in the *B* filter are in agreement with the observations of [44] if the electron flux entering the chromosphere is 3×10^{11} erg cm^{-2} s^{-1}. This flare was somewhat hotter than usual, and its area was estimated to be 3×10^{17} cm^2, implying that the power of the accelerated electrons, which is close that of the entire process, should be about 10^{29} erg/s; the power of the optical emission of this flare was 2×10^{28} erg/s. It follows that, in the case of rapid events, the energy of the entire process is a factor a few higher than that of the optical emission. This coincides with the assertion made above, and this can now be used as a test of the results of gas-dynamical simulations of impulsive flares and their optical emission.

Returning to the problem featured in the title of this paper, a parallel growth of the flux deficits of spotted photospheres and of the degree of excitation in their upper atmospheres could come about due to a redistribution of the energy associated with the flux deficit to

the outer atmosphere, either directly or via some intermediate process associated with stellar spots. The first possibility returns us to the idea of Mullan [2] mentioned above. This model could be feasible due to the higher densities of the outer atmospheres of active stars and the possible development of resonance and nonlinear effects [45–47]. However, thus far there is no direct observational evidence indicating that such models are applicable to the Sun or red dwarfs.

The second hypothesis supposes a connection between powerful flare activity and heavy spotting. The energies of flares on red dwarfs are known to be four orders of magnitude higher than those of solar flares [47]. Nevertheless, as noted above, the flare energy is insufficient to channel the entire radiative energy deficit of the spotted photosphere. However, this statement can now be placed in doubt.

Beginning with Butler and Rodono [48], a number of researchers have discussed the possible role of microflares in the heating of stellar coronas and it has even been suggested that the observed coronal emission could be a superposition of such microflares. On the other hand, detailed analyses of EXOSAT x-ray data by Collura *et al.* [49] and then Pallavicini *et al.* [50] failed to confirm the dominant contribution of microflares. This problem remains unsolved due to the limited information provided by subsequent data, including those obtained with the ROSAT satellite.

Here, again, we note that extrapolations of power-law flare energy spectra to hypothetical microflares with similar exponents as those derived from individually detected optical or x-ray events (0.7–0.9) imply that microflares make a small contribution to the total flare emission. However, as noted above, even in the solar case, there is observational and theoretical evidence that the spectra of microflares are softer than those of more powerful events. Therefore, even on the Sun, the contribution of microflares should be higher than implied by a power-law spectrum with a constant index extrapolated over the entire range of flare energies. Finally, recent data suggest that microflares are instrumental in active processes on late-type stars. According to EUVE data for 28 flares of the active solar analogs 47 Cas and EK Dra, $\beta = 1.2 \pm 0.2$ in the energy interval 3×10^{33}–6×10^{34}erg [51]. A more detailed analysis of EUVE data for F–M type stars led Audard *et al.* [52] to conclude that $\beta > 1$ for flares with $E > 10^{32}$ erg for F–G dwarfs, whereas it is most likely that $\beta < 1$ for K–M stars.

Taken together, these considerations make the hypothesis of global reconstruction of the upper atmospheres of active red dwarfs powered by the flux deficit of their spotted atmospheres appear very plausible. Microflaring seems to be the most likely mechanism for such reconstruction in the case of flare stars.

4. THE LONG-TERM PHOTOSPHERIC AND CHROMOSPHERIC VARIATIONS OF ACTIVE F–K STARS

In the previous section, we proposed that the entire energy of the flux deficit attributable to spots goes into global reconstruction of the outer atmosphere. This hypothesis applies to heavily spotted red dwarfs. The question now naturally arises of how this problem can be solved for red dwarfs with lower spot coverages and active F–K stars. Approaching the issue from a somewhat broader perspective, we can formulate this question as follows: how general is this hypothesis, and what is the most likely mechanism for converting the flux deficit into other energy forms on active F–G stars?

A preliminary analysis of this problem is possible even with the observational data already available. In addition to solar data, these include the results of the HK project of Wilson on 11 F–K stars whose chromospheric emission has been monitored since the middle of the 1960s, as well as high-accuracy, photometric optical continuum monitoring carried out during the last decade. Here, we use the data reported by Radick *et al.* [53], who also give a number of references to earlier studies. Fortunately, this program had two stars in common with the sample considered in the previous section; a number of other common stars were analyzed by Alekseev [54].

We will use the well-known fact that, within a certain interval of spectral types, the activity of stars is determined by the velocities of their axial rotation. The rotational velocities of single stars depend on their age, whereas the axial rotation of active components in binaries is determined as well by the interaction between the orbital and axial angular momenta. Active late-type stars tend to group around two chromospheric-activity levels. This phenomenon was first noticed by Vaughan and Preston [55] back in 1980 and has since been confirmed repeatedly [56, 57].

This dichotomy in levels of chromospheric activity can already be seen in [53], which presents an analysis of Strömgren *b* and *y* photometry with accuracy 0.001^m obtained over the last ten years together with chromospheric emission data. These data allowed Radick *et al.* [53] to investigate long-term variations of the photospheric and chromospheric emission. High levels of chromospheric emission are found mainly in rapidly rotating, young stars, whereas low chromospheric emission is found in more slowly rotating, older stars, including the Sun. Note that the best-defined dependence of the spectrum of the coronal emission on age is shown in the results of Güdel *et al.* [58] for G stars.

We now discuss, first and foremost, the long-term variations of the photospheric and chromospheric emission of the Sun and F–K stars of the HK project. Figure 4 shows variations of the solar chromospheric and photospheric emission during the past two 11-year cycles [59, 60]. We can see that the solar luminosity increases by 0.2% during the activity maximum and that the solar

constant varies synchronously with the chromospheric emission on time scales of one year and longer. The chromospheric emission varies synchronously with the area of chromospheric faculae—flocculi observed in H_α, the Ca II H and K lines, and others. An analysis indicates that the long-term variations of the solar constant are physically due to variations of the photospheric facular area. Only during rare periods—especially in the declining phase of the activity cycle, when giant spot groups appear on the solar disk—does the solar constant decrease by 0.1–0.3%. While variations of the solar constant within the activity cycle are correlated with those of facular area, in most active K stars, periods of heavy spottedness bring about a decrease in the total stellar flux.

Radick *et al.* [53] performed a formal statistical analysis of all available observations of the HK-project stars collected over a single ten-year period when the stars were monitored in spectral lines and the continuum. They focused on differences in the levels of chromospheric activity, paying much less attention to the shapes of the corresponding continuum and Ca II-line flux curves. In their Fig. 8a, Radick *et al.* [53] indicate for each star error bars for the corresponding correlation coefficients p. The signs of p indicate that most stars with low chromospheric activity, including the Sun, exhibit correlated $\Delta(b+y)/2$ and ΔS variations, where S is proportional to the equivalent widths of the Ca II H and K lines; in contrast, variations of these quantities are anticorrelated in stars with strong activity (see Fig. 5, which illustrates these two types of long-term behavior). However, this approach depends strongly on the influence of rotational modulation in the white light and spectral lines. Therefore, we repeated the correlation analysis using the mean light curves shown in Fig. 3 in [53] for all 34 stars. Our analysis yielded the same signs of p in cases where Radick *et al.* [53] had found strong correlations, whereas the results were very discrepant in cases of weak correlation. This enabled a more correct division of the star sample studied in [53] into two groups: objects in which the long-term variations of their photospheric and chromospheric emission are similar to those observed on the Sun and objects in which they are opposite. Table 2 lists stars for which our analysis yielded trustworthy results. Only one star in Table 2 (61 Cyg = HD 201091) fell in a different group than that assigned by Radick *et al.* [53]. The cases of low correlation are distributed more or less equally among the two groups, and no analysis could be performed for three of the 34 stars.

The last column of Table 2 gives the type of long-term variability based on the extent to which the cycle is clearly defined (Excellent, Good, Fair, Poor) and the period in years according to [61]. We use the notation "Var" (Variable) to indicate cases where long-term variability was present in the Ca II lines in the absence of cyclicity and "Long" if the variability time scale exceeded 20 years. "Flat" indicates the absence of long-term variations. Table 2 also gives data on two HK-project stars (EP Eri and DX Leo) not included in [53].

In stars in the second group, which show stronger chromospheric activity, the long-term variations of photospheric emission are due to spots, whereas, in stars in the first group, these variations are associated with the compensation of the flux deficit and the dominant contribution of photospheric faculae. Active red dwarfs represent an extension of the second group, taking into account specific features due to the later spectral types of some of these stars. However, if a particular red dwarf exhibits very low activity, and especially if there are no Balmer lines in its spectrum, it can easily end up in the group of less active objects.

In this sense, it is of interest to analyze two stars with very different activity levels that are common to both the HK project and our Table 1—HD 1835 = BE Cet and HD 129333 = EK Dra. EK Dra (G0 V), with a rotation period of P_{rot} = 2.7 days, is the most chromospherically active object in the sample. Its spot coverage is 27%; the amplitude of long-term variations EK Dra is $\Delta\langle V\rangle = 0\overset{m}{.}10$, whereas that of BE Cet is $0\overset{m}{.}02$. The long-term variations in the chromospheric activity of EK Dra are irregular and chaotic, which is probably the origin of the fact that the anticorrelation discussed above, although present, is not well-defined.

BE Cet is a more quiescent star (G2 V), with only 3.3% of its surface covered by spots. Accordingly, only 2.2% of its bolometric luminosity in spots L_{bol} emerges in the form of photospheric emission. The star rotates more slowly than EK Dra (P_{rot} = 7.65 days); however, the long-term variations in its photospheric and chromospheric brightness are still anticorrelated (Fig. 5). Cyclic variations in the Ca II lines are poorly defined, especially during the years 1965–1985, although they become more conspicuous in the years 1985–1995 (Fig. 4). According to [61], in the years 1965–1995, the star exhibited weakly cyclic long-term variations with a period of 9.1 ± 0.3 years. EK Dra and BE Cet proved to be at the two extreme ends of the group of F7 V–G3 V stars showing nonsolar (i.e., spot-dominated) long-term variations.

In addition to these two objects, the group of BY Dra variables and candidate objects include a number of other HK-project stars. Some of the corresponding data are also given in Table 2. Five stars exhibiting relatively strong chromospheric activity belong to the group of stars with nonsolar long-term variations. V 2292 Oph shows the highest anticorrelation among all the stars considered. The variations in ξ Boo and V 2133 Oph are also anticorrelated, but weakly. Note that ξ Boo and V 2133 Oph have ratios of $\Delta(b+y)/2$ to ΔS equal to –0.22 and –0.45, respectively, as is also characteristic of this group (see also Fig. 9 in [53]). With their fairly strong chromospheric activity and rapid rotation, EP Eri and DX Leo can also be assigned to this group, although no direct comparisons of their long-term chromospheric and photospheric emission variations have been made. Note that the amplitude of the brightness variations in these stars is lower than in V 2133 and

V 2292 Oph, which have similar spectral types and show well-defined anticorrelations.

Thus, stars belonging to the two groups differ in two aspects. First, it is evident that stars in the second group rotate more rapidly than those in the first group. It goes without saying that this applies for stars of similar spectral types. For example, G stars in the group with anticorrelated chromospheric and photospheric variations have rotational periods ranging from two to four days; as noted above, the rotational period of BE Cet (G2 V) is $P_{rot} = 7.65$ days and the periods of stars in the group with correlated variations range from 25 to 40 days. It is obvious that this difference in period is directly related to the higher levels of surface activity in the second group of stars.

The second difference turned out to be far from trivial. The overwhelming majority of stars in the first group, including the Sun, exhibit well-defined activity cycles, as is evident from Table 2. Moreover, many stars in the first group have cycles classified "Excellent" according to [61]. There is the impression that, as a star becomes older, not only does its strong and often irregular activity pattern evolve into cyclic behavior, but also its flux deficit begins to be nearly compensated; i.e., the star moves from the second to the first activity group. There are exceptions to this pattern: for example, the second group includes HD 152391, which shows well-defined activity cycles, and HD 149661, which has periodic chromospheric variations (although with a time-dependent period). The Sun has the highest chromospheric activity among stars in the first group (i.e., those with cyclic behavior), in spite of its weak x-ray flux. These problems are worthy of further investigation.

One of the most important recent results is the reliable determination of variations in the solar constant over the past two 11-year activity cycles [59, 60] (Fig. 4), which are very small. Variations in the total solar flux range from several tenths of a percent to several percent in the ultraviolet from 2000–4000 Å and are only 0.1% in the optical and near infrared (see, e.g., Fig. 7 in [62]). In other words, an important feature of solar radiation is that the optical radiation of dark regions (spots) is almost without exception compensated rather accurately by that of brighter regions (photospheric faculae). Three extra-atmospheric missions—ACRIM, ERB, and VIRGO (SoHO)—not only detected variations in the solar constant on various time intervals, but also revealed connections between these variations and activity processes. Accurate models of these relations include three sources of variations: bright points of photospheric faculae; the bright photospheric network, enhanced in regions of activity, and dark spots. We will combine the two sources of bright elements under the name "photospheric faculae"; i.e., we use the contrast of an "average" facula rather than that of the bright spots in a facula. This is sometimes referred to as a two-component (faculae + spots) model.

Schatten [63] suggested that the relatively small variations of the solar constant are due to the fact that an observer on Earth views the Sun virtually along its equator; i.e., the angle between the solar rotational axis and the line of sight is very close to 90°. If this angle differed from 90°, the amplitude of the variations of the solar constant would increase by a factor of four to five, according to [63]. However, this strong effect turned out to be due to the unrealistic ratio of the total flux of the faculae to that of the spots adopted in [63], and Unruh *et al.* [64] showed the actual effect of the viewing angle to be rather weak. It is important for our subsequent analysis that the effect of spots on the total solar radiation varies by approximately a factor of three as the angle between the line of sight and the rotational axis changes from 90° to 0°.

Our view concerning the origin of the observed virtually complete mutual compensation of spots and faculae that is the underlying cause of the low amplitude of variations in the solar constant is the following. In the simplest model, these variations are due to chance combinations of the contrasts and relative areas of spots and faculae. However, it is more likely that bright and dark photospheric formations are associated in such a way that the energy of the flux deficit of a spot is redistributed throughout the active region. If the photospheric facular contrast is limited for some reason, compensation of the flux deficit in spots is possible as long as the spot coverage of the active region remains low enough.

If we consider the Sun as a late-type star with low activity, we see that only a relatively small fraction of the energy of nuclear reactions produced near the solar center is processed into magnetic-field energy in deep layers of the convection zone. During the maximum of the activity cycle, the corresponding magnetic-field tubes are efficiently buoyed upward, carrying some excess energy with them into the photosphere. This corresponds to a small increase in the total optical emission of an entire single active region; the excess of the flux of faculae over that of spots in this region accounts for only a small fraction of the integrated flux. Accurate determinations of the solar constant itself indicate that the primary energy indeed accumulates in the form of magnetic energy and is carried to the surface. If normalized to a single active region, this energy is about 2×10^{-4} of the solar bolometric luminosity. Although it is fairly high, this energy is within the limits typical of the dynamical phenomena observed in the outer atmospheres of late-type stars. We therefore believe that the hypothesis that the optical flux deficit of spots is redistributed throughout adjacent facular fields can be reasonably applied not only to the Sun but also to other solar-type stars displaying low levels of activity.

In stars in the low-activity group identified above, the photospheric emission varies in phase with the chromospheric emission on time scales from several years to several decades. As on the Sun, faculae and

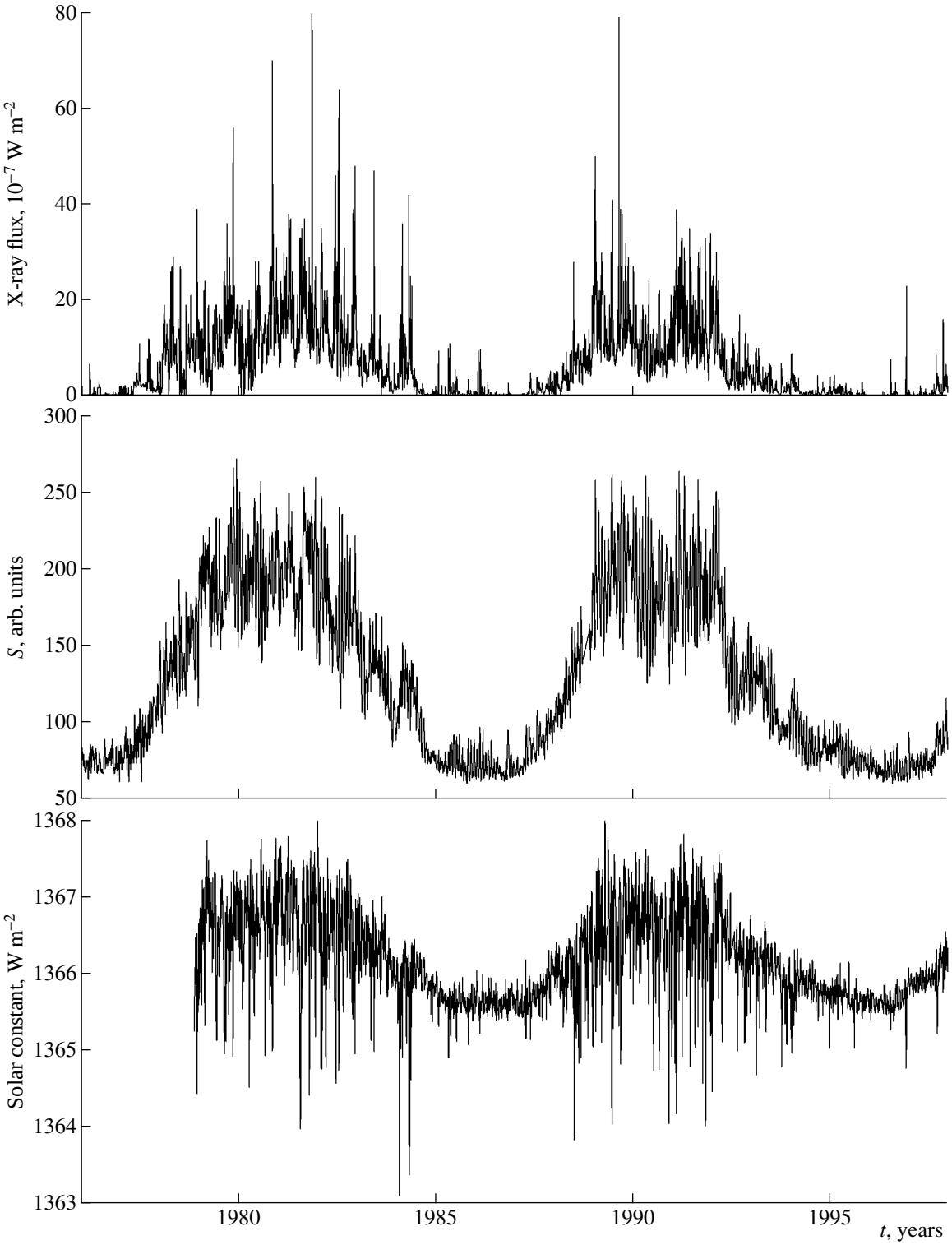

Fig. 4. Variations of solar x-ray emission according to GOES data (1–8 Å), chromospheric-activity index S based on Ca II and Mg II lines, and the solar constant from 1976 through 1997. Data provided by J. Lean [60].

spots balance each other and uncompensated weak variations of the total flux are due to faculae. In this case, the spot flux deficit is redistributed throughout the entire area of the active region. Only a small fraction of this deficit is used to change the physical conditions in the chromospheres, transition regions, and coronas of the Sun and solar-type stars of this group. Note that all this occurs on stars with low spot coverages.

The second group of stars, showing strong activity, consists of relatively young F and G stars and active K and M dwarfs. The surfaces of these objects are heavily spotted, and their long-term flux variations are due to the spots. These stars have their chromospheric emission peak during periods of high spottedness and, consequently, of decreased optical flux. These relative variations in the bolometric luminosity become important in active red dwarfs.

The inferred values of the stellar spot flux deficit and total energies emitted by the chromosphere and corona have led us to put forward the general hypothesis that the flux deficit goes into dynamical processes that bring about substantial reconstruction of the outer stellar atmospheres. It is relatively straightforward to identify the origin of the overall levels of surface activity in some active F–G stars. Here, age is an important factor. At the same time, the specific mechanism converting the photospheric flux deficit into energy powering dynamical processes in the outer atmosphere remains unclear. It is, however, evident that the formation of hot plasma clouds with temperatures above 10 MK, detected in the coronas of young stars, requires energies appreciably exceeding the x-ray energy of these stars. There is some circumstantial evidence—prolonged soft x-ray flares and the presence of radio emission—suggesting possible large-scale dynamical events in the coronas of young F–G stars. Such events could develop in the global or large-scale fields of these stars.

Thus, numerous nonstationary phenomena on red dwarfs are capable of bringing about important structural changes in the outer atmospheres. In addition to the arguments discussed above, radio data indicate that the coronas of these stars contain particles accelerated to high energies. Evidence for this is provided by the centimeter-wavelength spectrum, which is radiated by subrelativistic electrons moving in the coronal magnetic fields. In other words, the spot bolometric flux deficits listed in Table 1 are consistent with the hypothesis that microflaring is the mechanism that transports energy from spots to the outer atmospheres in flare stars. It is not currently possible to identify any specific mechanism for this reconstruction of the outer atmospheres of active F–G stars. We have only some hints suggesting that it must be linked in some way to the ages of these objects, the lower fraction of their surfaces covered by active regions, compared to flare stars, and, possibly, some specific features of the development of their dynamo processes.

This general idea is just beginning to be worked on, and it would be useful to directly simulate the long-term photometric variations taking into account the relative areas of bright and dark photospheric elements and their contrasts, as has been done for variations in the solar constant. Such simulations must also take into account the different inclinations i of the stellar rotation axes with respect to the line of sight. This angle is close to 90° for many of the red dwarfs considered; i.e., these stars are, like the Sun, viewed almost along their equators. However, the amplitudes of variations on time scales of several days (the period of axial rotation) and

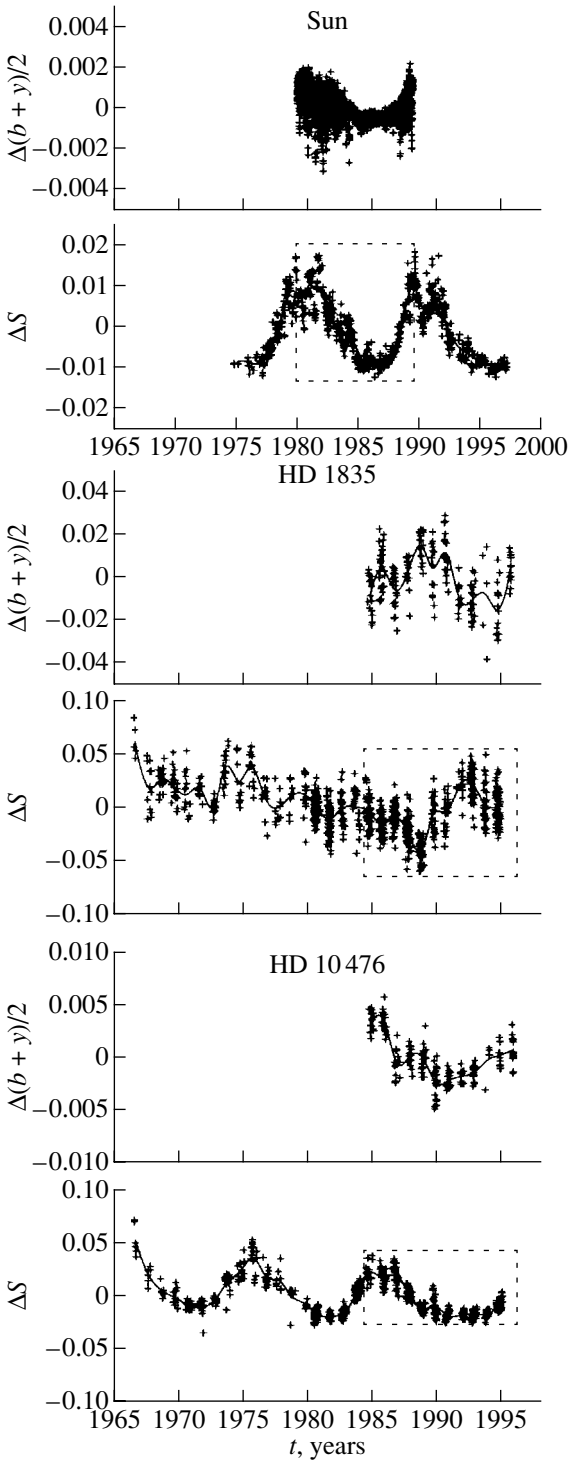

Fig. 5. Examples of different patterns of long-term variations of chromospheric (lower plots, ΔS) and photospheric (upper plots, $\Delta(b+y)/2$) radiation. Relative variations of chromospheric and photospheric radiation are expressed in S indices and magnitudes, respectively. (Adopted from [53].)

Table 2

No.	HD	Name	Sp	*B–V*	$\log R'_{HK}$	P_{rot}, days	Cycle, type, years
Group 1: Stars with correlated long-term variations of chromospheric and photospheric emission							
1	10476	107 Psc	K1V	0.84	–4.912	35	Exc. 9.6
2	18256	ρ^3 Ari	F5V	0.43	–4.722	3	Fair –
3	103095	Gmb 1830	G8VI	0.75	–4.896	31	Exc.
4	157856		F5V	0.46	–4.674	(4)	Fair –
5	160346		K3V	0.96	–4.795	37	Exc., 7
6	161239	84 Her	G6V	0.65	–5.164	(29)	Cycle
7	185144	σ Dra	K0V	0.80	–4.832	27	Exc., ≈7
8	201091	61 Cyg A	K5V	1.17	–4.764	35	Exc., 7.3
Group 2: Stars with anticorrelated long-term variations of chromospheric and photospheric emission							
1	1835	BE Cet	G2.5V	0.66	–4.433	8	Long
2	39587	χ^1 Ori	G0V	0.59	–4.426	5	Var
3	75332		F7V	0.49	–4.464	4	Var
4	82885	11 LMi	G8V–IV	0.77	–4.638	18	Fair/Poor
5	114710	β Com	F9.5V	0.57	–4.745	12	Good/Fair
6	115383	59 Vir	G0V	0.58	–4.443	3	Var
7	124570	14 Boo	F6IV	0.54	–5.156	26	Flat
8	129333	EK Dra	G0V	0.61	–4.157	3	Var
9	131156A	ξ Boo A	G8V	0.76	–4.363	6	Var
10	149661	V2133 Oph	K2 V	0.82	–4.583	21	Good (Cycle?)
11	152391	V2292 Oph	G7V	0.76	–4.448	11	Exc., 10.9
12	158614		G9IV–V	0.72	–5.028	(34)	Flat
13	176095		F5IV	0.46	–4.671	(4)	Long
14	203387		G8V	0.90	–4.42		
15	17925	EP Eri	K1V	0.87	–4.311	6.5	Long
16	82443	DX Leo	K0V	0.77	-4.211	5.40	Poor

several years (the period of activity cycles) decrease in the case of lower inclinations, especially if the star is viewed pole-on. This effect is manifest in five stars from Table 1 and is especially clear in the case of V 833 Tau and AD Leo, which have inclinations of $i = 20°$ and 38°, respectively. Note also that, in order for the effect of the inclination on ΔV and $\Delta\langle V\rangle$ to be brought in better agreement with observations, the optical emission should be computed with allowance for both spots and faculae.

5. CONCLUSIONS

We have used *BVRI* photometric observations and zonal spottedness models for 24 red dwarfs constructed at the Crimea Astrophysical Observatory covering a total of 342 epochs to compute for the first time the bolometric flux deficits of stellar spots. The absolute energy deficits are fairly high and range from 3×10^{29} to 5×10^{32} erg/s.

Our estimates indicate that, for the most active stars, the total radiative losses from their upper atmospheres and powerful sporadic flares are lower than these values; i.e., these losses cannot serve as outlets for the photospheric flux deficit. We therefore proposed that the missing energy of spotted photospheres goes into the formation of active upper atmospheres with dense, geometrically thin chromospheres and dense coronas containing high-temperature spots. Such outer atmospheres are similar to the structures that form during flares.

In the most active K–M stars, flare activity seems to be the most likely channel for the transport of energy associated with the photospheric flux deficit into upper atmospheric layers. This activity includes the nonradiative energy of individual sporadic flares, which, according to our computations, substantially exceeds their radiative energy, together with numerous microflares whose rate of occurrence must decrease with energy much more slowly than is true of strong detectable events.

The situation is quite different in the case of the Sun and other less active stars: here, the outlet of the photo-

spheric flux deficit can be the spreading of the energy in the vicinity of spots at nearly photospheric heights and the formation of facular fields and the associated chromospheric flocculi. Measurements of the solar constant have demonstrated that the Sun's photospheric flux deficit is compensated to a considerable extent by additional atmospheric radiation. These measurements showed that the solar constant decreased whenever a large group of spots crossed the solar disk; however, during the solar-activity maximum, when the number of spots was at its maximum, the solar constant actually increased due to the large number of active regions.

Our picture of the photospheric flux deficits of spotted F–M stars is based on these two extreme situations. The principal parameter of our picture is the stellar spot coverage, which varies both in the course of evolution of a particular star, due to secular deceleration of its rotation and decay of its magnetic activity, and as a result of systematic changes in the structure of the convection zone along the main sequence. Crudely speaking, on the Sun, with its mere fraction of a percent spot coverage, the photospheric flux deficit can be spread over large active regions surrounding the spots, whereas the most active stars with spot coverages reaching several tens of percent have no area left for large active regions, so that the energy associated with the photospheric flux deficit is channeled toward the upper atmosphere. The mechanism for the reconstruction of the outer atmospheres of active F–G stars may differ from the microflare mechanism typical of red dwarfs and possibly involves dynamical phenomena on a larger scale.

Our picture is supported by our combined analysis of the results of the HK project of O. Wilson and the long-term high-accuracy photometry of Radick *et al.* [53]. We have found further evidence suggesting that the total fluxes of the most active stars decrease during epochs of maximum chromospheric activity—that is, the variations are determined by large spotted regions with low temperatures, whereas less active stars become brighter during epochs of maximum chromospheric activity—in these objects, the additional facular radiation dominates over the flux deficit due to spots.

ACKNOWLEDGMENTS

We are grateful to Judith Lean for providing Fig. 4. This work was supported by the Russian Foundation for Basic Research (project no. 99-02-16289 and 01-02-17693), the Council for the Support of Leading Scientific Schools (project no. 00-15-96533), the Astronomy State Science and Technology Program (project no. 1.4.3.4), and NATO (grant no. PST.CLG.976557).

REFERENCES

1. H. C. Spruit, in *Surface Inhomogeneities on Late-Type Stars*, Ed. by P. B. Byrne and D. J. Mullan (Springer-Verlag, Heidelberg, 1992); Lect. Notes Phys. **397**, 78 (1992).
2. D. J. Mullan, Astrophys. J. **187**, 621 (1974).
3. E. Parker, Sol. Phys. **36**, 249 (1974).
4. L. W. Hartmann and R. Rosner, Astrophys. J. **230**, 802 (1979).
5. I. Yu. Alekseev and R. E. Gershberg, Astron. Zh. **73**, 579 (1996) [Astron. Rep. **40**, 528 (1996)]; Astron. Zh. **73**, 589 (1996) [Astron. Rep. **40**, 538 (1996)].
6. I. Yu. Alekseev and R. E. Gershberg, Astron. Zh. **74**, 240 (1997) [Astron. Rep. **41**, 207 (1997)].
7. H. L. Johnson, Ann. Rev. Astron. Astrophys. **4**, 193 (1966).
8. A. Young, A. Skumanich, J. R. Stauffer, *et al.*, Astrophys. J. **344**, 427 (1989).
9. J. R. Stauffer and L. W. Hartmann, Astrophys. J., Suppl. Ser. **61**, 531 (1986).
10. I. Yu. Alekseev and O. V. Kozlova, Astrofizika **43**, 339 (2000).
11. I. Yu. Alekseev and O. V. Kozlova, in preparation.
12. N. E. Piskunov, *Stellar Magnetism* [in Russian], Ed. by Yu. V. Glagolevskiĭ and I. I. Romanyuk (Nauka, St. Petersburg, 1992), p. 92.
13. N. E. Piskunov, F. Kupka, T. A. Ryabchikova, *et al.*, Astron. Astrophys., Suppl. Ser. **112**, 525 (1995).
14. N. E. Piskunov, F. Kupka, T. A. Ryabchikova, *et al.*, Astron. Astrophys., Suppl. Ser. **138**, 119 (1999).
15. S. R. Sundland, B. R. Pettersen, S. L. Hawley, *et al.*, in *Activity in Cool Star Envelopes*, Ed. by O. Havnes, B. R. Pettersen, J. H. M. M. Schmitt, and J. E. Solheim (Kluwer, Dordrecht, 1988), p. 61.
16. N. I. Shakhovskaya, Izv. Krym. Astrofiz. Obs. **51**, 92 (1974).
17. B. R. Pettersen, Vistas Astron. **3**, 41 (1987).
18. R. C. Dempsey, J. L. Linsky, T. A. Fleming, and J. H. M. M. Schmitt, Astrophys. J., Suppl. Ser. **86**, 599 (1993).
19. A. Marino, G. Micela, and G. Peres, Astron. Astrophys. **353**, 177 (2000).
20. D. A. Quin, J. G. Doyle, C. J. Butler, *et al.*, Astron. Astrophys. **272**, 477 (1993).
21. N. I. Shakhovskaya, Sol. Phys. **121**, 375 (1989).
22. J. L. Linsky, P. L. Bornmann, K. G. Carpenter, *et al.*, Astrophys. J. **260**, 670 (1982).
23. B. J. Oranje, Astron. Astrophys. **154**, 185 (1986).
24. C. J. Schrijver, A. K. Dobson, and R. R. Radick, Astron. Astrophys. **258**, 432 (1992).
25. M. Shimojo, S. Hashimoto, K. Shibata, *et al.*, Publ. Astron. Soc. Jpn. **48**, 123 (1996).
26. S. Kouchmy, H. Hara, Y. Suematsu, and K. Reardon, Astron. Astrophys. **320**, L33 (1997).
27. M. A. Livshits, B. A. Ioshpa, V. N. Obridko, *et al.*, in *Proceedings of the 7th Symposium on Solar-Terrestrial Physics* [in Russian] (Troitsk, 1999), p. 11.
28. J. Qiu, M.-D. Ding, H. Wang, *et al.*, Astrophys. J. (2000) (in press).
29. V. V. Kasinsky and R. T. Sotnikova, Astron. Astrophys. Trans. **12**, 313 (1997).
30. Yu. E. Litvinenko, Sol. Phys. **151**, 195 (1994).
31. E. R. Houdebine, Ir. Astron. J. **20**, 213 (1992).

32. É. A. Baranovskiĭ, R. E. Gershberg, and D. N. Shakhovskoĭ, Astron. Zh. **78**, 78 (2001) [Astron. Rep. **45**, 67 (2001)].
33. E. R. Houdebine, J. G. Doyle, and M. Koscielecky, Astron. Astrophys. **294**, 773 (1995).
34. J. J. Drake, *Cool Stars, Stellar Systems, and the Sun*, Ed. by R. Pallavicini and A. K. Dupree; Astron. Soc. Pac. Conf. Ser. **109**, 203 (1996).
35. M. Güdel, Astrophys. J., Suppl. Ser. **90**, 743 (1994).
36. M. A. Livshits, O. G. Badalyan, A. G. Kosovichev, and M. M. Katsova, Sol. Phys. **73**, 269 (1981).
37. M. M. Katsova, A. Ya. Boiko, and M. A. Livshits, Astron. Astrophys. **321**, 549 (1997).
38. É. A. Baranovskiĭ, R. E. Gershberg, and D. N. Shakhovskoĭ, Astron. Zh. **78**, 359 (2001) [Astron. Rep. **45** (4), 309 (2001)].
39. M. M. Katsova and M. A. Livshits, Astron. Zh. **68**, 131 (1991) [Sov. Astron. **35**, 65 (1991)].
40. A. Ya. Boĭko and M. A. Livshits, Astron. Zh. **76**, 860 (1999) [Astron. Rep. **43**, 759 (1999)].
41. M. M. Katsova, S. L. Hawley, W. P. Abbet, and M. A. Livshits, Preprint No. 4 (1120) (IZMIRAN, 1999), p. 1.
42. M. M. Katsova, M. A. Livshits, C. J. Butler, and J. G. Doyle, Mon. Not. R. Astron. Soc. **250**, 402 (1991).
43. I. Yu. Alekseev and R. E. Gershberg, *The Earth and the Universe*, Ed. by G. Asteriadis *et al.* (Ziti Editions, Thessaloniki, 1997), p. 43.
44. J. H. M. M. Schmitt, R. M. Haisch, and H. Barwig, Astrophys. J. Lett. **419**, L81 (1993).
45. R. F. Stein, Astrophys. J. **246**, 966 (1981).
46. P. Ulmschneider and H. U. Bohn, Astron. Astrophys. **254**, 173 (1981).
47. R. E. Gershberg, É. I. Mogilevskiĭ, and V. N. Obridko, Kinematika Fiz. Nebesnykh Tel **5**, 3 (1987).
48. C. J. Butler and M. Rodono, Ir. Astron. J. **17**, 131 (1985).
49. A. Collura, L. Pasquini, and J. H. M. M. Schmitt, Astron. Astrophys. **205**, 197 (1988).
50. R. Pallavicini, J. Tajliaferri, and L. Stella, Astron. Astrophys. **228**, 403 (1990).
51. M. Audard, M. Güdel, and E. F. Guinan, Astrophys. J. Lett. **513**, L53 (1999).
52. M. Audard, M. Güdel, J. J. Drake, and V. L. Kashyap, Astrophys. J. **541**, 396 (2000).
53. R. R. Radick, G. W. Lockwood, B. A. Skiff, and S. L. Baliunas, Astrophys. J., Suppl. Ser. **118**, 239 (1998).
54. I. Yu. Alekseev, *Low-Mass Spotted Stars* [in Russian] (Odessa, Astroprint, 2001).
55. A. H. Vaughan and R. W. Preston, Publ. Astron. Soc. Pac. **92**, 385 (1980).
56. S. H. Saar and S. L. Baliunas, in *The Solar Cycle*, Ed. by K. L. Harvey; Astron. Soc. Pac. Conf. Ser. **27**, 150 (1992); **27**, 197 (1992).
57. S. L. Baliunas, E. Nesme-Ribes, D. Sokoloff, and W. H. Soon, Astrophys. J. **460**, 848 (1996).
58. M. Güdel, E. F. Guinan, and S. L. Skinner, Astrophys. J. **483**, 947 (1997).
59. J. Lean, in *Surface Inhomogeneities on Late Type Stars*, Ed. by P. B. Byrne and D. J. Mullan (Springer-Verlag, Heidelberg, 1992); Lect. Notes Phys. **397**, 167 (1992).
60. J. Lean, in *Cool Stars, Stellar Systems, and the Sun*, Ed. by R. J. G. López, R. Rebolo, and M. R. Zapatero-Osorio; ASP Cons. Ser. **223**, 109 (2000).
61. S. L. Baliunas, R. A. Donahue, and W. H. Soon, Astrophys. J. **438**, 269 (1995).
62. Y. C. Unruh, S. K. Solanki, and M. Fligge, Astron. Astrophys. **345**, 635 (1999).
63. K. H. Schatten, J. Geophys. Res. **98** (A11), 18907 (1993).
64. Y. C. Unruh, R. Knaack, M. Fligge, and S. K. Solanki, in *Cool Stars, Stellar Systems, and the Sun*, Ed. by R. J. G. López, R. Rebolo, and M. R. Zapatero-Osorio; ASP Cons. Ser. **223**, CD-748 (2001).

Translated by A. Dambis